


2004

# Multifunctional mesoporous silica nanospheres for biosensor, stimuli-responsive controlled-release drug delivery carriers and gene transfection vectors

Cheng-Yu Lai  
Iowa State University

Follow this and additional works at: <https://lib.dr.iastate.edu/rtd>

 Part of the [Biochemistry Commons](#), and the [Inorganic Chemistry Commons](#)

## Recommended Citation

Lai, Cheng-Yu, "Multifunctional mesoporous silica nanospheres for biosensor, stimuli-responsive controlled-release drug delivery carriers and gene transfection vectors " (2004). *Retrospective Theses and Dissertations*. 1700.  
<https://lib.dr.iastate.edu/rtd/1700>

This Dissertation is brought to you for free and open access by the Iowa State University Capstones, Theses and Dissertations at Iowa State University Digital Repository. It has been accepted for inclusion in Retrospective Theses and Dissertations by an authorized administrator of Iowa State University Digital Repository. For more information, please contact [digirep@iastate.edu](mailto:digirep@iastate.edu).

Multifunctional mesoporous silica nanospheres for biosensor, stimuli-responsive controlled-release drug delivery carriers and gene transfection vectors

by

Cheng-Yu Lai

A dissertation submitted to the graduate faculty  
in partial fulfillment of the requirements for the degree of  
DOCTOR OF PHILOSOPHY

Major: Inorganic Chemistry  
Program of Study Committee  
Victor S. Y. Lin, Major Professor  
Robert J. Angelici  
Edward S. Yeung  
Keith L. Woo  
Nicola L. Pohl

Iowa State University

Ames, Iowa

2004

Copyright © Cheng-Yu Lai, 2004. All rights reserved.

UMI Number: 3190720

### INFORMATION TO USERS

The quality of this reproduction is dependent upon the quality of the copy submitted. Broken or indistinct print, colored or poor quality illustrations and photographs, print bleed-through, substandard margins, and improper alignment can adversely affect reproduction.

In the unlikely event that the author did not send a complete manuscript and there are missing pages, these will be noted. Also, if unauthorized copyright material had to be removed, a note will indicate the deletion.

**UMI**<sup>®</sup>

---

UMI Microform 3190720

Copyright 2006 by ProQuest Information and Learning Company.

All rights reserved. This microform edition is protected against unauthorized copying under Title 17, United States Code.

ProQuest Information and Learning Company  
300 North Zeeb Road  
P.O. Box 1346  
Ann Arbor, MI 48106-1346

Graduate College  
Iowa State University

This is to certify that the doctoral dissertation of  
Cheng-Yu Lai  
has met the dissertation requirements of Iowa State University

Signature was redacted for privacy.

Major Professor

Signature was redacted for privacy.

For the Major Program

Dedication

“With a keen eye for details, all the appearances can be broken and one truth will prevail.”

~ To Conan and Jimmy ~

## Table of Contents

List of Figures	viii
List of Tables	xiv
Acknowledgements	xv
Abstract	xvi
Chapter 1. Dissertation organization	1
Chapter 2. Fine-tuning the Degree of Organic Functionalization of Mesoporous Silica Nanosphere Materials via an Interfacially Designed Cocondensation Method	
Abstract	3
Introduction	3
Materials and Methods	4
Results and Discussion	8
Conclusions	15
Acknowledgements	15
References	16
Chapter 3. Molecular Recognition Inside of Multifunctionalized Mesoporous Silicas: Toward Selective Fluorescence Detection of Dopamine and Glucosamine	
Abstract	18
Introduction	18
Materials and Methods	19
Results and Discussion	26

Conclusions	31
Acknowledgements	31
References	31
Chapter 4. Gatekeeping Layer Effect: A Poly(lactic acid)-coated Mesoporous Silica Nanosphere-Based Fluorescence Probe for Detection of Amino-Containing Neurotransmitters	
Abstract	34
Introduction	34
Materials and Methods	35
Results and Discussion	39
Conclusions	48
Acknowledgements	48
References	48
Chapter 5. A Mesoporous Silica Nanosphere-Based Carrier System with Chemically Removable CdS Nanoparticle Caps for Stimuli-Responsive Controlled Release of Neurotransmitters and Drug Molecules	
Abstract	51
Introduction	52
Materials and Methods	54
Results and Discussion	59
Conclusions	71
Acknowledgements	71
References	71
Appendices A and B	74
Chapter 6. Real-Time ATP Imaging of Tunable Release from a MCM-41-type Mesoporous Silica Nanosphere-Based Delivery System	

Abstract	76
Introduction	76
Materials and Methods	78
Results and Discussion	80
Conclusions	91
Acknowledgements	91
References	91

#### Chapter 7. A Polyamidoamine Dendrimer-capped Mesoporous Silica Nanosphere-based Gene Transfection Reagent

Abstract	95
Introduction	96
Materials and Methods	96
Results and Discussion	103
Conclusions	115
Acknowledgements	115
References	115

#### Chapter 8. An Intracellular Mesoporous Silica Nanosphere-based Controlled Release Delivery Carrier for Anticancer drugs and Multi-plasmids Transfection

Abstract	116
Introduction	116
Materials and Methods	117
Results and Discussion	124
Conclusions	138
Acknowledgements	138
References	138





## List of Figures

## Chapter 2

- Figure 2-1. Schematic representation of the synthesis of organoalkoxysilane precursors. 5
- Figure 2-2. Schematic representation of the utilization of anionic organoalkoxysilane for controlling the functionalization of the MSN materials. 9
- Figure 2-3. SEM images of MSN-SH (a), MSN-COOH (b) and MSN-SO<sub>3</sub>H (c). 10
- Figure 2-4. Powder XRD diffraction patterns of the MSN-SH (green), MSN-COOH (red) and MSN-SO<sub>3</sub>H (blue) materials after treatment with disulfide reducing agent (DTT). 11
- Figure 2-5. (a) Nitrogen sorption isotherms of the MSN-SH (green), MSN-COOH (red) and MSN-SO<sub>3</sub>H (blue) materials after treatment with disulfide reducing agent (DTT). (b) Pore size distributions of the MSN-SH, MSN-COOH and MSN-SO<sub>3</sub>H materials. 12
- Figure 2-6. Solid state <sup>13</sup>C CP-MAS NMR spectra of the MSN-SH (up), MSN-COOH (middle) and MSN-SO<sub>3</sub>H (bottom). 12
- Figure 2-7. Schematic representation of the formation of thiol-functionalized mesoporous silica material (MSN-SO<sub>3</sub>H) via disulfide reduction with dithiothreitol (DTT). 13

## Chapter 3

- Figure 3-1. Schematic representation of the *o*-phthalic hemithioacetl (OPTA) functionalized mesoporous silica material and their fluorescent detection of amines. 19
- Figure 3-2. Schematic representation of the formation of thiol-functionalized mesoporous silica material (M1) via disulfide reduction with dithiothreitol. 22
- Figure 3-3. (a) Incorporation of the covalently linked organic groups was confirmed by <sup>29</sup>Si CP NMR spectroscopy. (b) <sup>13</sup>C CP-MAS NMR spectra of these materials further verified the multi-functional nature of the M2, M3, and OPTA-M1 indicating that all the organic functional groups were

covalently linked to the silica surfaces.	23
Figure 3-4. TEM image of a representative region of thiol-functionalized mesoporous silica (M1) after surfactant extraction and disulfide reduction.	24
Figure 3-5. BET Nitrogen Adsorption Isotherms and BJH Pore-size distributions of multifunctionalized mesoporous materials, from M1 to M4.	25
Figure 3-6. Kinetic measurements of the fluorescence detection of dopamine (a) and glucosamine (b) with OPTA-derivatized amorphous silicas grafted with secondary functional groups.	28
Figure 3-7. Kinetic measurements of the fluorescence detection of dopamine (a) and glucosamine (b) with OPTA-derivatized mesoporous silicas grafted with secondary functional groups	30

#### Chapter 4

Figure 4-1. Schematic representation of a surface of MSN materials: Thiol-MSN (a) and DH-MSN (b).	35
Figure 4-2. Schematic representation of the synthesis of PLA-coated MSN based fluorescence sensor system for detection of amine-containing neurotransmitters.	40
Figure 4-3. $^1\text{H} \rightarrow ^{13}\text{C}$ CPMAS (a-c), $^{29}\text{Si}$ DPMAS (d-f) and $^1\text{H} \rightarrow ^{29}\text{Si}$ CPMAS (g-i) spectra collected for Thiol-MSN (a,d,g), DH-MSN (b,e,h) and PLA-MSN (c,f,i) samples.	42
Figure 4-4. Transmission electron micrograph (TEM) of an ultramicrotomed PLA-MSN material.	43
Figure 4-5. Powder X-Ray diffraction patterns of thiol-MSN, DH-MSN, and PLA-MSN.	44
Figure 4-6. BET nitrogen adsorption/desorption isotherms and BJH pore size distributions of DH-MSN (solid line) and PLA-MSN (dashed line) materials.	45
Figure 4-7. Particle size distribution (a) and scanning electron micrograph (b) of PLA-MSN.	45
Figure 4-8. Kinetic measurements of the fluorescence detection of dopamine (s), tyrosine and glutamic acid with OPTA-SS (a) and PLA-MSN (b).	46

- Figure 4-9. HPLC chromatographs of the solution containing dopamine (0.5 mM) and glutamic acid (10 mM) before (blue) and after (red) the introduction of PLA-MSN. 47

## Chapter 5

- Figure 5-1. Schematic representation of the CdS nanoparticle-capped MSN-based drug/neurotransmitter delivery system. 53
- Figure 5-2. Synthesis of 2-(propylsulfanyl)ethylamine functionalized mesoporous silica nanosphere (linker-MSN) material. 60
- Figure 5-3. (a) BET nitrogen adsorption/desorption isotherms of the thiol-MSN material before and after covalent encapsulation of the mercaptoacetic acid-functionalized CdS nanoparticles. (b) BJH pore size distributions for the thiol-MSN and CdS-capped MSN nanocomposite materials. 61
- Figure 5-4. SEM (a and b) and TEM (300 kV) micrographs of the linker-MSN (c and e). The TEM micrographs (d and f) of the CdS-capped MSN clearly exhibit aggregations of CdS nanoparticles on the exterior surface of MSN material represented by dots in the areas indicated by black arrows in (d). 62
- Figure 5-5. Low (a) and high (b) angle powder X-ray diffraction patterns (XRD) of the linker-MSN material before (solid line) and after (dashed line) the immobilization of CdS nanocrystals. 64
- Figure 5-6. The DTT-induced release profiles of Vancomycin and ATP from the CdS-capped MSN system: (a) % release over time. (b) The DTT concentration-dependent releases. Released analyte concentrations were measured with CdS-MSNs (2.3 mg) in pH 7.4 PBS buffers (0.8 mL) after 24 h of the DTT additions. 65
- Figure 5-7. Effect of ATP release from CdS-capped MSNs on astrocytes. (a) Top panels show the pseudocolor images of astrocytes loaded with Fura-2 at resting level (top left panel) and after the application of ME (top right panel). (b) Left bottom panel shows the fluorescence of cells and CdS at 520 nm

( $\lambda_{\text{ex}} = 380 \text{ nm}$ ). (c) Right bottom graph is a time course of astrocytes and CdS-capped MSN fluorescence prior to and after the application of ME. 68

Figure 5-8. (a) Images showing that application of ME on an astrocyte culture loaded with the intracellular  $\text{Ca}^{2+}$ -chelating fluorophore without the presence of MSN failed to produce any  $[\text{Ca}^{2+}]_i$  response of astrocytes.  
 (b) Pseudo-color image of astrocytes taken after the ME application showed no increase or decrease in  $[\text{Ca}^{2+}]_i$  of the cells.  
 (c) The same cells responded to the perfusion application of  $100.0 \text{ }\mu\text{M}$  ATP indicated by the increase of fluorescence intensity of the pseudo-color image of astrocytes. 69

Figure 5-9. Pseudo-color images of an astrocyte culture in the presence of random piles of CdS-capped MSNs with empty mesoporous channels before (a) and after (b) the application of ATP ( $100.0 \text{ }\mu\text{M}$ ). An increase in  $[\text{Ca}^{2+}]_i$  of the astrocytes (lower square, red) located adjacent to a pile of MSNs (upper square, yellow) upon the perfusion application of ATP was observed (d, lower curve). 70

## Chapter 6

Figure 6-1. SEM (A) and TEM (B, C) micrographs of PAMAM dendrimer-capped MSN. 82

Figure 6-2. Solid state  $^{13}\text{C}$  CPMAS (A),  $^{31}\text{P}$  CPMAS (B),  $^{29}\text{Si}$  DPMAS (C), and  $^{29}\text{Si}$  CPMAS (D) spectra of ATP-loaded MSN material capped with G2.5 PAMAM dendrimers. 83

Figure 6-3. Effect of disulfide-cleaving molecules on chemiluminescence signal. 85

Figure 6-4. Release of encapsulated ATP from MCM-type mesoporous nanospheres. 86

Figure 6-5. Effect of uncapping agent concentration on the magnitude of release of encapsulated ATP from MCM-type mesoporous nanospheres. 89

Figure 6-6. Release of encapsulated ATP from dendrimer-capped MCM-41-type mesoporous nanospheres. 90

## Chapter 7

Figure 7-1. Schematic representation of a non-viral gene transfection.	96
Figure 7-2. Schematic representation of a non-viral gene transfection system based on a Texas Red. (TR)-loaded, G2-PAMAM dendrimercapped MSN material complexed with an enhanced green fluorescence protein ( <i>Aequorea victoria</i> ) plasmid DNA (pEGFP-C1).	103
Figure 7-3. Powder X-Ray diffraction patterns of purified ICP-MSN, G2-MSN, and Texas Red-loaded G2-MSN materials.	104
Figure 7-4. BET nitrogen adsorption/desorption isotherms (a) and BJH pore size distributions (b) of MSN, ICP-MSN, G2-MSN, and Texas Red-loaded G2-MSN materials.	105
Figure 7-5. <sup>13</sup> C solid state CP-MAS NMR spectra of the ICP-MSN (top) and G2-MSN (bottom) materials.	106
Figure 7-6. SEM (a) and TEM (300 kV) micrographs of the G2-MSN (b).	107
Figure 7-7. Complexation of G2-MSN with pEGFP-C1 DNA (GFP)	108
Figure 7-8. Electrophoretic gel shifts of stability Studies of pEGFP-C1 DNA and G2-MSN-DNA Complex after Bam H1 treatment.	109
Figure 7-9. Fluorescent microscopy images of HeLa cells treated with G2-MSN-DNA complexes that have first been exposed to <i>BamH</i> I.	109
Figure 7-10. Flow cytometry analysis of the transfection of pEGFP in HeLa cells with G2-MSN.	111
Figure 7-11. Fluorescence confocal micrographs of cells transfected by pEGFP-C1-coated G2-MSN system.	112
Figure 7-12. TEM micrographs of G2-MSN-DNA complexes (black dots) endocytosed by Chinese hamster ovarian (CHO) (a), human cervical cancer (HeLa) (b), and neural glia (astrocytes) (c) cells.	113
Figure 7-13. Cell growth of (a) HeLa and (b) CHO cells in the presence of G2-MSN (gray bars) and in the absence of G2-MSN (black bars).	114

## Chapter 8

Figure 8-1. Schematic representation of Texas Red incorporated mesoporous silica nanospheres, T-MSN.	124
Figure 8-2. Scanning electron micrographs (SEM) of the mesoporous silica nanospheres (MSN). Scale bars = 100 nm (a) and 1.0 $\mu$ m (b).	125
Figure 8-3. High-resolution transmission electron micrographs (TEM) of FTIC incorporated MCM-41 mesoporous silica nanospheres with amine functionality (F-MSN).	125
Figure 8-4. Schematic representation of possible interaction of MSNs with HeLa cells.	127
Figure 8-5. F-MSN internalization. Dosage study (a); Time dependence study (b).	128
Figure 8-6. Fluorescent MSNs after endocytosis and cell mitosis – a dividing HeLa cell.	128
Figure 8-7. Cellular application of F-MSN (a) F-MSN engaged in endocytosis. (b) F-MSNs inside of a HeLa cell.	129
Figure 8-8. Doxorubicin delivery: Free doxorubicin delivered to HeLa Cells (a); MSN Encapsulated doxorubicin delivery in HeLa Cells (b).	130
Figure 8-9. Cleavable versus non-cleavable caps.	131
Figure 8-10. HPLC study of Doxorubicin release kinetics from Dox-MSNs.	132
Figure 8-11. Kinetic study of Doxorubicin release: the Dox-MSNs were applied to cell cultures and monitored every four hours: after 4h (a); after 8h (b); after 12h (c).	133
Figure 8-12. Transfection of neural glia (astrocytes) with pEGFP utilizing G2-MSN as a transfection vector.	135
Figure. 8-13 TEM micrograph of cotransfected HeLa cells.	136
Figure. 8-14. Confocal fluorescence images and phase contrast images of HeLa cells (a) and CHO cells (b).	137
Figure. 8-15. Relative transfection efficiencies between several transfection reagents: G2-MSN, Polyfect and Superfect Mock transfection were also performed to demonstrate that there is no fluorescent signal detected in the absence of DNA complexed MSNs.	137

## List of Tables

Table 2-1. Structural properties of the organically functionalized MSN materials (MSN-SH, MSN-COOH and MSN-SO <sub>3</sub> H ).	14
Table 2-2. Elemental Analysis of the organically functionalized MSNs (MSN-SH, MSN-COOH and MSN-SO <sub>3</sub> H ).	15
Table 3-1. Characterization of Multifunctionalized Mesoporous Silicas (M1 to M4).	27
Table 4-1. Summary of <sup>13</sup> C CPMAS NMR data of PLA/MSN particles.	41
Table 4-2. Summary of <sup>29</sup> Si CPMAS NMR DATA PLA/MSN particles.	42
Table 4-3. Powder X-Ray diffraction results of MSNs (Thiol-MSN, DH-MSN and PLA-MAN).	44
Table 4-4. Nitrogen sorption isotherms of PLA/MSN particles.	44
Table 4-5. HPLC analysis of dopamine and glutamic acid before and after the introduction of PLA-MSN.	47
Table 5-1. Structural parameters of the thiol-MSN and the CdS-capped MSN materials.	64
Table 6-1. Characteristics of release of encapsulated ATP from CdS-capped MCM-type mesoporous nanospheres for various reducing agents.	88
Table 7-1. Powder X-Ray diffraction patterns of MSNs (CP-MSN, G2-MSN and Tex/G2-MSN).	105
Table 7-2. BET and BJH parameters of MSNs (MSN, ICP-MSN, G2-MSN and Tex/G2-MSN).	105
Table 7-3. Transfection Efficiencies of different transfection reagents on HeLa cells.	110



## Acknowledgments

This work would not have been possible without the help and talent from many people.

First and foremost, I would like to express my sincere appreciation to my advisor, Dr. Victor Shang-Yi Lin, for his generous support throughout several challenging research fields.

My particular thanks also go to all the committee members, Dr. Robert Angelici, Dr. Edward Yeung, Dr. Keith Woo, Dr. Nicola Pohl, for their valuable comments and suggestions on my research.

Sincere gratitude is also expressed to Dr. Paul Kapke, Dr. Janice Buss, Dr. Luisa Tobatabai, Dr. Marit Nilsen-Hamilton for their time and valuable suggestions and comments on my thesis work.

Especially, I wish to thank to Dr. Nenad Kostic and his former graduate students for their friendship and help. Without their enthusiastic participation and great effort, my research would have been done.

Many thanks expressed to people in Chemistry Store, Cell facility, Hybridoma Facility, DNA Facility, Protein Facility, Image Facility, Bessey Microscopy Facility and Scanning Microscopy in Town Engineering, friends from Taiwan and China in this campus for their generous help and patience.

I am grateful to all the funding agencies for their support of the projects in this dissertation.

I thank both Kate Hung and Shu Wu who have made my academic experience rich and memorable.

I thank my family for their support, especially when I was bumped down in past years.

## Abstract

Structurally well-defined mesoporous silica materials with tunable pore size and narrow pore-size distribution have attracted much attention for their potential applications in sensing, drug delivery and gene transfer. A series of mesoporous silica nanosphere-based (MSN) nano-devices presented herein were synthesized and utilized for the aforementioned applications.

In terms of sensing applications, we provide a first example in utilization of a multi-functionalized mesoporous silica material to selectively detect dopamine. The system selectivity is regulated by the organic functional groups that are located on the pore surface allowing only the target molecules to penetrate into the mesopores to access the sensing functionality. A second application, rooted in this work, is the selective detection of amino-containing neurotransmitters under physiological condition. To serve this purpose we developed a fluorescence probe consisting of a poly(lactic acid)-coated, MCM-41 type mesoporous silica nanosphere (PLA-MSN) material. By utilizing the PLA layer as a gatekeeper to regulate the penetration of molecules in and out of the nano-scale pores, the PLA-MSN can selectively recognize dopamine from several structurally similar neurotransmitters (tyrosine and glutamic acid).

Drug delivery applications have been built around a controlled release delivery device. In the original conception, the system used surface-derivatized cadmium sulfide (CdS) nanocrystals or poly(amido amine) dendrimers (PAMAM) as chemically removable caps to encapsulate several drug molecules and neurotransmitters inside the organically functionalized MSN mesoporous framework. The caps are covalently attached to the channels openings, with a chemically cleavable disulfide bond. The stimuli-responsive release profiles of drug-loaded MSN delivery systems were studied by using disulfide reducing molecules, such as dithiothreitol (DTT) and mercaptoethanol (ME), as release triggers. A luciferase chemiluminescence imaging method was employed to investigate the kinetics and mechanism of the ATP release with various disulfide-reducing agents as uncapping triggers in real time. By varying the chemical nature of the “cap” and “trigger” molecules in our MSN system, we discovered that the release profiles could be regulated in a controllable fashion.

Further, bio-compatible PAMAM dendrimers of low generations, size matched to the entrance of the channel of these branched, globular-shaped molecules were utilized in cancer drug delivery. The biocompatibility and delivery efficiency of the later MSN system in interaction with HeLa cervical cancer cells were demonstrated. The system renders the possibility to serve as a universal transmembrane carrier for intracellular drug delivery and imaging applications. This is the first uptake study of MCM-41 type mesoporous silicas into eukaryotic cells.

The last application presented in this dissertation is gene delivery. We designed a MSN-based gene transfection system, where second generation (G2) PAMAMs were covalently attached to the surface of MSNs. The G2-PAMAM-capped MSN material (G2-MSN) was able to complex with a plasmid DNA (pEGFP-C1) that is encoding for an enhanced green fluorescence protein. The gene transfection efficacy, uptake mechanism, and biocompatibility of the G2-MSN system with various cell types, such as neural glia (astrocytes), human cervical cancer (HeLa), and Chinese hamster ovarian (CHO) cells were investigated. In contrast to other non-viral state-of-the-art gene transfer systems, the mesoporous structure of the MSN allows gene regulators small molecule to be encapsulated inside the MSN channels. The uniqueness of this gene carrier resides in the utilization of low generation PAMAM dendrimers in gene transfection as well as in the ability of the system to perform cotransfection of two separate types of genes. This later feature would enable the system to be employed in therapeutic gene delivery studies.

## Chapter 1. Introduction of Mesoporous Silicates MCM-41

### Dissertation Organization

This dissertation is divided into nine chapters based on chronological order. From chapter 2 to 8, each consists of a journal paper presented with its own abstract, introduction, results and discussion, experimental section, conclusions, acknowledgements and references. Chapter one presents the thesis organization and chapter nine is a final review of the entire dissertation.

Chapter 2 describes a synthetic method that can fine tune the amount of chemically accessible organic functional groups on the pores surface of MCM-41 type mesoporous silica nanosphere (MSN) materials by matching the cationic alkylammonium head group of the surfactant with various anionic organoalkoxysilane precursors at the micelle-water interface. My personal contribution represents 40% of the presented research.

Chapter 3 describes the design and synthesis of a well-defined, monodispersed mesoporous silica nanosphere (MSN) as a fluorescence sensory system which could serve as synthetic scaffolds to study the molecular recognition events of biogenic molecules, such as dopamine and glucosamine. The characterization, surface modification and molecular recognition experiments of MSN are presented. My personal contribution represents 90% of the presented research.

Chapter 4 extends the sensing application of MSN to a poly(lactic acid) coated MCM-41-type mesoporous silica nanosphere (PLA-MSN) that can serve as a fluorescence sensor system for detection of amino-containing neurotransmitters in neutral aqueous buffer while simultaneously provide a biocompatible layer for neuronal interaction. My personal contribution represents 40% of the presented research.

Chapter 5 describes the synthesis and characterization of a site-selective MCM-41 type mesoporous silica nanosphere-based (MSN) controlled-release delivery system using surface-derivatized cadmium sulfide (CdS) nanocrystals as chemically removable caps to encapsulate several molecules inside the organically functionalized MSN mesoporous framework. In this chapter, the release profiles of several drugs and delivery efficiencies of

neuroglia cells are also discussed. My personal contribution represents 90% of the presented research.

Chaper 6 extends the application of a MSN type controlled release nano-device by replacing caps form CdS nanocrystals to more biofriendly polyamidoamine organic dendimer (PAMAM). My personal contribution represents 40% of the presented research.

Chapter 7 describes a novel polyamidoamine dendrimer-capped mesoporous silica nanosphere-based gene transfection reagent. This new gene shuttle, A nano-Trojan Horse, provides high transfection efficiencies in several types of cells. The chapter also introduces the biocompatibility study of capped-MSNS as well as their cellular uptake behavior. My personal contribution represents 50% of the presented research.

Chapter 8 is presenting an intracellular delivery nano-vehicle based on PAMAM-dendrimer capped MSNs. The main focus of the chapter is on drug-delivery, achieved on HeLa cancer cells by utilizing Doxorubicin-encapsulated MSNs. Furthermore, for demonstrating the versatility of coating methodology, this cargo was utilized for condensing two different types of DNA on the external surface for co-transfection of different types of cells. My personal contribution represents 51% of the presented research.

The final chapter summarizes the entire dissertation, bringing a final overview of each chapter.

Chapter 2. Fine-tuning the Degree of Organic Functionalization of Mesoporous Silica  
Nanosphere Materials via an Interfacially Designed Cocondensation Method

The paper is in press in *Chemical Communications*

Radu, D. R.; **Lai, C.-Y.**; Huang, J.; Xu S.; Lin, V.S.-Y.

Department of Chemistry, Iowa State University, Ames, Iowa 50011-3111

Abstract

A synthetic method that can fine tune the amount of chemically accessible organic functional groups on the pore surface of MCM-41 type mesoporous silica nanosphere (MSN) materials has been developed by electrostatically matching various anionic organoalkoxysilanes with the cationic cetyltrimethylammonium bromide micelles in a base-catalyzed condensation reaction of tetraethoxysilane.

Introduction

Recent advancements in utilizing organic surfactants or block copolymers as structure-directing templates for the syntheses of structurally well-defined mesoporous silica materials, such as MCM-41/48,<sup>1</sup> SBA-15,<sup>2</sup> MSU-n,<sup>3</sup> and FSM-16,<sup>4</sup> have attracted much attention for their potential applications in sensing,<sup>5</sup> catalysis,<sup>6</sup> and drug delivery.<sup>7</sup> Obviously, the realization of these applications greatly depends on the ability to functionalize the interior and exterior surfaces of the mesoporous silicas with various organic functional groups. Although a wide variety of synthetic approaches have been pursued and some significant progresses has been made, few would argue that the current state-of-the-art methods, such as post synthesis grafting<sup>8</sup> and organosiloxane/siloxane co-condensation<sup>9</sup> methods, need to be improved in terms of controlling the amount and location of the incorporated functional groups on the surface of the mesoporous silica materials. For example, functional groups incorporated via the post synthesis grafting method typically

congregate at the opening parts of porous channels resulting in an inhomogeneous surface coverage,<sup>10</sup> whereas the amount of functional groups introduced by the organosiloxane/siloxane co-condensation method is yet to reach above 25% surface coverage without destroying the structural integrity and the long-range periodicity of the synthesized materials.<sup>9,10</sup> Herein, we report on a new co-condensation method that could generate organically functionalized, MCM-41 type of mesoporous silica nanosphere materials while controlling the surface concentration of organic functional groups.

## Materials and Methods

### Experimental Section

Materials. 3-Mercaptopropionic acid (99+%), 2,2'-dipyridyl disulfide (98%), (3-mercaptopropyl)trimethoxysilane (MPTES) (95%), 2-mercaptoethanesulfonic acid sodium salt (98%), cetyltrimethylammonium bromide (CTAB), tetraethyl orthosilicate (TEOS, 96%) and dithiothreitol (DTT) were purchased from Aldrich Chemical Co. (Milwaukee, WI). Acetic acid (Glacial), hydrochloric acid (37.4%), sodium hydroxide, ethanol (anhydrous), methanol (HPLC grade), tetrahydrofuran (HPLC grade), hexanes (pesticide grade) and ethyl ether (anhydrous) were obtained from Fisher Scientific Co. (Pittsburgh, PA). Nanopure water was deionized to 18.0 M $\Omega$ -cm in a Barnstead E-pure water purification system and used for the synthesis of MSN materials.

### Synthesis of organoalkoxysilane precursors

#### 2-[3-(trimethoxysilyl)-propyl]disulfanyl]-propionic acid, CDSP-TMS, (1b)

As depicted in Figure 2-1, 2-Carboxyethyl-2-pyridyl-disulfide, compound (1a), was prepared according to a procedure published by Carlsson et al. In a typical synthesis, 3.75 g (17 mmol) of 2,2'-dipyridyl disulfide (Aldrithiol-2) was dissolved in 30 mL of ethanol and a solution of 0.87 mL of mercaptopropionic acid in 5 mL ethanol was injected dropwise. After 20 h of stirring at room temperature, the crude yellow oil product was isolated by rotary evaporation. The purified product (1.45 g, yield = 40%) was obtained from an alumina

column chromatography (eluent = CH<sub>2</sub>Cl<sub>2</sub>/EtOH 3:2 v/v). The product 1.45 g (6.8 mmol) is corresponding to 40% yield. The characterization of compound 1a is consistent with the literature reported data.<sup>14</sup>

2-[3-(trimethoxysilyl)-propyl]disulfanyl]-propionic acid, compound (1b), was prepared by dissolving compound 1a (1.51 g, 7 mmol) in 30 mL of THF, followed by a

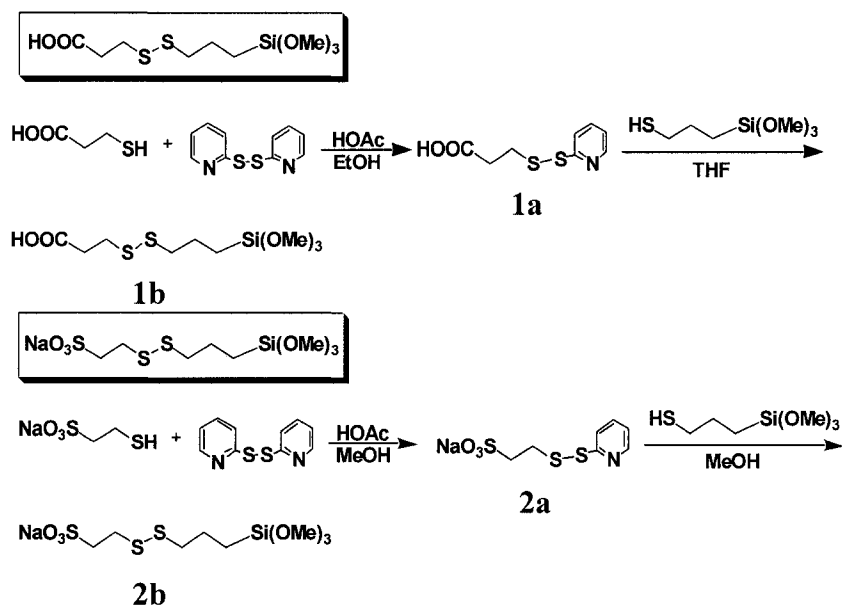


Figure 2-1. Schematic representation of the synthesis of organoalkoxysilane precursors

dropwise addition of MPTMS (1.1 g, 5.6 mmol). The resulting yellow solution was stirred under N<sub>2</sub> atmosphere for 12 h. After flash evaporation of the solvent, the yellow product was purified by silicagel column chromatography using EA/ Hexane in 1:2 ratio as eluent. The purified product (1 g) was isolated with a 60% yield. <sup>1</sup>H-NMR (CDCl<sub>3</sub>), δ 0.76 (t, 2H, CH<sub>2</sub>(1)), 1.81 (q, 2H, CH<sub>2</sub>(2)), 2.71 (t, 2H, CH<sub>2</sub>(5)), 2.81 (t, 2H, CH<sub>2</sub>(3)), 2.91 (t, 2H, CH<sub>2</sub>(4)), 3.60 (s, 1H, OCH<sub>3</sub>); <sup>13</sup>C-NMR (D<sub>2</sub>O), δ 10.25, 13.69, 23.75, 34.83, 36.98, 42.26, 180.99.

2-[3-(trimethoxysilyl)-propyl]disulfanyl]-ethanesulfonic acid, SDSP-TMS, (2b)

As depicted in Figure 2-1, 2,2'-Dipyridyl disulfide (8.82 g, 40.0 mmol) was dissolved in 50.0 mL of methanol, followed by an addition of 1.6 mL of glacial acetic acid as catalyst. To this mixture, 2-mercaptoethanesulfonic acid sodium salt (3.82 g, 20.0 mmol) in 30.0 mL of methanol was added dropwise in 30 min with stirring. The reaction mixture was protected



from light and stirred at room temperature overnight, followed by solvent evaporation under vacuum. The crude product was purified by dissolving in a small amount of methanol, followed by recrystallization in ethyl ether and dried under vacuum to yield compound 2a (5.14 g, yield = 94.0%).  $^1\text{H-NMR}$  (300 MHz; DMSO- $d_6$ ),  $\delta$  2.73 (*m*, 2H,  $\text{CH}_2$ ), 3.02 (*m*, 2H,  $\text{CH}_2$ ), 7.24 (*d*, 1H, ArH), 7.81 (*m*, 2H, ArH), 8.45 (*d*, 1H, ArH).

To synthesize 2-[3-(trimethoxysilyl)-propyl]disulfanyl-ethanesulfonic acid sodium salt (2b), compound 2a (1.36 g, 5.0 mmol) was dissolved in 20.0 mL of methanol with 1.0 mL of glacial acetic acid. To this mixture, (3-mercaptopropyl) trimethoxysilane (0.95 mL, 5.0 mmol) in 10.0 mL of methanol was added dropwise. The mixture was protected from light and stirred under nitrogen at room temperature overnight. The reaction was quenched and the solvent was evaporated under vacuum. The solid product was dissolved in a small amount of methanol, followed by ethyl ether precipitation. The purified product (5.14 g, yield = 74.7%) was collected by filtration and dried under vacuum.  $^1\text{H-NMR}$  (300 MHz;  $\text{D}_2\text{O}$ )  $\delta$  0.79 (*t*, 2H,  $\text{CH}_2(1)$ ), 1.83 (*q*, 2H,  $\text{CH}_2(2)$ ), 2.81 (*t*, 2H,  $\text{CH}_2(3)$ ), 3.03 (*t*, 2H,  $\text{CH}_2(5)$ ), 3.27 (*t*, 2H,  $\text{CH}_2(4)$ ), 3.60 (*s*, 7H,  $\text{OCH}_3$ ).

### Synthesis of MSN materials

Three organically functionalized mesoporous silica materials, MSN-COOH, MSN- $\text{SO}_3\text{H}$ , and MSN-SH, were prepared by adding an ethanolic solution (2 mL, 2.24 mmol) of CDSP-TMS, SDSP-TMS, and the commercially available MP-TMS, respectively, to an aqueous solution (480 mL) of CTAB (2.74 mmol), NaOH (7.00 mmol), and TEOS (22.40 mmol) at 80°C. The reaction mixture was stirred for 2 h. The solid products were isolated by filtration and washed thoroughly with methanol. The surfactant-removed materials were obtained by refluxing 1 g of the MSN material in 170 mL of methanolic solution of HCl (1 M) for 12 h. The resulting surfactant-removed material was isolated by filtration, washed extensively with methanol, and dried under vacuum. To obtain mesoporous silica material with free thiol groups, the surfactant extracted MSN material was added to 100.0 mL of 5%  $\text{NaHCO}_3(\text{aq})$  containing a disulfide reducing agent, dithiothreitol (DTT) (1.88 g, 12.2 mmol).

The mixture was stirred at room temperature for 4 h. The white product was then filtered and washed with water and methanol, following by vacuum drying.

#### Characterization of the Organic Functionalization of the MSN Materials

1. Powder XRD diffraction patterns of MSN-COOH, MSN-SO<sub>3</sub>H, and MSN-SH are summarized in Table 2-1. The data were collected on a Scintag XRD 2000 X-Ray diffractometer using Cu K $\alpha$  radiation. Low angle diffraction with a  $2\theta$  range of 1 to 10° was used to investigate the long-range order of the materials.

2. Surface area (SA) and Median Pore Diameter (MPD) were measured using a Micromeritics ASAP2000 sorptometer. Samples were degassed at 90 °C for 1 h and at 150 °C for 4 h. Nitrogen adsorption and desorption isotherms of the MSN materials were obtained at -196 °C. Specific surface areas and pore size distributions were calculated using the BrunauerEmmett-Teller (BET) and Barrett-Joyner-Halenda (BJH) method, respectively.

3. Particle morphology of these MSN materials was determined by scanning electron microscopy (SEM) using a JEOL 840A scanning electron microscope with 10 kV accelerating voltage and 0.005 nA of beam current for imaging. For obtaining the transmission electron microscopy (TEM) micrograph displayed in the main text, a small aliquot was taken from a suspension of MSN in methanol, and placed in a lacey carbon-coated TEM grid, which was pulled through the suspension and allowed to dry in air. The specimen was given no further treatment, as it appeared stable under beam bombardment.

4. TGA curves were recorded using a TA Instruments TGA 2950 thermogravimetric analyzer with a temperature ramp of 5° C/min under continuous flow of nitrogen (100 mL/min). The percentage of weigh loss when heating the samples of MSNs in the range of 1-1000°C is concluded in Table 2-2. In general, three or four distinct weight loss TGA profiles were found, including methanol, organic functional groups, and a small weight loss due to the dehydration of the surface hydroxyl groups.

5. The  $^{13}\text{C}$  spectra shown in the Figure 2-6 confirm the presence of the three organic functional groups in the MSN materials before the disulfide bond reductions. Solid-state  $^{13}\text{C}$  CP-MAS NMR spectra were obtained at 75.47 Mhz on a Bruker MSL300 spectrometer equipped with Bruker 4mm rotor MAS probe. Magic-angle sample spinning rate was maintained at 10 KHz. The NMR spectra consisted of between 2,000 and 6,000 acquisitions with cross polarization times of 3ms and pulse repetition times of 15s. All chemical shifts reported are referenced to liquid  $\text{SiMe}_4$  (TMS).

#### Quantification of chemically accessible surface-functionalized thiol coverage

All experiments were performed in triplicate, by reacting a predetermined amount of material (in the range of 20 to 25 mg) with a methanolic solution of excess 2, 2'-dipyridyl disulfide (44 mg, 0.2 mmol dissolved in 5 mL methanol).

### Results and Discussion

Our method involves the utilization of disulfide-containing organotrimethoxysilanes that have different anionic functional groups, such as 3-(3'-(trimethoxysilyl)-propyl-disulfanyl)-propionic acid (CDSP-TMS), 2-[3-(trimethoxy-silyl)-propyl-disulfanyl]-ethanesulfonic acid sodium salt (SDSP-TMS), and mercaptopropyl-trimethoxysilane (MP-TMS), to electrostatically match with cationic cetyltrimethylammonium bromide (CTAB) surfactant micelles in a NaOH-catalyzed condensation reaction of tetraethoxysilane (TEOS) as shown in Figure 2-2. We were inspired by the recent reports by Larsen and Magid,<sup>11</sup> where they observed the anionic lyotropic series ( $\text{citrate} < \text{CO}_3^{2-} < \text{SO}_4^{2-} < \text{CH}_3\text{CO}_2^- < \text{F}^- < \text{OH}^- < \text{HCO}_2^- < \text{Cl}^- < \text{NO}_3^- < \text{Br}^- < \text{CH}_3\text{C}_6\text{H}_4\text{SO}_3^-$ ) for interaction with the CTAB surfactant micelle based on the enthalpy of transfer of the salt from water to solutions of 0.1 M CTAB. They concluded that anions less hydrated than  $\text{Br}^-$ , such as sulfonate, will be able to replace  $\text{Br}^-$  and bind tightly to the cetyltrimethylammonium head group of the CTAB molecule thereby effectively mitigating the repulsion between these cationic head groups and stabilizing the micelle structure. Also, several recent reports<sup>12</sup> have also discovered that the long-range structure ordering of CTAB-templated mesoporous silicas could be improved by

the additions of various anions. The tightly bound (less hydrated) anions, such as acetate and  $\text{BF}_4^-$ , became incorporated in the silicate matrix due to their ability to compete with the silicate anions in displacing  $\text{Br}^-$  from the CTAB micelle.

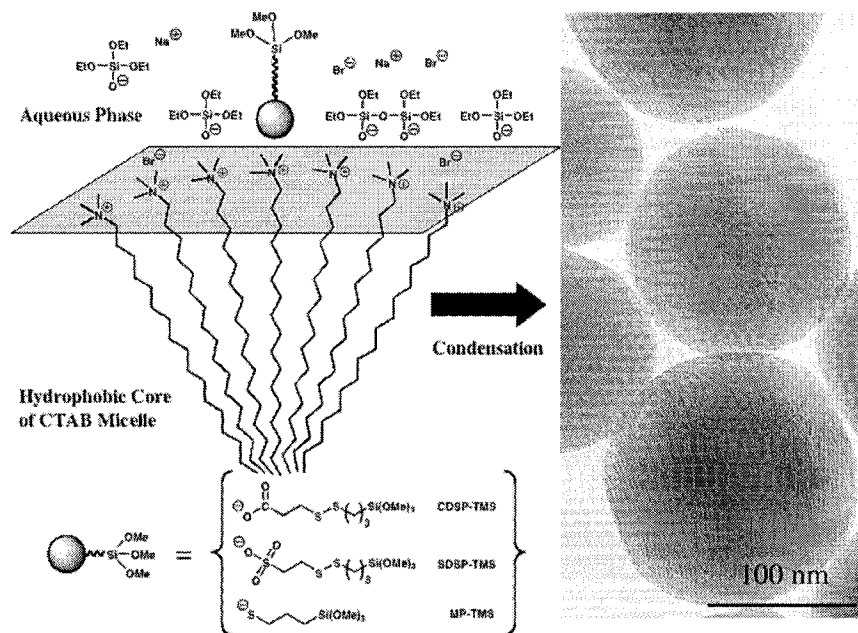


Figure 2-2. Schematic representation of the utilization of anionic organoalkoxysilane for controlling the functionalization of the MSN materials. The MCM-41 type mesoporous channels are illustrated by the parallel stripes shown in the TEM micrograph of the MSN-SH material.

The different electrostatic matching effects of various anionic organoalkoxysilanes, such as thiolate-, carboxylate-, and sulfonate-containing organoalkoxysilanes, to CTAB micelles in governing the degree of organic functionalization of the MCM-41 type mesoporous silica materials are investigated. First, two disulfide-containing organotrimethoxysilanes (CDSP-TMS and SDSP-TMS) with carboxylic and sulfonic acid groups, respectively, were synthesized via a synthetic approach outlined in Scheme 2-1.

These two compounds were synthesized via a simple thiol activation of 3-mercaptopropionic acid and 2-mercaptoethanesulfonic acid sodium salt with 2,2'-dipyridyl disulfide followed by a disulfide exchange reaction with mercaptopropyltrimethoxysilane.

Three organically functionalized mesoporous silica materials, MSN-COOH, MSN-SO<sub>3</sub>H, and MSN-SH, were prepared by adding an ethanolic solution (2 mL, 2.24 mmol) of CDSP-TMS, SDSP-TMS, and the commercially available MP-TMS, respectively, to an aqueous solution (480 mL, 80°C) of CTAB (2.74 mmol), NaOH (7.00 mmol), and TEOS (22.40 mmol, added at 80°C prior to the addition of organoalkoxysilanes). The reaction mixture was stirred for 2 h. The solid products were isolated by filtration and washed thoroughly with methanol. Surfactant-removed materials were obtained with an acid extraction. All three materials exhibited spherical particle shape with an average particle diameter of 200 nm (Figure 2-2 and 2-3).

Scheme 2-1

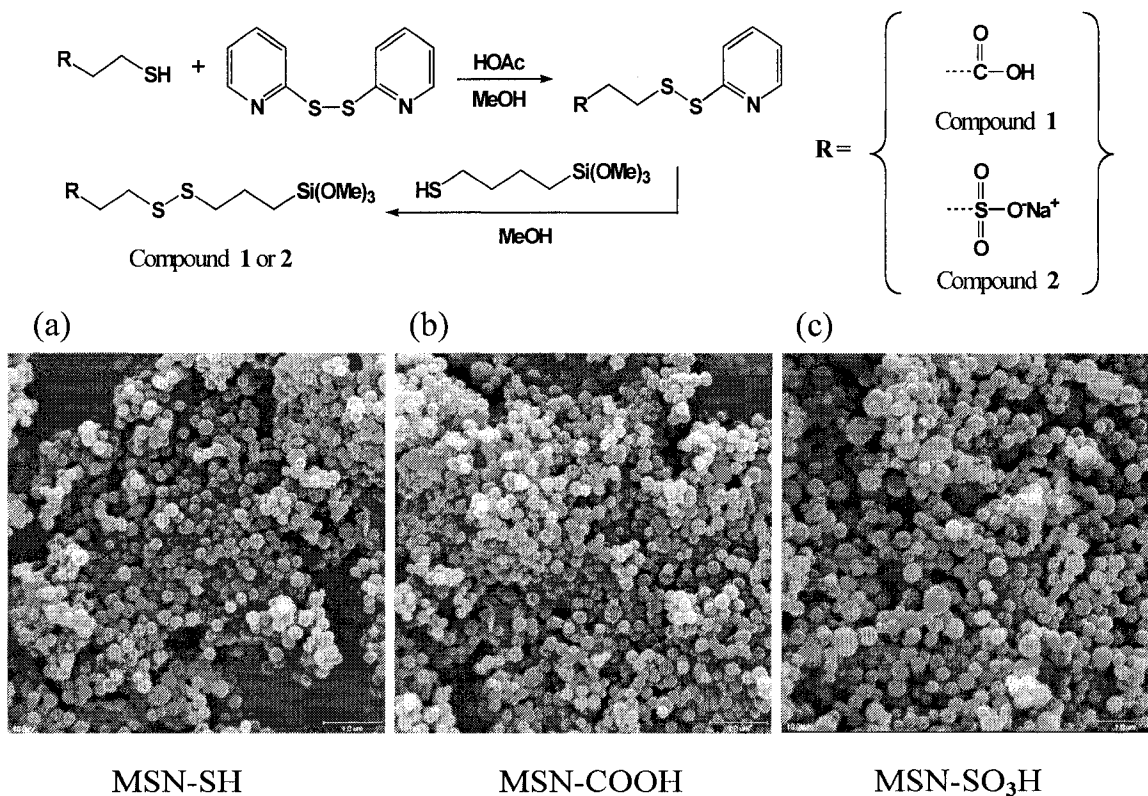


Figure 2-3. SEM images of MSN-SH (a), MSN-COOH (b) and MSN-SO<sub>3</sub>H (c). All three materials exhibited spherical particle morphology, with an average particle diameter of 200 nm. All images are presented using the same magnification (scale bar = 1 μm).

The mesoporous structures of these organically functionalized MSN materials were determined by nitrogen adsorption-desorption surface analysis (BET isotherms and BJH pore size distributions), TEM, and powder X-ray diffraction (XRD) spectroscopy.

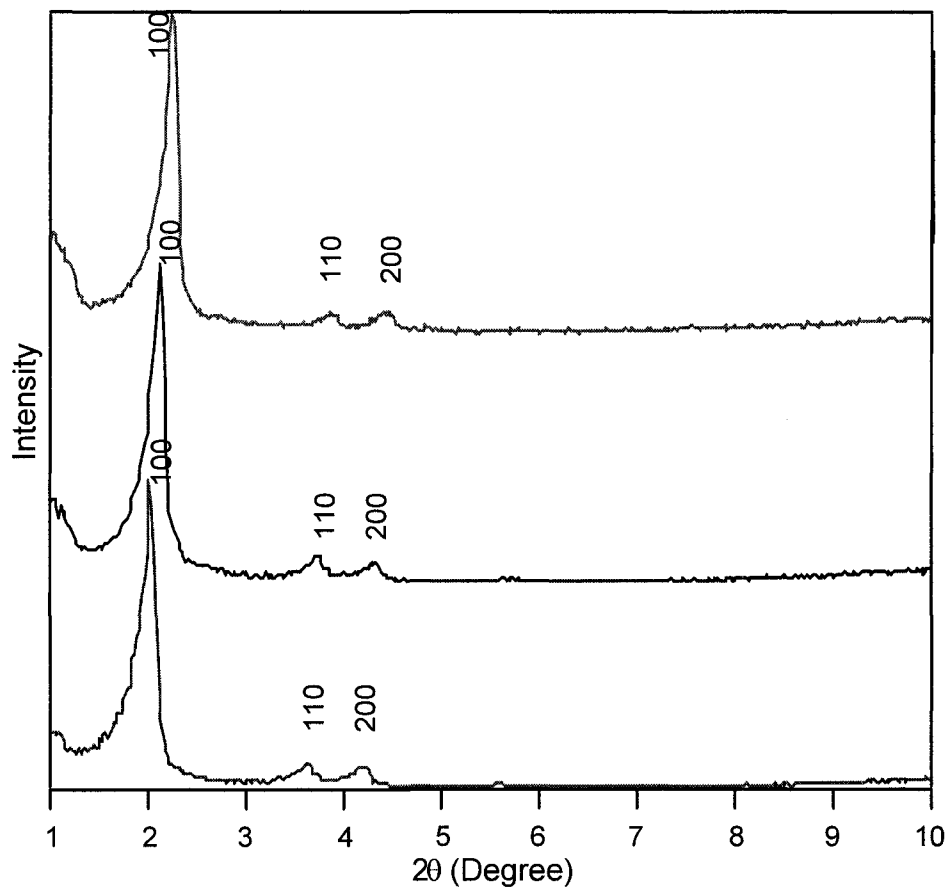


Figure 2-4. Powder XRD diffraction patterns of the MSN-SH (green), MSN-COOH (red) and MSN-SO<sub>3</sub>H (blue) materials after treatment with disulfide reducing agent (DTT).

These materials exhibited diffraction patterns characteristic of hexagonal MCM-41 silicas, including (100), (110), and (200) peaks (Figure 2-4). In addition, all three MSN materials exhibited type IV BET isotherms with similar average BJH pore diameters (Figure 2-5 and Table 2-1). Hexagonally packed mesoporous channels were clearly observed in the TEM micrographs of these MSNs (Figure 2-1). The existence of the organic functional groups was confirmed by <sup>13</sup>C solid state NMR spectroscopy (Figure 2-6).

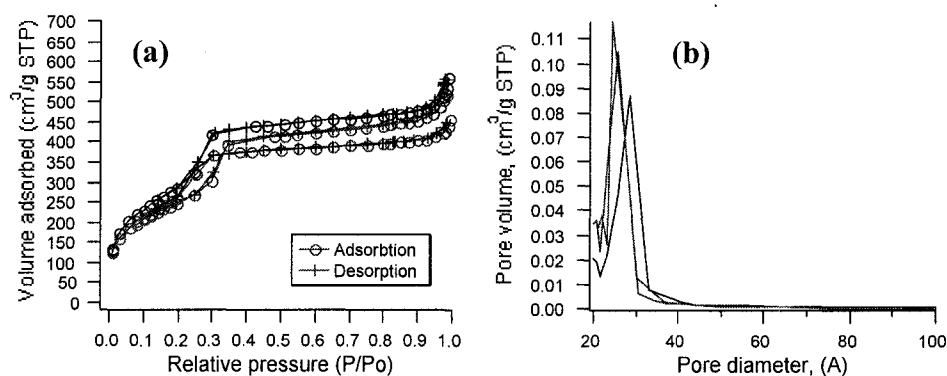


Figure 2-5. (a) Nitrogen sorption isotherms of the MSN-SH (green), MSN-COOH (red) and MSN-SO<sub>3</sub>H (blue) materials after treatment with disulfide reducing agent (DTT). (b) Pore size distributions of the MSN-SH, MSN-COOH and MSN-SO<sub>3</sub>H materials.

To quantify the amount of chemically accessible functional groups that are incorporated and oriented properly on the mesopore surfaces, we chemically converted the surface bound organic groups of the MSN-COOH and MSN-SO<sub>3</sub>H materials to thiol (-SH) by treating them with a disulfide reducing agent, dithiothreitol (DTT) as depicted in Figure 2-6.

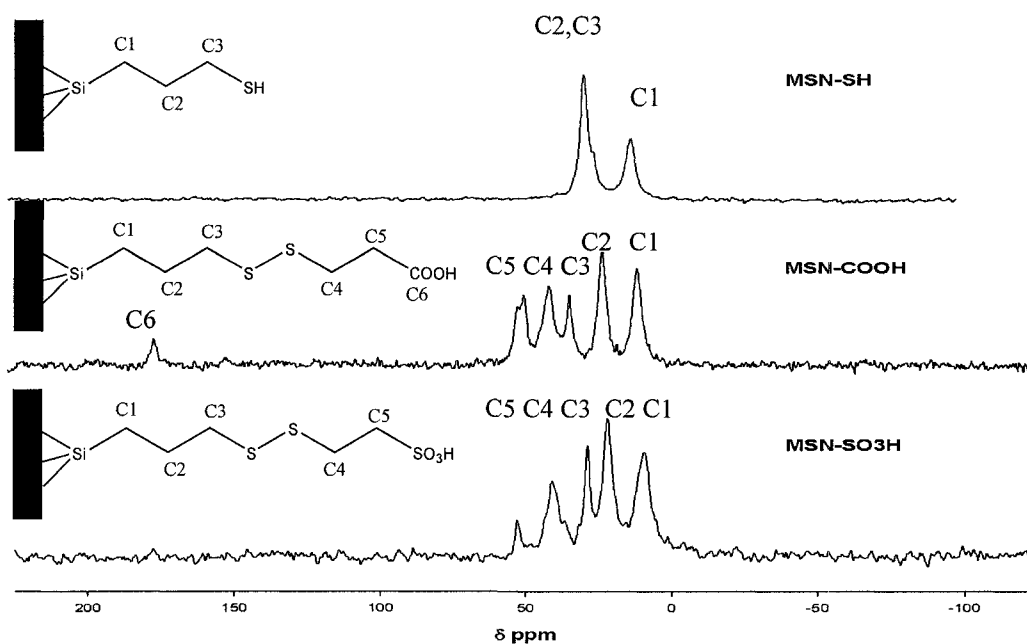


Figure 2-6. Solid state <sup>13</sup>C CP-MAS NMR spectra of the MSN-SH (up), MSN-COOH (middle) and MSN-SO<sub>3</sub>H (bottom).

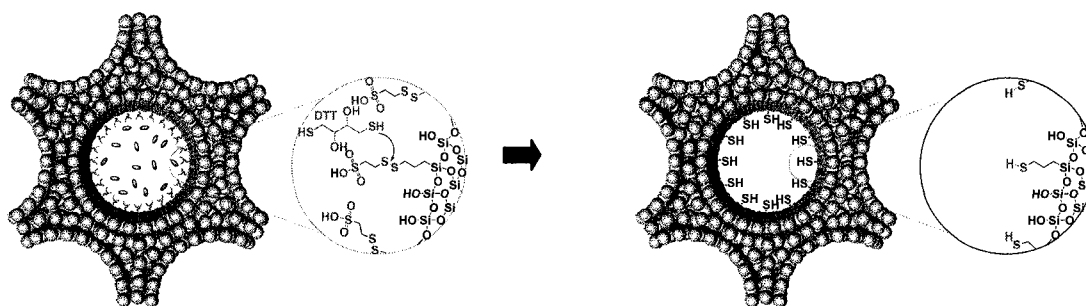


Figure 2-7. Schematic representation of the formation of thiol-functionalized mesoporous silica material (MSN-SO<sub>3</sub>H) via disulfide reduction with dithiothreitol (DTT).

As shown in Scheme 2-2, reactions of the resulting free thiol-functionalized materials with the 2,2'-dipyridyl disulfide gave rise to 2-pyridyldithio-derivatized surface functional groups along with a 2-pyridothione compound as the side product.

Table 2-1. Structural properties of the organically functionalized MSN materials.

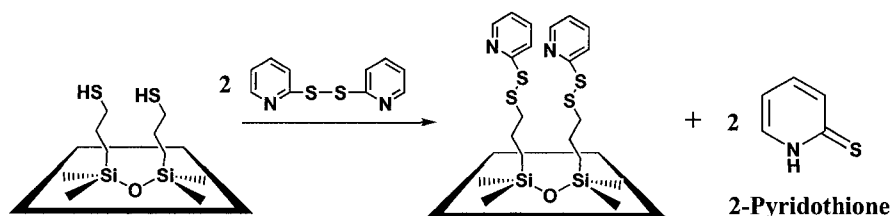
	Powder XRD			Nitrogen Sorption Isotherms		
	Low angle (Silica) (Å)			BET surface area (m <sup>2</sup> /g)	BET pore volume (mL/g)	BJH pore diameter (Å)
	<i>d</i> <sub>100</sub>	<i>d</i> <sub>110</sub>	<i>d</i> <sub>200</sub>			
MSN-SH	39.8	22.9	19.9	999	0.793	25.8
MSN-COOH	40.5	22.8	20.1	920	0.657	27.3
MSN-SO <sub>3</sub> H	43.8	24.4	20.9	863	0.755	28.1

Nitrogen sorption isotherms of the three MSN materials exhibited a sharp step starting at ca.  $p/p_0 = 0.38$ , as shown in Figure 2-5a with reversible type IV isotherms. (The inflection point is attributed to the commencement of pore filling from which the pore diameter can be roughly estimated).



Given that every surface-bound thiol that reacted with the 2,2'-dipyridyl disulfide would yield one 2-pyridothione molecule in solution, the amount of chemically accessible surface thiol functionality of these three materials could be quantified by measuring the concentration (UV/Vis absorbance) of the 2-pyridothione ( $\lambda_{\text{max}} = 343 \text{ nm}$ ,  $\epsilon = 8,080 \text{ M}^{-1}\text{cm}^{-1}$ )<sup>13</sup> in the supernatants of these reactions. The results showed that the solution concentrations of 2-pyridothione increased in the order of MSN-SH < MSN-COOH < MSN-SO<sub>3</sub>H, indicating that the surface concentration of the chemically accessible thiol functional group increases from MSN-SH ( $0.56 \pm 0.01 \text{ mmol/g}$ ), MSN-COOH ( $0.97 \pm 0.01 \text{ mmol/g}$ ), to MSN-SO<sub>3</sub>H ( $1.56 \pm 0.01 \text{ mmol/g}$ ).

Interestingly, the elemental analyses of these materials showed a decreasing trend in the weight % of sulfur and carbon among these materials (MSN-SH > MSN-SO<sub>3</sub>H > MSN-



Scheme 2-2

COOH) as summarized in Table 2-2.

Table 2-2. Elemental Analysis of the organically functionalized MSNs

Material	C %	H %	S %
MSN-SH	$13.23 \pm 0.01$	$2.74 \pm 0.01$	$10.09 \pm 0.01$
MSN-COOH	$8.60 \pm 0.01$	$2.33 \pm 0.01$	$5.98 \pm 0.01$
MSN-SO <sub>3</sub> H	$9.79 \pm 0.01$	$2.60 \pm 0.01$	$7.95 \pm 0.01$

In spite of a lower loading of organic functional groups in MSN-SO<sub>3</sub>H, the results suggested that the amount of the chemically accessible organic functional groups in MSN-SO<sub>3</sub>H is in fact higher than those of MSN-COOH and MSN-SH. Such a difference in the loading and spatial orientation of the organic functional groups could be attributed to the competition between the anionic species, i.e., Br<sup>-</sup>, silicates, and the anionic

organoalkoxysilane precursors (CDSP-TMS, SDSP-TMS and MP-TMS), for the cationic surfactants (CTAB). Indeed, the least hydrated sulfonate group-containing SDSP-TMS gave rise to the highest loading of chemically accessible organic groups. Furthermore, relative to the carboxylate group, the thiolate offered less stabilization of the CTAB micelle aggregates, and therefore yielded the lowest loading.

### Conclusions

Functionalization of mesoporous silica materials is an important prerequisite for further utilization of these materials in various applications. In the presented work we studied the possibility of gaining control over the amount of chemically accessible functionality on the interior or exterior surface of mesoporous silicas. Our results have shown that the amounts of chemically accessible organic functional groups present on MCM-41 silica particles and consequently on Mesoporous Silica Nanospheres (MSN) by utilizing a modified co-condensation reaction can be controlled. This fine-tuning can be achieved by carefully designing the matching between the surfactant head groups and the desired organic functional group precursors. We concluded that there is a synergy of factors influencing the micellar-silica interaction. Among these factors we were investigating:

- a). electrostatic interaction at the micellar rod-precursor head groups interface;
- b). size matching between the cationic head group of the surfactant and the organo-precursor head-group;
- c). binding affinities between different ionic species and the cationically charged CTAB micelle, based on published physical-chemistry studies of binding constants of such interactions .

### Acknowledgements

This research was supported by the U.S. Department of Energy, Office of Basic Energy Sciences, through the Catalysis Science Grant No. AL-03-380-011 and NSF (CHE-0239570).

## References

1. C. T. Kresge, M. E. Leonowicz, W. J. Roth, J. C. Vartuli, and J. S. Beck, *Nature (London)*, 1992, **359**, 710.
2. D. Zhao, J. Feng, Q. Huo, N. Melosh, G. H. Frederickson, B. F. Chmelka, and G. D. Stucky, *Science (Washington, D. C.)*, 1998, **279**, 548.
3. S. A. Bagshaw, E. Prouzet, and T. J. Pinnavaia, *Science (Washington, D. C.)*, 1995, **269**, 1242.
4. S. Inagaki, A. Koiwai, N. Suzuki, Y. Fukushima, and K. Kuroda, *Bull. Chem. Soc. Jpn.*, 1996, **69**, 1449.
5. (a) V. S. Y. Lin, C.-Y. Lai, J. Huang, S.-A. Song, and S. Xu, *J. Am. Chem. Soc.*, 2001, **123**, 11510. (b) D. R. Radu, C.-Y. Lai, J. W. Wiench, M. Pruski, and V. S. Y. Lin, *J. Am. Chem. Soc.*, 2004, **126**, 1640.
6. (a) S. Huh, H.-T. Chen, J. W. Wiench, M. Pruski, and V. S. Y. Lin, *J. Am. Chem. Soc.*, 2004, **126**, 1010. (b) A. Corma, *Chem. Rev.*, 1997, **97**, 2373. (c) J. M. Thomas, *J. Mol. Catal. A*, 1999, **146**, 77. (e) D. Brunel, A. C. Blanc, A. Galarneau, and F. Fajula, *Catal. Today*, 2002, **73**, 139, and references therein.
7. (a) C.-Y. Lai, B. G. Trewyn, D. M. Jeftinija, K. Jeftinija, S. Xu, S. Jeftinija, and V. S. Y. Lin, *J. Am. Chem. Soc.*, 2003, **125**, 4451. (b) N. K. Mal, M. Fujiwara, Y. Tanaka, T. Taguchi, and M. Matsukata, *Chem. Mater.*, 2003, **15**, 3385.
8. J. Liu, Y. Shin, Z. Nie, J. H. Chang, L.-Q. Wang, G. E. Fryxell, W. D. Samuels, and G. J. Exarhos, *J. Phys. Chem. A*, 2000, **104**, 8328, and references therein.
9. A. Stein, B. J. Melde, and R. C. Schroden, *Adv. Mater. (Weinheim, Ger.)*, 2000, **12**, 1403, and references therein.
10. M. H. Lim and A. Stein, *Chem. Mater.*, 1999, **11**, 3285.
11. (a) J. W. Larsen and L. J. Magid, *J. Am. Chem. Soc.*, 1974, **96**, 5774. (b) J. W. Larsen and L. J. Magid, *J. Phys. Chem.*, 1974, **78**, 834.
12. (a) K. J. Edler and J. W. White, *Chemistry of Materials*, 1997, **9**, 1226. (b) A. Okabe, T. Fukushima, K. Ariga, M. Niki, and T. Aida, *J. Am. Chem. Soc.*, 2004, **126**, 9013.
13. J. K. Yee, D. B. Parry, K. D. Caldwell, and J. M. Harris, *Langmuir*, 1991, **7**, 307.

14. Carlsson, J.; Drevin, H.; Axen, R. *Biochem. J.* **1978**, *173*, 723.

### Chapter 3. Molecular Recognition Inside of Multifunctionalized Mesoporous Silicas: Toward Selective Fluorescence Detection of Dopamine and Glucosamine

The paper was published in *The Journal of American Chemical Society*

*J. Am. Chem. Soc.* **2001**; *123*(46); 11510-11511

Lin, V. S.-Y.; **Lai, C.-Y.**; Huang, J.; Song, S.-A.; Xu, S.

Department of Chemistry, Iowa State University, Ames, Iowa 50011-3111

#### Abstract

Organofunctionalized MCM-41 silica pores could serve as synthetic scaffolds to mimic enzyme or antibody active sites for specific covalent and/or noncovalent interactions with target molecules. Herein, we report the design and synthesis of a fluorescence sensory system to study the molecular recognition events of biogenic molecules, such as dopamine and glucosamine, inside different functionalized mesoporous silica microenvironments.

#### Introduction

Structurally well-defined mesoporous silica materials, such as MCM-type silicas, with tunable pore size and narrow pore-size distribution have attracted much attention for their potential applications in adsorption, catalysis, separation, and sensing. Our design strategy took advantage of the size-sieving ability of the mesoporous silica framework as the supporting matrix to first incorporate an amine-sensitive *o*-phthalic hemithioacetal (OPTA) group on the pore-surface. Only small molecules with amino groups can diffuse into the pores and react with the OPTA group to give rise to highly fluorescent isoindole products as depicted in Figure 3-1. In contrast to the molecular imprinted micro- and/or mesoporous silica materials<sup>4</sup> where the selectivity was determined by the pore shape and the functional group density in each cavity, we prepared multifunctionalized pores to not only capture the target substrate molecules covalently but also provide different secondary noncovalent interactions. OPTA-derivatized mesoporous silica materials with various surface-bound

functional groups allow modulation of our sensory system to enhance the substrate selectivity by tuning substrate accessibility and pore hydrophobicity.

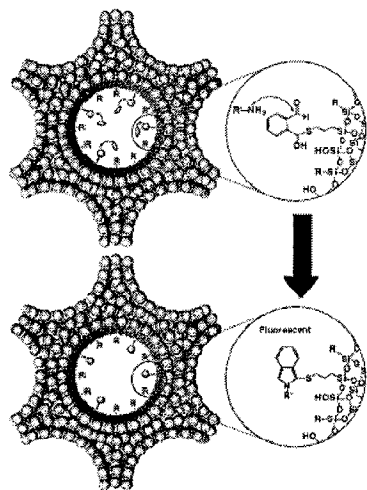


Figure 3-1. Schematic representation of the *o*-phthalic hemithioacetl (OPTA) functionalized mesoporous silica material and their fluorescent detection of amines. (R) siloxy, propyl, phenyl, or pentafluorophenyl groups; R'-NH<sub>2</sub>) dopamine or glucosamine).

## Materials and Methods

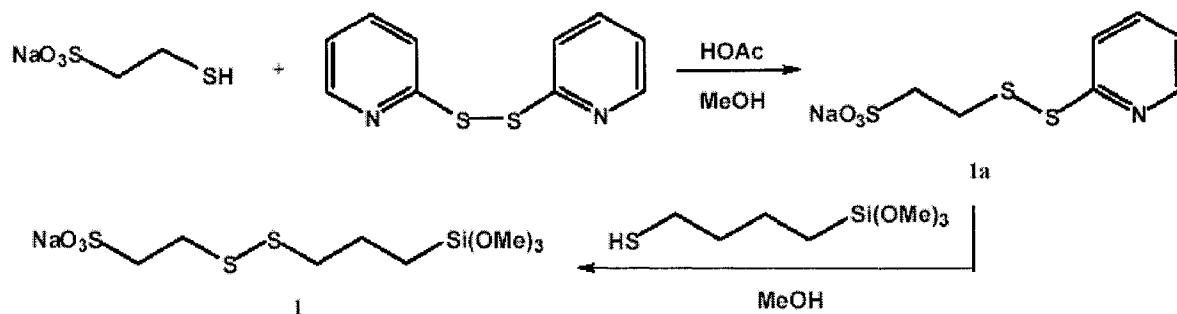
### Experimental Section

**Materials.** 3-Mercaptopropionic acid (99+%), 2,2'-dipyridyl disulfide (98%), (3-mercaptopropyl)trimethoxysilane (MPTES) (95%), 2-mercaptoethanesulfonic acid sodium salt (98%), cetyltrimethylammonium bromide (CTAB), tetraethyl orthosilicate (TEOS, 96%), pentafluorophenyltri trimethoxysilane (PFTES) and dithiothreitol (DTT) were purchased from Aldrich Chemical Co. (Milwaukee, WI). Acetic acid (Glacial), hydrochloric acid (37.4%), sodium hydroxide, ethanol (anhydrous), methanol (HPLC grade), tetrahydrofuran (HPLC grade), hexanes (pesticide grade) and ethyl ether (anhydrous) were obtained from Fisher Scientific Co. (Pittsburgh, PA). Nanopure water was deionized to 18.0 M $\Omega$ -cm in a Barnstead E-pure water purification system and used for the synthesis of MSN materials.

### Synthesis of Thiol-functionalized Mesoporous Silica Material (M1)

To synthesize the thiol-functionalized mesoporous silica (M1), we modified the well developed cetyltrimethylammonium bromide (CTAB) surfactant templated co-condensation method of tetraethoxysilane (TEOS) and organosiloxane precursors<sup>12</sup> by using compound 1 as the organosiloxane precursor depicted in scheme 3-1.

#### Synthesis of compound 1



Scheme 3-1

2,2'-Dipyridyl disulfide (8.82 g, 40.0 mmol) was dissolved in 50.0 mL of methanol; 1.6 mL of glacial acetic acid was added as catalyst. To this mixture, 2-Mercaptoethanesulfonic acid sodium salt (3.82 g, 20.0 mmol) in 30.0 mL of methanol was added dropwise in 30 min with stirring. The reaction mixture was protected from light and stirred at ambient temperature overnight, followed by solvent evaporation under vacuum. The crude product was repurified by dissolving in a small amount of methanol, followed by ethyl ether precipitation and dried under vacuum to yield compound 1a. 5.14 g, yield = 94.0%. <sup>1</sup>H-NMR (300 MHz; DMSO-d<sub>6</sub>),  $\delta$  2.73 (*m*, 2H, CH<sub>2</sub>), 3.02 (*m*, 2H, CH<sub>2</sub>), 7.24 (*d*, 1H, ArH), 7.81 (*m*, 2H, ArH), 8.45 (*d*, 1H, ArH).

To synthesize 2-[3-(trimethoxysilyl)-propyl]disulfanyl-ethanesulfonic acid sodium salt (1), compound 1a (1.36 g, 5.0 mmol) was dissolved in 20.0 mL of methanol with 1.0 mL of glacial acetic acid. To this mixture, (3-mercaptopropyl)trimethoxysilane (0.95 mL, 5.0 mmol) in 10.0 mL of methanol was added dropwise. The mixture was protected from light and stirred under nitrogen at room temperature overnight. The reaction mixture was

quenched and solvent was evaporated under vacuum. The solid obtained was dissolved in a small amount of methanol, followed by ethyl ether precipitation. The purified product was collected by filtration and dried under vacuum. 5.14 g, yield = 74.7%.  $^1\text{H-NMR}$  (300 MHz;  $\text{D}_2\text{O}$ )  $\delta$  0.79 (t, 2H,  $\text{CH}_2(1)$ ), 1.83 (q, 2H,  $\text{CH}_2(2)$ ), 2.81 (t, 2H,  $\text{CH}_2(3)$ ), 3.03 (t, 2H,  $\text{CH}_2(5)$ ), 3.27 (t, 2H,  $\text{CH}_2(4)$ ), 3.60 (s, 7H,  $\text{OCH}_3$ ).

### Synthesis of M1

Sodium hydroxide (0.83 g, 20.84 mmol) was dissolved in 80.0 mL ( $5.0 \times 10^3$  mmol) of deionized water, and 1.52 g (4.17 mmol) CTAB was added while stirring continuously to get a clear solution, and then compound 1 (1.24 g, 3.46 mmol) was added. The reaction mixture was stirred at ambient temperature for two hours, followed by dropwise addition of TEOS (6.97 mL, 31.27 mmol). The mixture was stirred vigorously at room temperature for two days followed by heating at  $90^\circ\text{C}$  for one day to improve the structural order. The as-synthesized M1 was filtered off, and then dried at  $90^\circ\text{C}$  under vacuum for 10 h. To remove the surfactant template, 3.0 g of as-synthesized M1 was refluxed for 24 hours in 9.0 mL 37.4% HCl / 324.0 mL MeOH. To obtain mesoporous silica material with free thiol groups (Figure 3-1), the surfactant extracted M1 (0.42 g) was added to 100.0 mL of  $\text{NaHCO}_3$  5% aqueous solution containing a disulfide reducing agent, dithiothreitol (DTT) (1.88 g, 12.2 mmol). The mixture was stirred at room temperature for 3 hours, then filtered off and washed with water. The white powder obtained was dried under vacuum at ambient temperature.

### Solid-State CP-MAS NMR Spectra

Solid-state  $^{29}\text{Si}$  and  $^{13}\text{C}$  CP-MAS NMR spectra were obtained at 59.62 MHz and 75.47 MHz, respectively, on Bruker MSL300 spectrometer equipped with Bruker 4mm rotor MAS probe. Magic-angle sample spinning rate was maintained at 4 KHz for  $^{29}\text{Si}$  measurements, and was increased to 10 KHz for  $^{13}\text{C}$  in order to minimize the spin band due to the high anisotropic chemical shifts of aromatic carbons. The NMR spectra consisted of between 2,000 and 6,000 acquisitions with cross polarization times of 1ms ( $^{29}\text{Si}$ ) and 3ms ( $^{13}\text{C}$ ) and pulse repetition times of 10s ( $^{29}\text{Si}$ ) and 15s ( $^{13}\text{C}$ ). All chemical shifts reported are referenced to liquid  $\text{Me}_4\text{Si}$  (TMS).



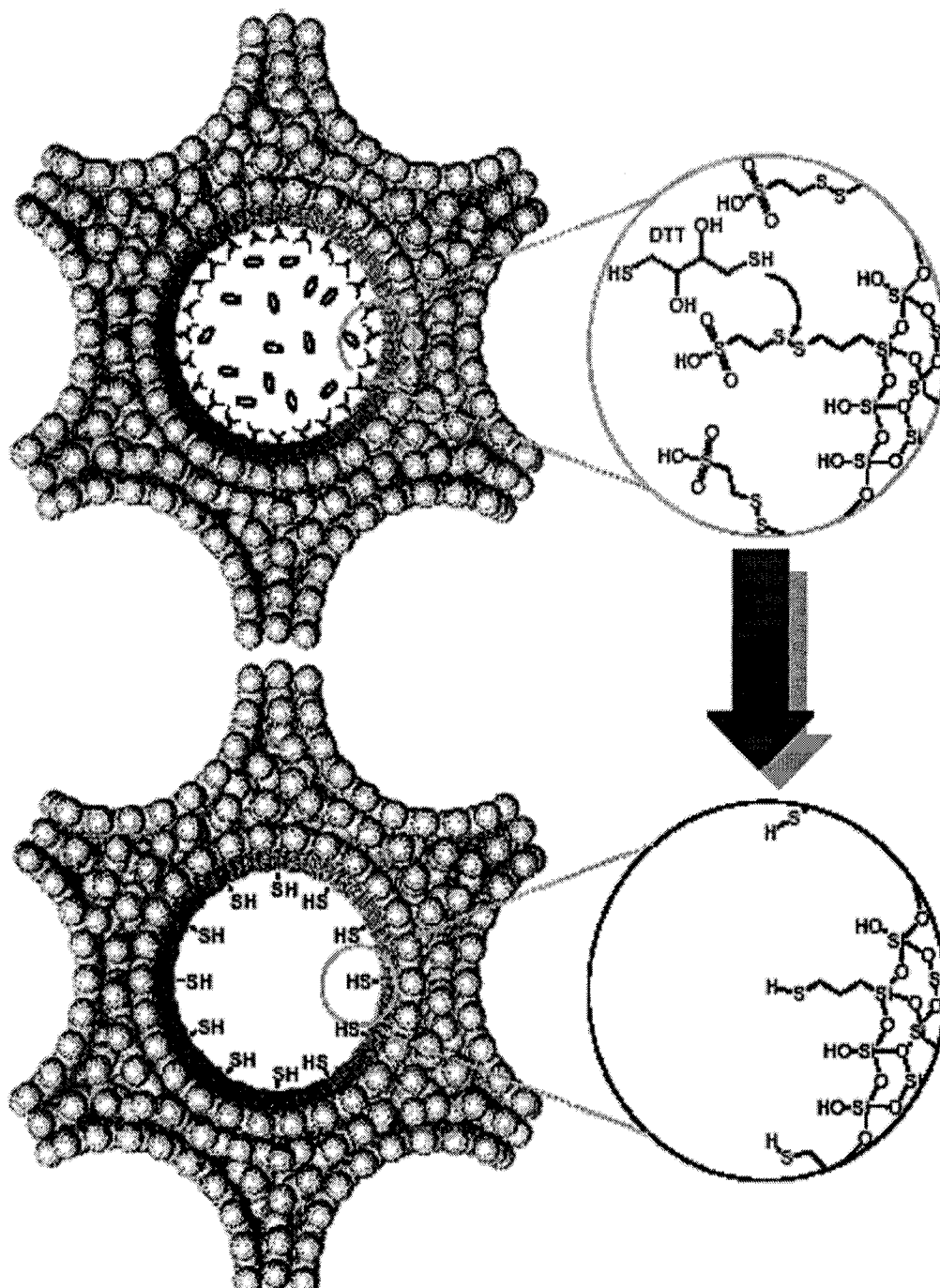


Figure 3-2. Schematic representation of the formation of thiol-functionalized mesoporous silica material via disulfide reduction with dithiothreitol.

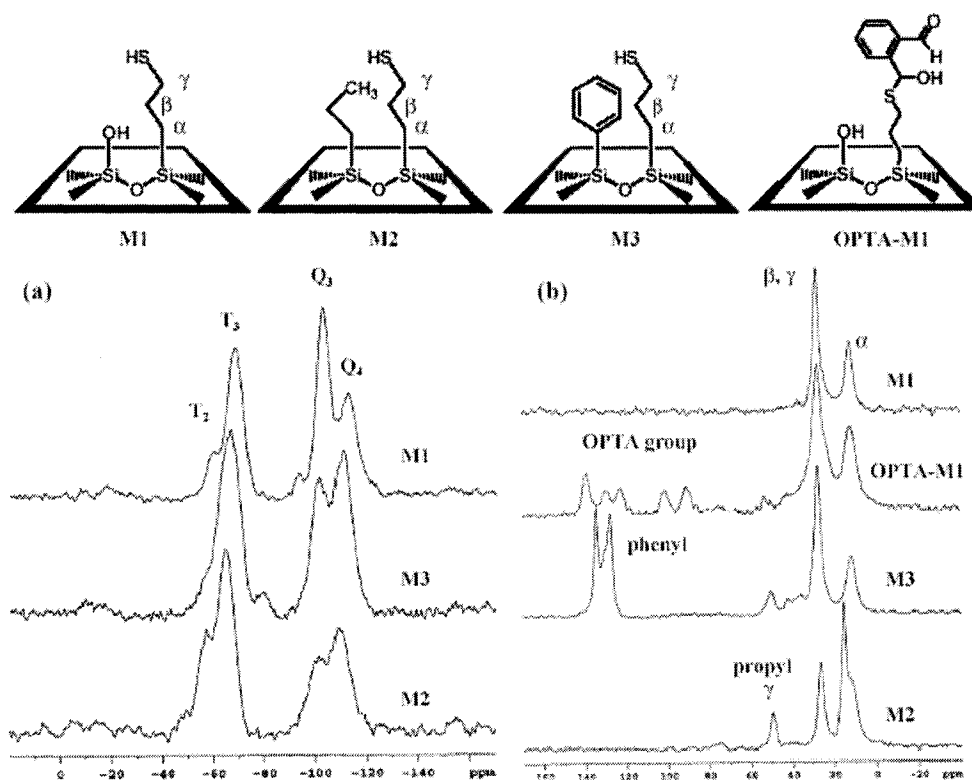


Figure 3-3. (a) Incorporation of the covalently linked organic groups was confirmed by  $^{29}\text{Si}$  CP NMR spectroscopy which showed distinct resonances for Si atoms in both siloxane [ $\text{Q}_x = \text{Si}(\text{OSi})_x(\text{OH})_{4-x}$ ,  $x = 2-4$ ] and organosiloxane [ $\text{T}_y = \text{RSi}(\text{OSi})_y(\text{OH})_{3-y}$ ,  $y = 1-3$ ] environments. (b)  $^{13}\text{C}$  CP-MAS NMR spectra of these materials further verified the multi-functional nature of the M2, M3, and OPTA-M1 indicating that all the organic functional groups were covalently linked to the silica surfaces

### Transmission Electron Microscopy (TEM) Analyses

The TEM image of thiol-functionalized mesoporous silica (M1) reveals the hexagonal array of uniform channels with the typical honeycomb appearance of MCM-41 type of mesoporous materials shown in Figure 3-4. The silica powder was mixed with acrylate embedding resin. Then the mixture in an embedding capsule was centrifuged and cured for 24 hours at 60 °C. The embedded block was microtomed to get thin sections of ca. 60 nm thick by using an ultramicrotome (RMC MT6000-XL) with a diamond knife. The floated sections were mounted on a 400 mesh Cu grid. The thin sections were observed with a transmission electron microscope (Hitachi H9000NA) operating at 300 kV and at 150,000 x electron optical magnification.

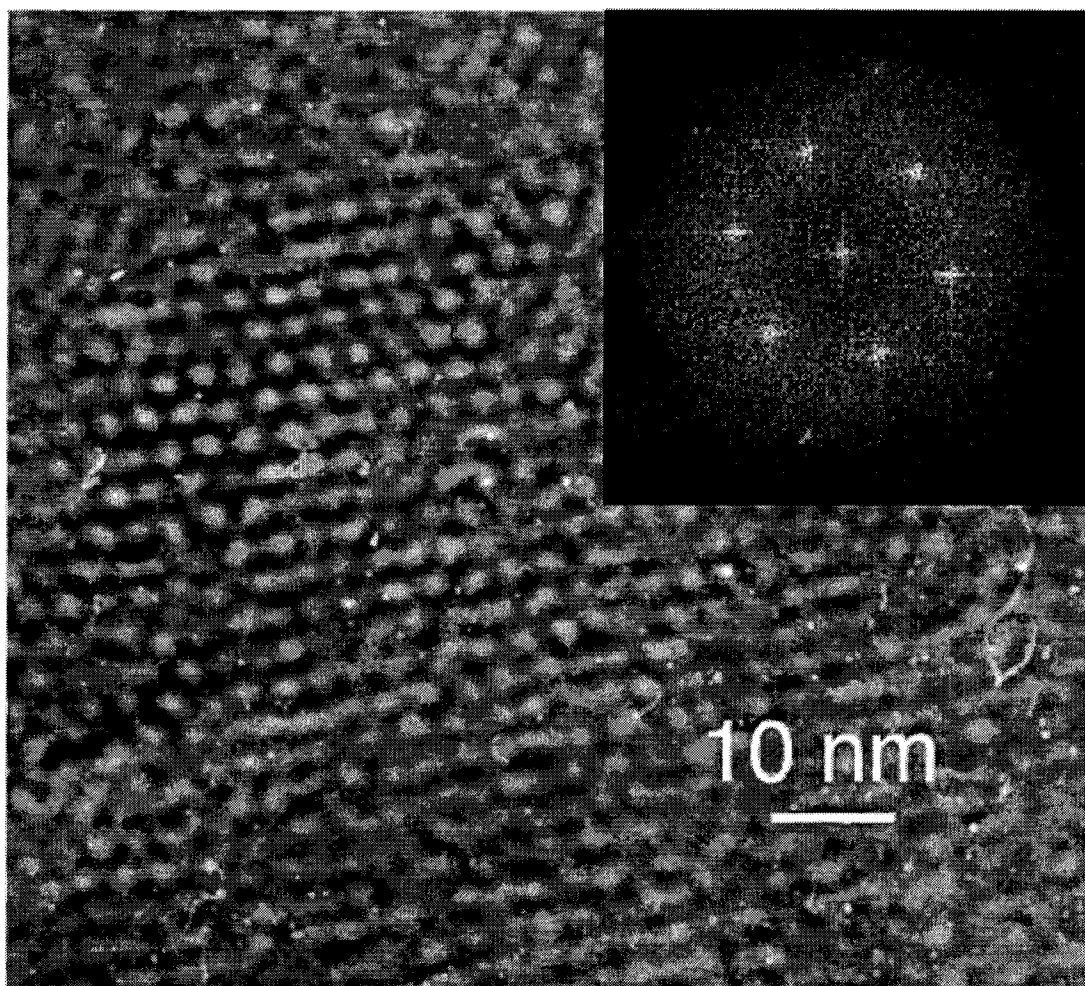
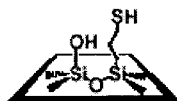


Figure 3-4. TEM image of a representative region of thiol-functionalized mesoporous silica (M1) after surfactant extraction and disulfide reduction. The inset shows the selected area electron diffraction pattern from this region.

#### BET Nitrogen Adsorption Isotherms and BJH Pore-size distributions

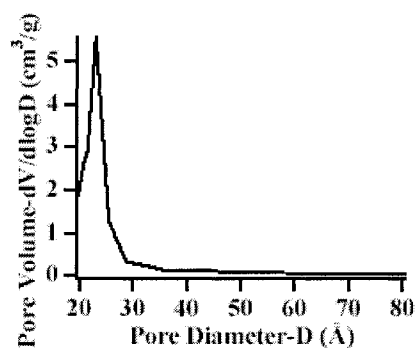
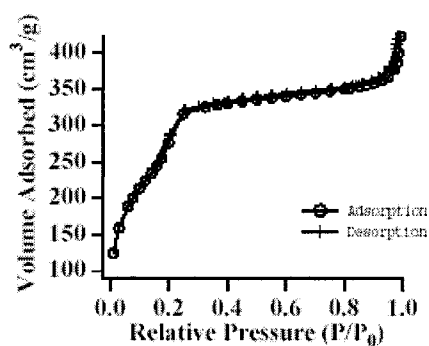
Surface area (SA) and Median Pore Diameter (MPD) were measured using a Micromeritics ASAP2000 sorptometer. Samples were degassed at 90 °C for 1 h and at 150 °C for 4 h. Nitrogen adsorption and desorption isotherms of the MSN materials were obtained at -196 °C. Specific surface areas and pore size distributions were calculated using the BrunauerEmmett-Teller (BET) and Barrett-Joyner-Halenda (BJH) method, respectively (Figure 3-5).

M1:

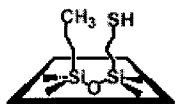


M1

Surface Area:  
964 m<sup>2</sup>/g  
Pore Diameter:  
23.1 Å

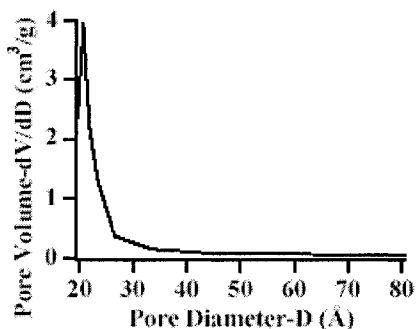
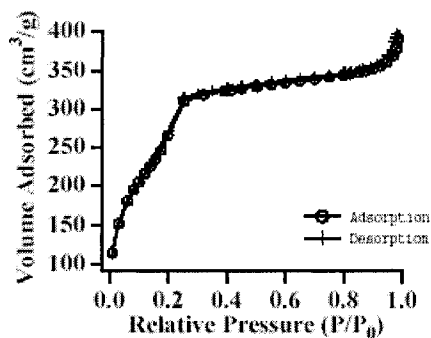


M2:

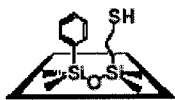


M2

Surface Area:  
926 m<sup>2</sup>/g  
Pore Diameter:  
20.6 Å

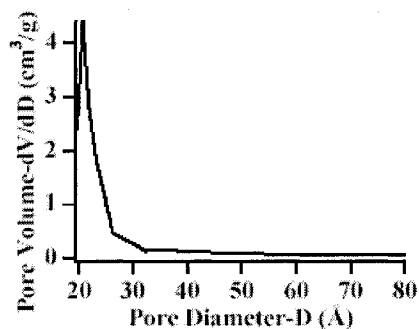
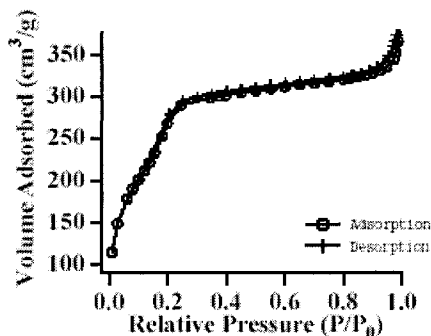


M3:

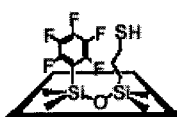


M3

Surface Area:  
936 m<sup>2</sup>/g  
Pore Diameter:  
20.6 Å



M4:



M4

Surface Area:  
939 m<sup>2</sup>/g  
Pore Diameter:  
20.7 Å

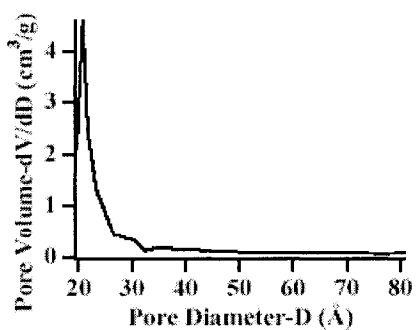
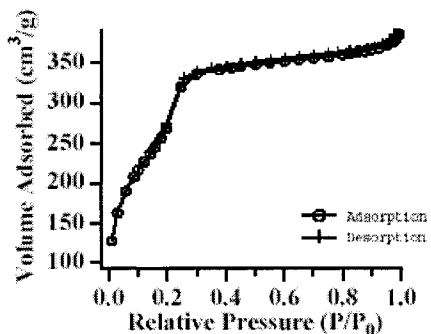


Figure 3-5. BET Nitrogen Adsorption Isotherms and BJH Pore-size distributions of multifunctionalized mesoporous materials, from M1 to M4.

## Fluorescence Detection of Dopamine and Glucosamine with Organo-functionalized Amorphous Silicas

An Amorphous silica material (0.1g) with a 200 m<sup>2</sup>/g BET surface area was purchased from Aldrich and treated with 3-mercaptopropyltrimethoxysilane (0.9 mL, 4.7 mmol) in a 10 mL of toluene solution. The reaction mixture was refluxed over night under nitrogen. The resulting thiol-grafted silica was filtered and washed thoroughly with toluene, ethanol, and deionized water. The product was then filtered and dried under vacuum for 12 h. Propyltrimethoxysilane (0.85mL, 4.7 mmol) and phenyltrimethoxysilane (0.9 mL, 4.7 mmol) were grafted separately to the thiolfunctionalized silica to yield two different multifunctionalized silicas, S2 (propyl- and thiol-derivatized silica) and S3 (phenyl- and thiol derivatized silica), respectively. The incorporation of all these organic groups was also confirmed by <sup>13</sup>C CP-MS solid-state NMR spectroscopy (same as Figure 3-3). The amounts of chemically accessible thiol groups (S2: 0.08 mmol/g; S3: 0.1 mmol/g) of these multifunctionalized silica materials were determined by the aforementioned method.<sup>13</sup> The CHNS elemental analyses of these materials indicated that the surface coverage of the propyl and phenyl groups are 0.054 mmol/g (S2) and 0.075 mmol/g (S3), respectively.

## Results and Discussion

To synthesize these multifunctionalized mesoporous silica materials, we first prepared a thiol-functionalized MCM-41 silica (M1) via a modified synthetic method of the well-developed surfactant templated co-condensation reaction.<sup>5</sup> The unoccupied silica pore surface of the M1 was further functionalized with propyl, phenyl, and pentafluorophenyl groups via postsynthesis grafting procedures<sup>6</sup> using propyltrimethoxysilane, phenyltrimethoxysilane, and pentafluorophenyltriethoxysilane<sup>7</sup> to yield three other multifunctionalized organomesoporous silica materials, M2, M3, and M4, respectively.<sup>8</sup> The characterization of these materials is summarized in Table 3-1.

Table 3-1. Characterization of Multifunctionalized Mesoporous Silicas

	BET surface area <sup>a</sup> (m <sup>2</sup> /g)	BJH pore diameter <sup>a</sup> (Å)	chemically accessible thiol density <sup>b</sup> (mmol/g)	amount of the grafted group <sup>c</sup> (mmol/g)
M1	964	23.1	1.5	
M2	926	20.6	0.046	1.5
M3	936	20.6	0.042	1.0
M4	939	20.7	0.062	1.2

<sup>a</sup> See experimental section for the adsorption isotherms and pore size distributions. <sup>b</sup> Chemically accessible thiol densities were determined by measuring the solution concentration of the side product (pyridine-2-thione) generated from the reaction of the pore-surface thiols with 2,2'-dipyridyl disulfide.<sup>9</sup> <sup>c</sup> Measured by CHNS elemental analyses.

Phthalic dicarboxaldehyde (*o*-phthalaldehyde, OPA) was introduced to suspensions of these thiol-containing multifunctionalized mesoporous silicas in a neutral buffer solution to form the amine-sensitive *o*-phthalic hemithioacetal-derivatized materials, OPTA-MX (X = 1 to 4). Incorporation of the OPTA groups was confirmed by <sup>13</sup>C CP-MAS NMR spectroscopy (see experimental section). The resulting OPTA-silica powder was dispersed in buffer for the fluorescence sensing experiments of dopamine or glucosamine. In contrast to the reported results of multi-functionalized mesoporous silicas, Figure 3-6a,b shows that the reaction rates of the nonporous silica surface-bound OPTA groups with dopamine and glucosamine are almost the same. Despite of the different surface phenyl groups), the fluorescence intensity of all three materials (OPTA-SX, X = 1 to 3) increased rapidly and reached their plateaus within 5 min. Also, in the concentration studies, all OPTA-SX (X = 1 to 3) amorphous silica materials showed similar changes of fluorescence intensity with the increasing concentration of dopamine or glucosamine (Figure 3-6c,d).

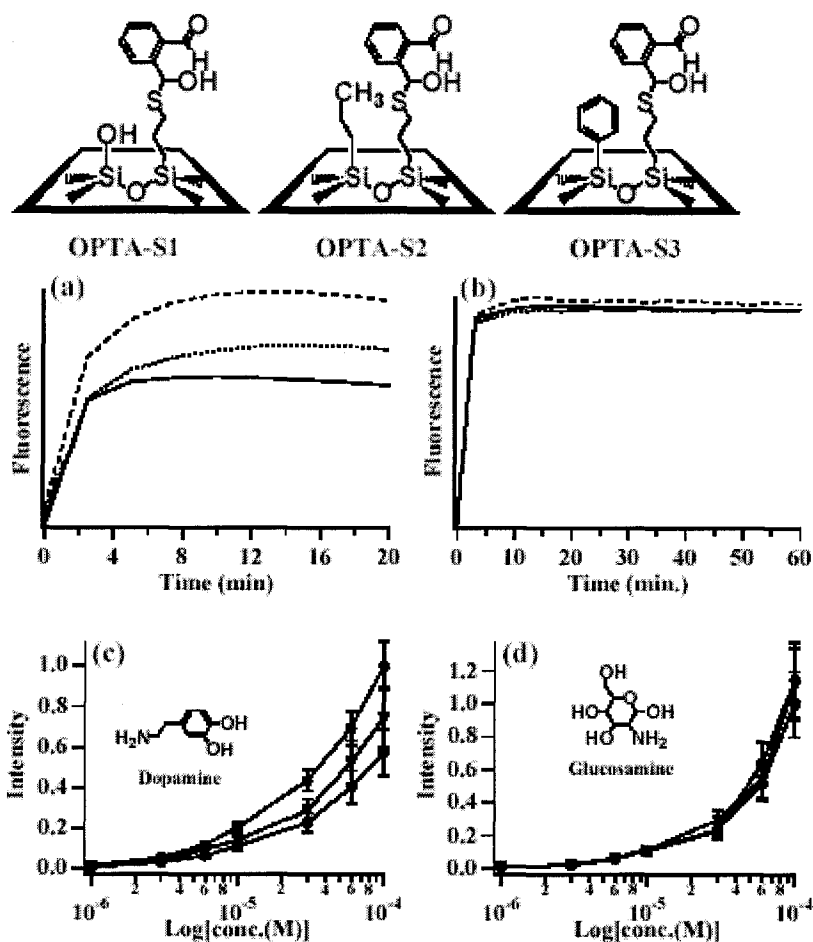


Figure 3-6. Kinetic measurements of the fluorescence detection of dopamine (a) and glucosamine (b) with OPTA-derivatized amorphous silicas grafted with secondary functional groups, such as silanol (S1: solid line), propyl (S2: dotted line), and phenyl (S3: dashed line) groups. Fluorescence increase of OPTA-SX (X = 1:●; 2: ▽ ; 3: Δ) as a function of dopamine (c) and glucosamine (d) concentrations.

In contrast to the instantaneous completion of the homogeneous reaction of 2-mercaptoethanol, OPA, and dopamine or glucoseamine to form a highly fluorescence isoindole, the reactions of dopamine (30  $\mu$ M) with all four of our OPTA-derivatized mesoporous silicas exhibited slower reaction rates (Figure 3-7a). For OPTA-M1, the increase of fluorescence intensity at the emission  $\lambda_{\max}$  of isoindole (440 nm) reached a plateau indicating the completion of the reaction in about 10 min. In contrast to the dopamine experiment, OPTA-M1 treated with 600  $\mu$ M glucosamine took about 2 h for the reaction to proceed to completion (Figure 3-7b). The reaction rate of glucosamine is at least 1 order of

magnitude slower than that of dopamine. Since dopamine and glucosamine are similar in their sizes and reactivities toward OPTA in homogeneous solutions,<sup>10,11</sup> the large difference in reaction rates between dopamine and glucosamine could not be explained by the size-sieving effect of these functionalized mesoporous materials. Conceivably, the significantly slower reaction rates of glucosamine could be attributed to a strong dipolar interaction between the abundant hydroxy groups of glucosamine with the pore surface silicates leading to a slower diffusion process within the pores. In addition, as the silicate walls are functionalized with increasingly hydrophobic substituents (OPTA-MX, X = 2 to 4), the diffusion rates for both dopamine and glucosamine are slowed (Figure 3-7a,b). The fluorescence intensity of these OPTA-derivatized mesoporous silicas treated with dopamine and glucosamine also varies dramatically depending on the pore environment (Figure 3-7c,d). In our study of dopamine binding, the measured fluorescence intensity of OPTA-M1 increased with the increasing concentration of dopamine, but for the more hydrophobic OPTA-MX (X = 2 to 4) materials, the change of fluorescence intensity was smaller than that of OPTA-M1. The reaction rates of dopamine binding are clearly slower in these materials. Furthermore, the OPTA-M4/dopamine binding gives a significantly higher increase of fluorescence intensities at all concentrations in comparison with that of OPTA-M3 and OPTA-M4. This observation strongly suggested that the pentafluorophenyl-functionalized mesopores of the OPTA-M4 were more reactive and preferred by dopamine compared to the propyl- and phenyl-functionalized pores of the OPTA-M2 and OPTA-M3 materials. Since both the average pore sizes and the surface coverage of the thiol functionality of these materials (MX, X = 2 to 4) are very similar (Table3-1), the large difference in binding behaviors is not likely due to the slight variation in the amount of chemically accessible thiol groups or the pore size of the functionalized mesopores of these materials. Compared with the phenyl-functionalized OPTA-M3, the better  $\pi$ - $\pi$  donor/acceptor type of stacking effect between the catechol rings of dopamine molecules and the pentafluorophenyl moieties of the OPTA-M4 silica could induce a faster and more favorable diffusion of dopamine to enter their functionalized mesopores. The hydrophobic propyl-functionalized OPTA-M2 material discourages the intercalation of dopamine. The same fluorescence study for glucosamine binding to OPTA-M1 at various concentrations showed similar large increases in



fluorescence intensity (Figure 3-7d). In contrast to dopamine binding, the propyl-, phenyl-, and pentafluorophenyl-functionalized OPTA-MX (X = 2 to 4) materials showed only similar small increases of fluorescence intensities with increasing glucosamine concentrations. These data further support the possibility that the nonaromatic glucosamine molecules could not easily diffuse into either the propyl-, phenyl-, or pentafluorophenyl-functionalized mesopores to react with the OPTA groups due to the hydrophobic environment inside the pores.

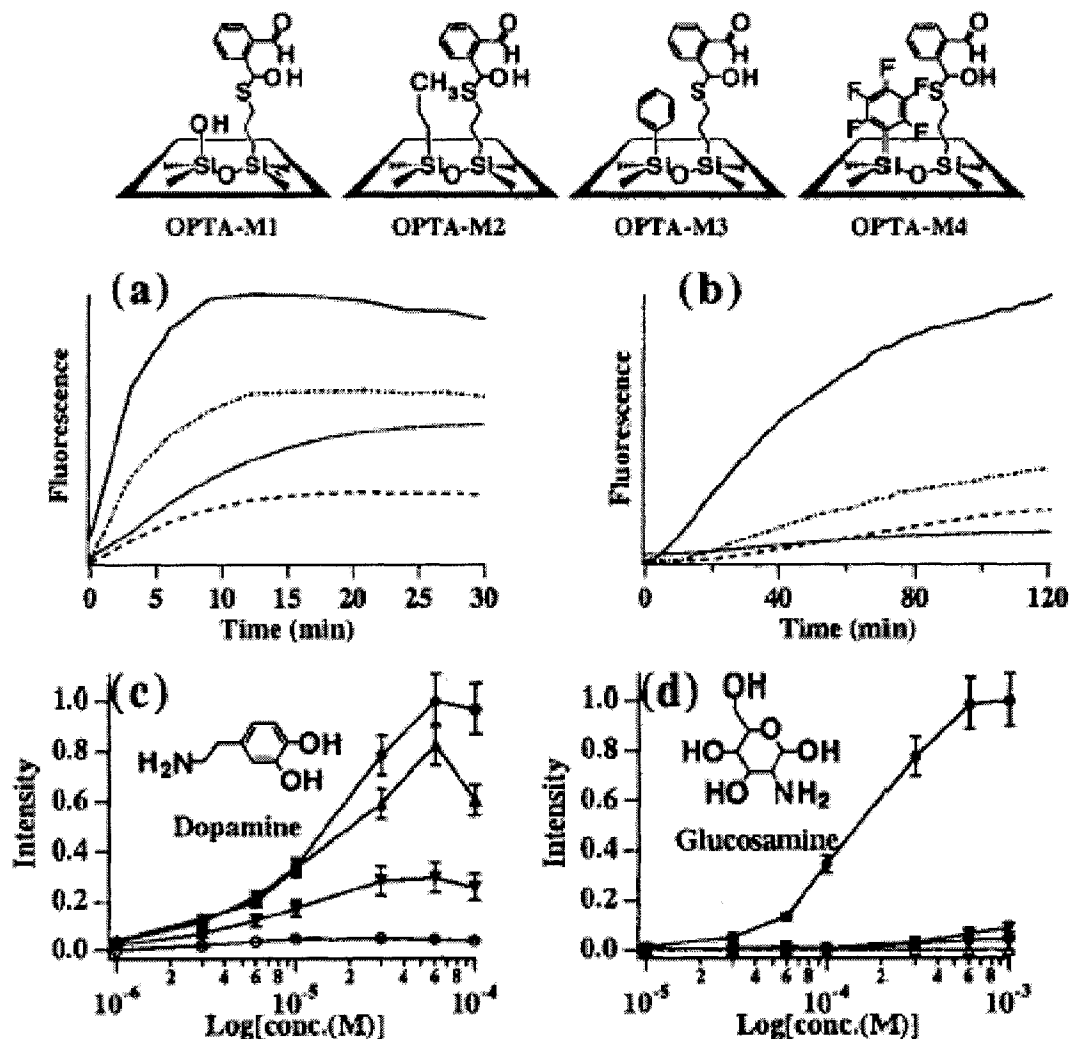


Figure 3-7. Kinetic measurements of the fluorescence detection of dopamine (a) and glucosamine (b) with OPTA-derivatized mesoporous silicas grafted with secondary functional groups, such as silanol (M1: solid line), propyl (M2: dotted line), phenyl (M3: dashed line), and pentafluorophenyl (M4: dash-dotted line) groups. Fluorescence increase of OPTA-MX (X) = 1 (●); 2 (○); 3 (▽); 4 (Δ) as a function of dopamine (c) and glucosamine (d) concentrations.

## Conclusions

In this study, we have demonstrated that selective molecular recognition of two multifunctional molecules with similar sizes and functionalities can be achieved not by shape recognition but by creating a multifunctionalized mesopore as the "active site" with combinations of covalent (isoindole formation) and noncovalent interactions (hydrophobic and  $\pi$ - $\pi$  interactions). The presented selectivity was not observed in the amorphous silica systems grafted with the same organofunctionalities, such as propyl and phenyl groups. Unlike the large difference in the increases of fluorescence intensity in the cases of dopamine and glucosamine binding to the OPTA-derivatized mesoporous silicas with different secondary functional groups, such as propyl and phenyl groups, the presence of the same hydrophobic functional groups here apparently did not significantly perturb the kinetic profiles of dopamine/glucosamine reacting with the amorphous silicas decorated with the same functional groups (see Figure 3-6). These results support our hypothesis that the multifunctionalization of a material with size and structurally well-defined, meso-scale pores is an important prerequisite for further developing new types of sensors or catalysts with highly selective molecular recognition sites within a rigid scaffold that could mimic biological active sites. Therefore, we envision that these multifunctionalized mesoporous silicas could serve as new materials for developing highly selective sensors and catalysts.

## Acknowledgements

The authors thank the Office of Biotechnology, Iowa State University for financial support of this work.

## References

1. C. T. Kresge, M. E. Leonowicz, W. J. Roth, J. C. Vartuli, and J. S. Beck, *Nature (London)*, 1992, **359**, 710.
2. Kresge, C. T.; Leonowicz, M. E.; Roth, W. J.; Vartuli, J. C.; Beck, J. S. *Nature* **1992**, 359, 710. (b) Zhao, D.; Feng, J.; Huo, Q.; Melosh, N.; Frederickson, G. H.; Chmelka,

- B. F.; Stucky, G. D. *Science* **1998**, *279*, 548. (c) Prouzet, E.; Pinnavaia, T. J. *Angew. Chem., Int. Ed. Engl.* **1997**, *36*, 516. (d) Inagaki, S.; Fukushima, Y.; Kuroda, K. *J. Chem. Soc., Chem. Commun.* **1993**, 680.
3. Liu, J.; Shin, Y.; Nie, Z.; Chang, J. H.; Wang, L.-Q.; Fryxell, G. E.; Samuels, W. D.; Exarhos, G. J. *J. Phys. Chem. A* **2000**, *104*, 8328.
4. Simons, S. S., Jr.; Johnson, D. F. *Anal. Biochem.* **1978**, *90*, 705. (b) Simons, S. S., Jr.; Johnson, D. F. *J. Org. Chem.* **1978**, *43*, 2886. (c) Dai, F.; Burkert, V. P.; Singh, H. N.; Hinze, W. L. *Microchem. J.* **1997**, *57*, 166.
5. (a) Dai, S.; Burleigh, M. C.; Shin, Y.; Morrow, C. C.; Barnes, C. E.; Xue, Z. *Angew. Chem., Int. Ed. Engl.* **1999**, *38*, 1235. (b) Katz, A.; Davis, M. E. *Nature* **2000**, *403*, 286. (c) Shin, Y.; Liu, J.; Wang, L.-Q.; Nie, Z.; Samuels, W. D.; Fryxell, G. E.; Exarhos, G. J. *Angew. Chem., Int. Ed.* **2000**, *39*, 2702. (d) Wulff, G.; Heide, B.; Helfmeier, G. *J. Am. Chem. Soc.* **1986**, *108*, 1089.
6. (a) Lim, M. H.; Blanford, C. F.; Stein, A. *Chem. Mater.* **1998**, *10*, 467. (b) Fowler, C. E.; Burkett, S. L.; Mann, S. *Chem. Commun.* **1997**, 1769. (c) Hall, S. R.; Fowler, C. E.; Mann, S.; Lebeau, B. *Chem. Commun.* **1999**, 201. For detailed procedure and the TEM image of M1, please see experimental section.
7. For examples of mesoporous silica materials with organosiloxane groups incorporated via postsynthesis grafting, see: (a) Moller, K.; Bein, T. *Chem. Mater.* **1998**, *10*, 2950. (b) Stein, A.; Melde, B. J.; Schroden, R. C. *Adv. Mater.* **2000**, *12*, 1403.
8. Frohn, H. J.; Giesen, M.; Klose, A.; Lewin, A.; Bardin, V. V. *J. Organomet. Chem.* **1996**, *506*, 155.
9. For detailed <sup>29</sup>Si and <sup>13</sup>C CP-MAS NMR peak assignments of these organofunctionalized silicas, see experimental section. (a) Yee, J. K.; Parry, D. B.; Caldwell, K. D.; Harris, J. M. *Langmuir* **1991**, *7*, 307. (b) Millot, M. C.; Seville, B.; Mahieu, J. P. *J. Chromatogr.* **1986**, *354*, 155.
10. (a) Yui, Y.; Kawai, C. *J. Chromatogr.* **1981**, *206*, 586. (b) Mell, L. D., Jr.; Dasler, A. R.; Gustafson, A. B. *J. Liq. Chromatogr.* **1978**, *1*, 261.

11. (a) Altmann, F. *Anal. Biochem.* **1992**, *204*, 215. (b) Dominguez, L. M.; Dunn, R. S. *J. Chromatogr. Sci.* **1987**, *25*, 468. (c) Carroll, S. F.; Nelson, D. R. *Anal. Biochem.* **1979**, *98*, 190.
12. (a) Lim, M. H.; Blanford, C. F.; Stein, A. *Chem. Mater.* **1998**, *10*, 467. (b) Fowler, C. E.; Burkett, S. L.; Mann, S. *Chem. Commun.* **1997**, 1769. (c) Hall, S. R.; Fowler, C. E.; Mann, S.; Lebeau, B. *Chem. Commun.* **1999**, 201.
13. See Table 1 of the paper and the following reference articles: (a) Yee, J. K.; Parry, D. B.; Caldwell, K. D.; Harris, J. M. *Langmuir* **1991**, *7*, 307. (b) Millot, M. C.; Sebille, B.; Mahieu, J. P. *J. Chromatogr.* **1986**, *354*, 155.

Chapter 4. Gatekeeping Layer Effect: A Poly(lactic acid)-coated Mesoporous Silica  
Nanosphere-Based Fluorescence Probe for Detection of Amino-Containing  
Neurotransmitters

The paper was published in *The Journal of American Chemical Society*

*J. Am. Chem. Soc.* **2004**; *126*(6); 1640-1641

Radu, D. R.; Lai, C.-Y.; Wiench, J. W.; Pruski, M.; Lin, V. S.-Y.

Department of Chemistry, Iowa State University, Ames, Iowa 50011-3111

### Abstract

Selective functionalization of the exterior and interior surface of structurally uniform mesoporous materials, such as MCM- or SBA-type of silicas with different organic moieties<sup>2</sup> allows precise regulation of the penetration of selective molecules with certain sizes and chemical properties into the nano-scale pores. Herein, we report the synthesis and characterization of a poly(lactic acid)-coated, MCM-41 type mesoporous silica nanosphere (PLA-MSN) material that can serve as a fluorescence sensor for selective detection of amino-containing neurotransmitters under physiological condition. By utilizing the PLA layer as a *gatekeeper* to regulate the penetration of molecules in and out of the nano-scale pores, we investigated the molecular recognition events between several structurally simple neurotransmitters, i.e., dopamine, tyrosine, and glutamic acid and a pore surface-anchored *o*-phthalic hemithioacetal (OPTA) group.

### Introduction

Synthesizing molecular receptors that can differentiate various extracellular amino acid-based neurotransmitters has long been a research challenge. For example, dopamine and glutamic acid are two essential neurotransmitters that are often simultaneously exchanged between various neural cells.<sup>1</sup> Despite their importance in understanding

interneuronal chemical communication, to the best of our knowledge, no synthetic molecular receptor has been reported in the literature that can distinguish dopamine from glutamic acid. In this chapter, we extend our sensor design strategy from providing a secondary interaction between similar targets to study the molecular recognition events to coating a poly(lactic acid) layer on MCM-41 type mesoporous silica nanosphere (PLA-MSN) to regulate the diffusion of detecting amino-containing neurotransmitters under physiological condition.

## Materials and Methods

### Experimental Section

#### Preparation of materials

5,6-Epoxyhexyltriethoxysilane was purchased from Gelest, methanol and toluene were purchased from Fisher, and all other chemicals were purchased from Aldrich. All chemicals were used as received without further purification. Figure 4-1 illustrates schematic representation of the mesoporous silica nanosphere (MSN) materials functionalized with mercaptopropyl (Thiol-MSN) and bifunctionalized with dihydroxyhexyl/mercaptopropyl (DH-MSN).

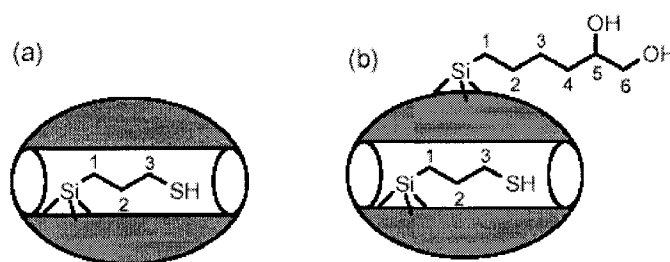


Figure 4-1. Schematic representation of a surface of MSN materials: Thiol-MSN (a) and DH-MSN (b).

#### Synthesis of DH-MSN

5,6-Epoxyhexyltriethoxysilane (EHTES, 1.0 mmol) was added to a toluene suspension (80.0 mL) of thiol-MSN (1.0 g). The reaction mixture was refluxed overnight under nitrogen. The resulting material was filtered, washed extensively with toluene and methanol and dried under vacuum for 3 h at 25 °C. The 5,6-epoxyhexyl-grafted thiol-MSN

material (1.50 g) was refluxed in a 162 mL methanol solution of hydrochloric acid (1.57 M) for 12 h to remove the CTAB template. The HCl methanol solution also converted the thiol-MSN with epoxyhexyl groups to the desired 5,6-dihydroxyhexyl-coated thiol-MSN material (DH-MSN). The surfactant-removed DH-MSN (1.00 g) was treated with 80 mL water/methanol (1/7) solution of sodium bicarbonate (0.042 g) for 4 h at room temperature to remove any unreacted, physisorbed EHTES. The purified material was dried under vacuum for 6 h at 60 °C.

#### Synthesis of PLA-coated thiol-MSN

The purified DH-MSN material (0.68 g) was sonicated for 30 min in 10.0 mL anhydrous THF to disperse the particles uniformly. *L*-Lactide (0.36 g, 2.50 mmol) was mixed with tin(II)-2-ethylhexanoate ( $\text{Sn}(\text{Oct})_2$ , 0.16 mL, 0.50 mmol), in 15 mL anhydrous THF. The lactide/catalyst solution was added to the DH-MSN THF solution by injection under  $\text{N}_2$ . The reaction mixture was stirred for 72 h under  $\text{N}_2$  at 80°C to produce the PLA-coated thiol-MSN.

#### Synthesis of OPTA-SS material

A fumed amorphous silica material (0.2 g) with a 200.0  $\text{m}^2/\text{g}$  BET surface area was added to a 20.0 mL toluene solution of 3-mercaptopropyltrimethoxysilane (0.88 mL, 4.68 mmol). The reaction mixture was refluxed over night under nitrogen. The resulting thiol-grafted solid silica was filtered and washed thoroughly with toluene, ethanol, and de-ionized water. The product was isolated by filtration and dried under vacuum for 12 h. Chemically accessible thiol density was determined by measuring the solution concentration of the side product (pyridine-2-thione) generated from the reaction of the surface thiols with 2,2'-dipyridyl disulfide in THF.<sup>1</sup> The surface-bound thiol functionality was then converted to *o*-phthalic hemithioacetal (OPTA) by reacting 85.0 mg of material with 170.0 mg (126.0 mmol) of phthalic dicarboxaldehyde (*o*-phthalaldehyde, OPA) in 10 mL methanol for 5 h. After filtration, the material was extensively washed with methanol and dried under vacuum.

## Material Characterization

Solid state NMR was used to characterize the mesoporous silica nanosphere (MSN) materials functionalized with mercaptopropyl (Thiol-MSN) and bifunctionalized with dihydroxyhexyl/mercaptopropyl (DH-MSN). The expected structures of these materials are illustrated in Figure 4-1. In addition, a PLA-coated sample (PLA-MSN) prepared from DH-MSN, was examined. The samples were also analyzed by powder X-Ray diffraction and by measurements of nitrogen adsorption/desorption isotherms (see following Sections).

## Experimental conditions

Solid-state nuclear magnetic resonance (NMR) of  $^{29}\text{Si}$  and  $^{13}\text{C}$  was used to (i) confirm the functionalization of MSN materials, (ii) determine their average molecular formulae, and (iii) provide evidence for polymerization of the lactide. The spectra were obtained at 9.4 T on a Varian/Chemagnetics Infinity spectrometer equipped with a doubly-tuned 5-mm magic angle spinning (MAS) probe. A sample rotation rate of 9 kHz was used in all experiments. The method of variable amplitude cross polarization (CP) between  $^1\text{H}$  and the observed, diluted nuclei ( $^{13}\text{C}$  or  $^{29}\text{Si}$ ) was used to increase the sensitivity.<sup>2</sup> During each CP period, the  $^1\text{H}$  rf magnetic field was ramped between 16 and 40 kHz using 2.4 kHz increments, whereas the  $^{29}\text{Si}$  (or  $^{13}\text{C}$ ) rf field was maintained at a constant level of 36 kHz. The  $^1\text{H}$  rf magnetic fields of 83 kHz and 60 kHz were used for initial excitation and during continuous wave (CW) decoupling, respectively. The measured values of  $^1\text{H}$  longitudinal relaxation time  $T_1^{\text{H}}$  did not exceed 1 s, which allowed for repetition time of 1.2 s to be used in the CPMAS experiments. In the  $^1\text{H} \rightarrow ^{13}\text{C}$  CPMAS experiments, 6,000 free induction decays (FID's) were typically acquired using two different contact times of 0.4 or 1.5 ms. The  $^1\text{H} \rightarrow ^{29}\text{Si}$  CPMAS experiments used a contact time of 1 ms and 36,000 scans. All spectra were referenced to  $\text{SiMe}_4$ . In spite of long relaxation times of  $^{29}\text{Si}$  nuclei, the direct polarization (DPMAS) method was used for quantitative measurements of various silicon groups. During these measurements a  $90^\circ$  excitation pulse of 2.1  $\mu\text{s}$  was followed by acquisition of the  $^{29}\text{Si}$  FID under CW  $^1\text{H}$  decoupling at 65 kHz. The saturation recovery experiment, carried out with MCM-41 samples functionalized with allyl and 3-isocyanatopropyl groups, yielded the values of  $T_1^{\text{Si}}$  on the order of 50 to 65 s for  $\text{T}^{\text{n}}$  groups and 30 to 45 s for  $\text{Q}^{\text{n}}$  groups.<sup>3</sup> Thus, a



delay of 300 s between the scans was used to allow for full restoration of the equilibrium magnetization of  $^{29}\text{Si}$  spins. An acquisition of 270 FID's yielded the relative intensities of  $^{29}\text{Si}$  resonances with an accuracy of  $\pm 3\%$ .

#### Powder X-Ray Diffraction

Powder XRD experiments were performed on a Scintag XDS 2000 diffractometer using a Cu K $\alpha$  radiation source. Low angle diffraction with a  $2\theta$  range of 1 to  $10^\circ$  was used to investigate the long-range order of the materials.

#### Nitrogen adsorption/desorption isotherms

The surface area and median pore diameter were measured using  $\text{N}_2$  adsorption/desorption measurements in a Micromeritics ASAP 2000 BET surface analyzer system. The data were evaluated using the Brunauer-Emmett-Teller (BET) and Barrett-Joyner-Halenda (BJH) methods to calculate the surface area and pore volumes/pore size distributions, respectively. Samples were prepared by degassing at  $90^\circ\text{C}$  for 1 h and then at  $150^\circ\text{C}$  for 4 h.

#### Particle size distribution and scanning electron micrograph of PLA-MSN

Particle morphology of these materials was determined by scanning electron microscopy (SEM) using a Hitachi S4700 FE-SEM system with 10 kV accelerating voltage and 0.005 nA of beam current for imaging.

#### Transmission electron micrograph of PLA-MSN

For transmission electron microscopy (TEM) studies, a small aliquot was taken from a suspension of methanol and placed in a lacey carbon-coated TEM grid, which was pulled through the suspension and allowed to dry in air. Thin sections of samples embedded in epoxy resin were obtained with ultramicrotomy (60-80 nm). The resulting sample was examined with a Philips model CM-30 TEM operated at 300 kV. The specimen was given no further treatment, as it appeared stable under beam bombardment.

HPLC analysis of the competitive detection of PLA-MSN system in a mixture of dopamine and glutamic acid

PLA-MSN nanoparticles (2 mg) were introduced to a pH 7.4 PBS buffer (10 mM) solution of dopamine (0.5 mM) and glutamic acid (10 mM) at 25°C. After 10 min of mixing, the suspension was centrifuged and the individual concentrations of dopamine and glutamic acid in the supernatant were analyzed by HPLC. All analyses were performed on a Hitachi LC/3DQMS HPLC system with a reverse phase C18 column (SUPELCOSIL LC-18-T 250 mm × 4.6 mm, ID 5µm packing, Aldrich). The UV absorption peak at 210 nm was used for the quantitative analyses of Glutamic acid and Dopamine. Flow rate of mobile phase was 1 mL/min. The mobile phase eluent consisted of a mixture of 0.1M potassium dihydrogen phosphate adjusted to pH 6.0 (solvent A) and methanol (solvent B). The elution gradient program was as follows: 0 min 100% A, 0% B, 9min 100%A, 0%B; 11min, 70%A, 30% B; 17 min 70% A, 30% B; 18 min 100% A, 0% B. Finally, an additional 7 min was allowed for the column to return to the initial condition and re-equilibrate. The column temperature was set at room temperature and the injection volume of samples was 25 µL for all analyses.

## Results and Discussion

We synthesized a mercaptopropyl-functionalized mesoporous silica nanosphere (thiol-MSN) material with average pore diameter of 2.5 nm via our previously reported method.<sup>3a,4</sup> As outlined in Figure 4-2, 5,6-epoxyhexyltriethoxysilane (EHTES) was grafted onto the exterior surface of the thiol-MSN-containing cetyltrimethylammonium bromide (CTAB) surfactants inside the mesopores.

The resulting material was refluxed in a methanol solution of hydrochloric acid to remove the CTAB template and to convert the thiol-MSN with epoxyhexyl groups to a 5,6-dihydroxyhexyl-coated thiol-MSN material (DH-MSN).<sup>5</sup> Incorporation of the 5,6-dihydroxyhexyl group was confirmed by <sup>29</sup>Si and <sup>13</sup>C CP- and DP-MAS NMR spectroscopy (see below) and the surface coverage was measured to be 43% (2.1 mmol/g).

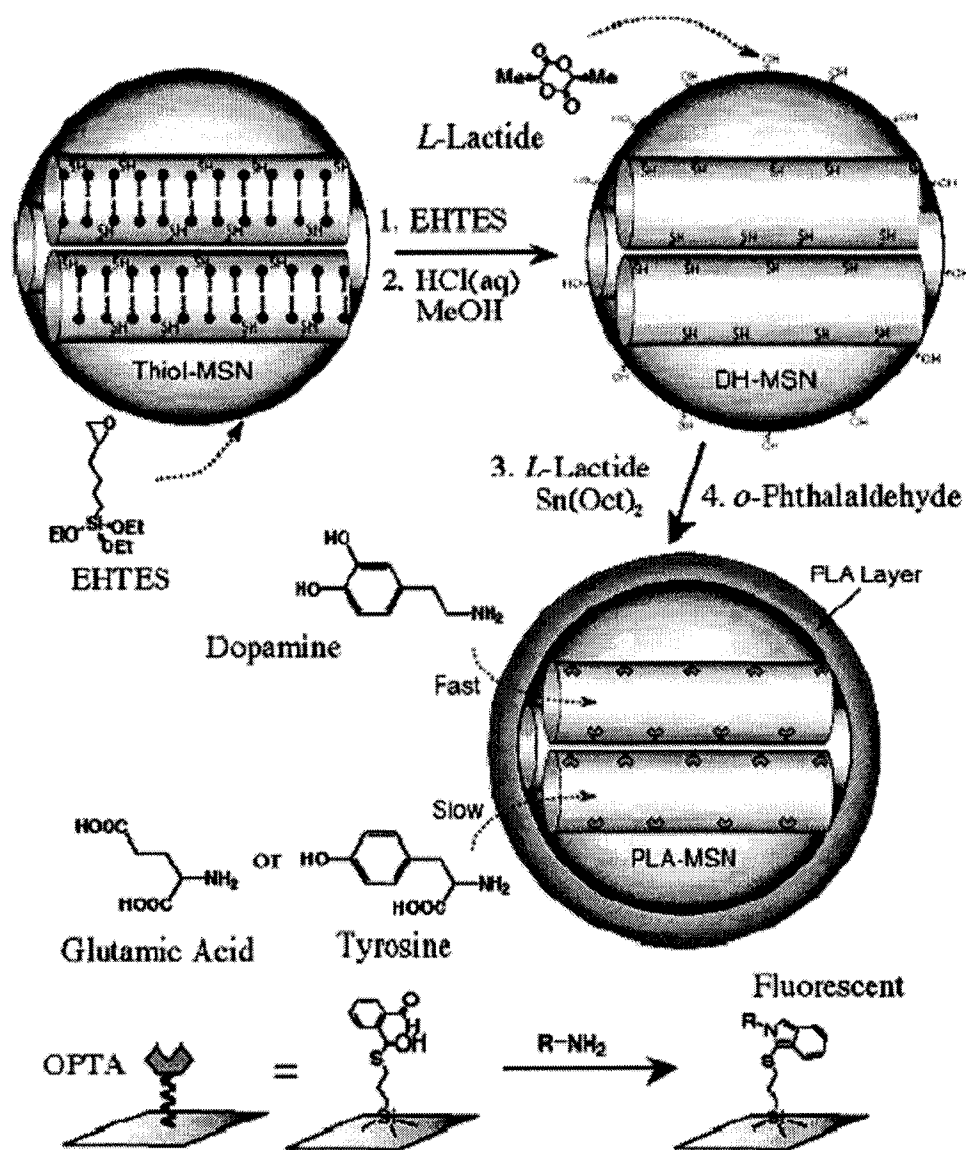


Figure 4-2. Schematic representation of the synthesis of PLA-coated MSNbased fluorescence sensor system for detection of amine-containing neurotransmitters, i.e., dopamine, glutamic acid, and tyrosine (R-NH<sub>2</sub>). (5,6-epoxyhexyltriethoxysilane ) EHTES, cetyltrimethylammonium bromide(CTAB) surfactant = ●~~~~.

Figure 4-3 shows the <sup>13</sup>C and <sup>29</sup>Si spectra acquired for Thiol-MSN, DH-MSN and PLA-MSN samples. The carbon chemical shifts  $\delta_C$  corresponding to thiol, DH, and PLA functional groups are listed in Table 4-1, while Table 4-2 includes the chemical shifts  $\delta_{Si}$  of T<sup>n</sup> and Q<sup>n</sup> silicone groups. In addition, Table 4-2 shows the relative concentrations of silicon groups, molecular formulae, and molar concentrations of organic functionalities obtained



Table 4-2. Summary of  $^{29}\text{Si}$  CPMAS NMR DATA

	Relative concentration of silicon groups [%]					SC [%] <sup>(a)</sup>	Average molecular formula
	T <sup>2</sup> (-58ppm)	T <sup>3</sup> (-67ppm)	Q <sup>2</sup> (-93ppm)	Q <sup>3</sup> (-102ppm)	Q <sup>4</sup> (-112ppm)		
Thiol-MSN	4	15	3	29	49	37 (2.7)	(SiO <sub>2</sub> ) <sub>100</sub> (H <sub>2</sub> O) <sub>10</sub> (C <sub>3</sub> H <sub>8</sub> S) <sub>19</sub>
DH-MSN	3	16	1	24	56	43 (2.1)	(SiO <sub>2</sub> ) <sub>100</sub> (H <sub>2</sub> O) <sub>5</sub> (C <sub>3</sub> H <sub>8</sub> S+C <sub>6</sub> H <sub>14</sub> O <sub>2</sub> ) <sub>9</sub>
PLA-MSN	3	16	1	24	56	43	

(a) SC - surface coverage calculated using following equation:  $SC = (T^2 + T^3)/(T^2 + T^3 + Q^2 + Q^3)$ . Note that NMR data represent the SC's of the entire surface. According to our N<sub>2</sub> adsorption measurements, the external surface area in the studied MSN's was approximately 30%. Thus, the surface coverage of internal pores in Thiol-MSN is in fact 40% higher. The values in parentheses represent the amounts of organic groups in mmol/g.

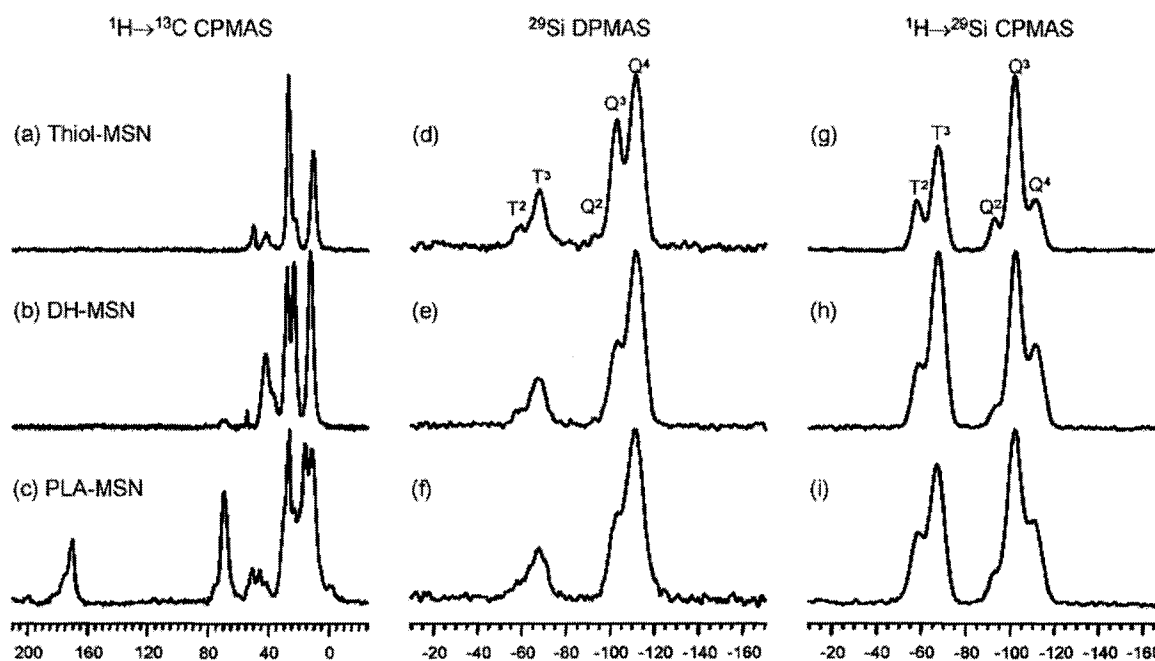


Figure 4-3.  $^1\text{H} \rightarrow ^{13}\text{C}$  CPMAS (a-c),  $^{29}\text{Si}$  DPMAS (d-f) and  $^1\text{H} \rightarrow ^{29}\text{Si}$  CPMAS (g-i) spectra collected for Thiol-MSN (a,d,g), DH-MSN (b,e,h) and PLA-MSN (c,f,i) samples. Following contact times (in ms) were used to collect the CPMAS spectra: 0.4 (a,b), 1.5 (c), and 1.0 (g-i).

The assignments of  $^{29}\text{Si}$  NMR, which are also shown in Figure 4-3, spectra (d) and (g), are well established in the literature.<sup>3,4,8,13</sup> The following silicone groups were found: T<sup>2</sup> (at -58 ppm), T<sup>3</sup> (-67 ppm), Q<sup>2</sup> (-93 ppm), Q<sup>3</sup> (-102 ppm), and Q<sup>4</sup> (-112 ppm). Surface coverage (SC), calculated using equation:  $SC = (T^2 + T^3)/(T^2 + T^3 + Q^2 + Q^3)$ , expresses amount of surface silicone atoms bonded to an organic group per total number of surface silicone atoms. Note that the  $^{29}\text{Si}$  CPMAS spectra are not quantitative; they were merely used to facilitate the deconvolution of less intense resonances measured using DPMAS NMR.

The vacuum-dried DH-MSN material (0.68 g) was sonicated for 30 min in 10 mL of anhydrous THF to disperse the particles uniformly. L-Lactide (0.36 g, 2.50 mmol) was mixed with a catalyst, tin(II) 2-ethylhexanoate ( $\text{Sn}(\text{Oct})_2$ , 0.16 mL, 0.50 mmol), in 15 mL of anhydrous THF. The lactide/catalyst solution was added to the DH-MSN THF suspension via injection and stirred at 80 °C for 72 h to yield the PLA-coated thiol-MSN material. The crude solid product was further purified by a method previously published by Langer's group.<sup>7</sup> As shown in Figure 4-4, the average thickness (ca. 11 nm) of the PLA layer was determined by transmission electron microscopy (TEM). The chemically accessible thiol density (0.22 mmol/g) of the purified PLA-MSN was measured by our previously published method.<sup>3a</sup>

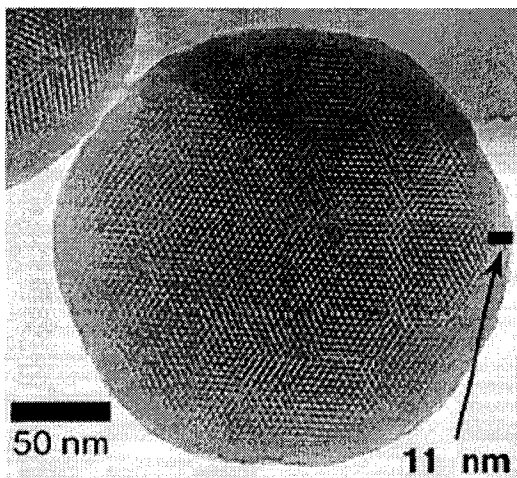


Figure 4-4. Transmission electron micrograph (TEM) of an ultramicrotomed PLA-MSN material. The layer of PLA can be visualized by the rim of amorphous structure surrounding the MCM-41-type of MSN core with mesopores packed in a hexagonal symmetry.

The mercaptopropyl functionality was then converted to the amine-sensitive OPTA group by reacting 85.0 mg of PLA-coated thiol-MSN with 170.0 mg (1.26 mmol) of phthalic dicarboxaldehyde (*o*-phthalaldehyde, OPA) in 10 mL of methanol solution for 5 h. After filtration, the resulting material (PLA-MSN) was thoroughly washed with methanol and dried under vacuum. The morphology, particle size distribution, and the structure of organic

functionalities of PLA-MSN were scrutinized by XRD, SEM, TEM, N<sub>2</sub> sorption isotherms (From Figure 4-5 to 4-7 and Table 4-3).

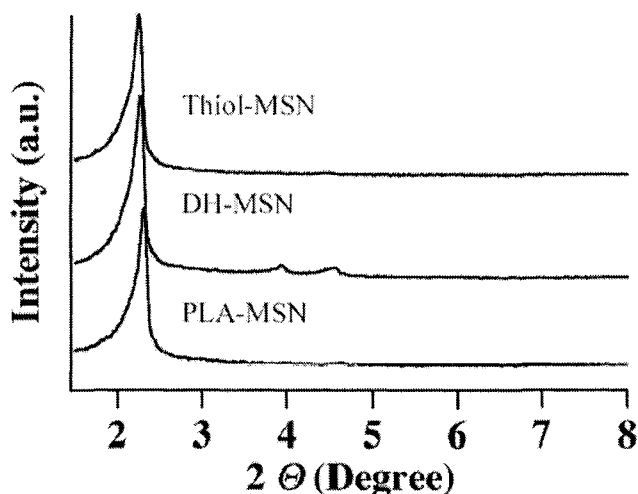


Figure 4-5. Powder X-Ray diffraction patterns of thiol-MSN, DH-MSN, and PLA-MSN. All three materials exhibit the typical diffraction patterns of MCM-41 type mesoporous silica with hexagonal symmetry.

Table 4-3. Powder X-Ray diffraction results

Sample	Powder XRD Diffraction		
	$d_{100}$ (Å)	$d_{200}$ (Å)	$d_{111}$ (Å)
Thiol-MSN	20.26	11.50	10.00
DH-MSN	23.30	11.84	9.74
PLA-MSN	22.64	11.50	9.63

The N<sub>2</sub> sorption isotherms of thiol-MSN material were published in our previous papers.<sup>9</sup> The details of nitrogen sorption analyses of the DH-MSN and PLA-MSN materials are outlined below (Table 4-4).

Table 4-4. Nitrogen sorption isotherms.

Material	BET	BET	BJH
	Surface Area (m <sup>2</sup> /g)	Pore volume (mL/g)	Average Pore Diameter (Å)
DH-MSN	904.38	0.53	23.0
PLA-MSN	633.95	0.34	20.5

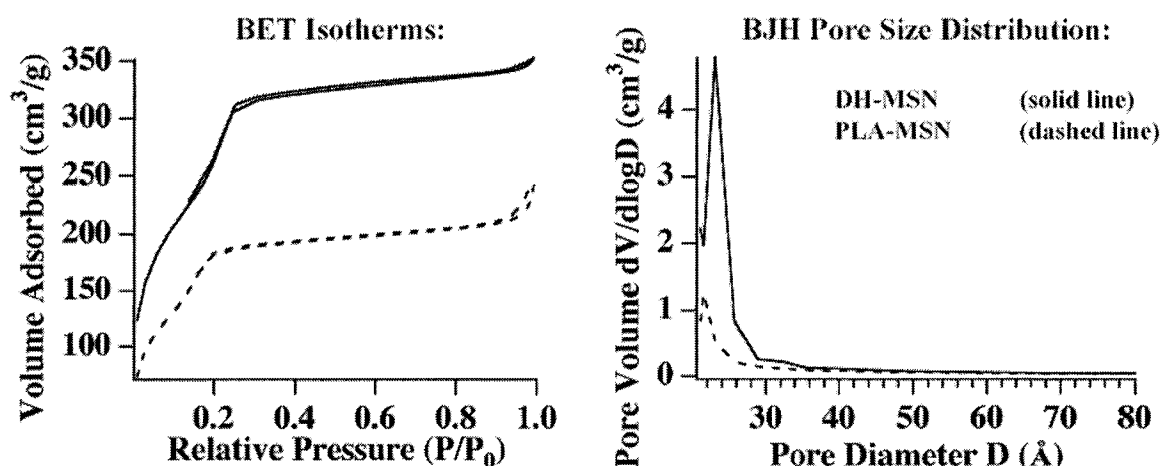


Figure 4-6. BET nitrogen adsorption/desorption isotherms and BJH pore size distributions of DH-MSN (solid line) and PLA-MSN (dashed line) materials. The BET isotherms of both DH-MSN and PLA-MSN materials didn't exhibit any hysteresis, which suggested the absence of the xerogel layer.

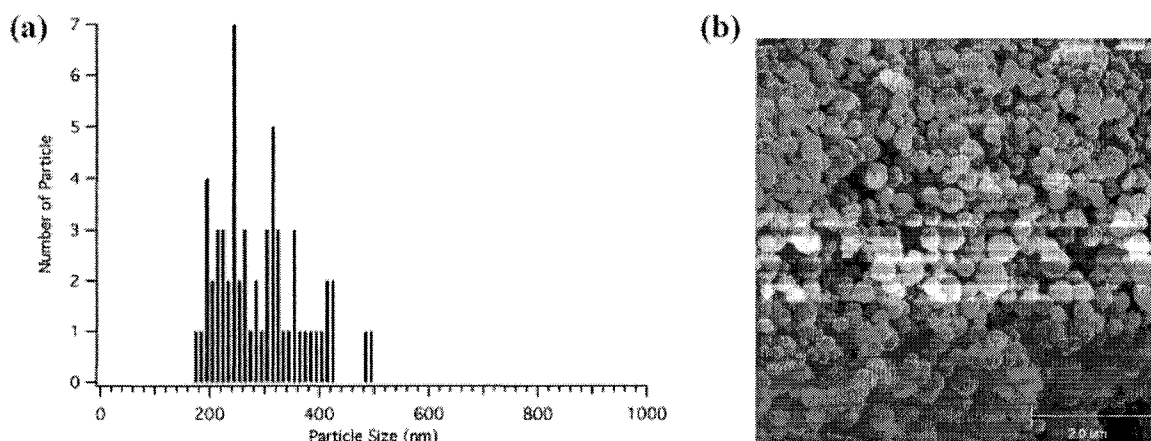


Figure 4-7. Particle size distribution (a) and scanning electron micrograph (b) of PLA-MSN. Polydispersity of PLA-MSN is *approx.* 160 nm (half width at half maximum of the particle size distribution).

To examine the gatekeeping effect of the PLA layer in our PLA-MSN system, we prepared and characterized an amorphous silica material grafted with the same OPTA functionality (OPTA-SS) as a control system.<sup>6</sup> The surface coverage of the OPTA group was determined to be 0.08 mmol/g.<sup>2a,4</sup> Both the OPTA-SS and our PLA-MSN materials were dispersed in pH 7.4 PBS buffer (10 mM) for the fluorescence-sensing experiments of neurotransmitters. In the case of OPTA-SS, dopamine, tyrosine, and glutamic acid (230  $\mu$ M each) reacted with the surface-bound OPTA groups rapidly, as evidence by the fluorescence



emission data shown in Figure 4-8a. It is noteworthy that both tyrosine and glutamic acid reacted to the OPTA-SS with very similar rates and therefore could not be distinguished. In contrast, the reactions of these analytes (230  $\mu\text{M}$ ) with our OPTA-derivatized PLA-MSN exhibited significantly different and lower reaction rates (Figure 4-8b), by a factor of 4, 10, and 57, respectively. In the case of dopamine, the lower reaction rate could be attributed to the additional diffusional penetration through the PLA layer into the OPTA-functionalized mesopores. Clearly, the reaction rates of tyrosine and glutamic acid were further slowed by the gatekeeping effect of the PLA layer on these two analytes. In addition, our study (Figure 4-8c) showed that the fluorescence intensity of OPTA-SS increased similarly with the increasing concentrations of all three neurotransmitters. However, in the case of the PLA-MSN (Figure 4-8d), the dopamine binding gave the most significant increase of fluorescence intensities at all concentrations. We also note that a similar set of kinetic and titration experiments performed on the DH-MSN material (without PLA) showed no evidence of the gatekeeping effect.<sup>6</sup> To examine the substrate selectivity of our PLA-MSN system in the presence of a mixture of neurotransmitters, PLA-MSN nanoparticles (2 mg) were introduced to a pH 7.4 PBS buffer (10 mM) solution of dopamine (0.5 mM) and glutamic acid (10 mM) at 25 °C.

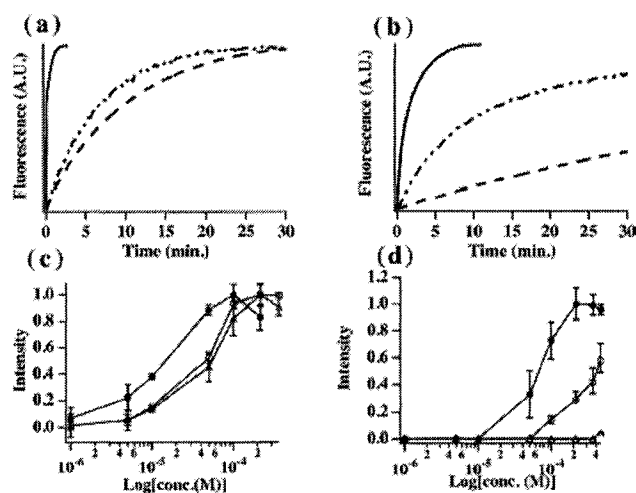


Figure 4-8. Kinetic measurements of the fluorescence detection of dopamine (s), tyrosine (- - - - -), and glutamic acid (- - -) with OPTA-SS (a) and PLA-MSN (b). Fluorescence increase of OPTA-SS (c) and PLAMSN (d) as a function of dopamine (b), tyrosine (O), and glutamic acid (4) concentrations. The fluorescence intensities were measured 5 min after the introduction of every concentration of each neurotransmitter.

After 10 min of mixing, the suspension was centrifuged, and the individual concentrations of dopamine and glutamic acid in the supernatant were analyzed by HPLC (Figure 4-9).<sup>6</sup>

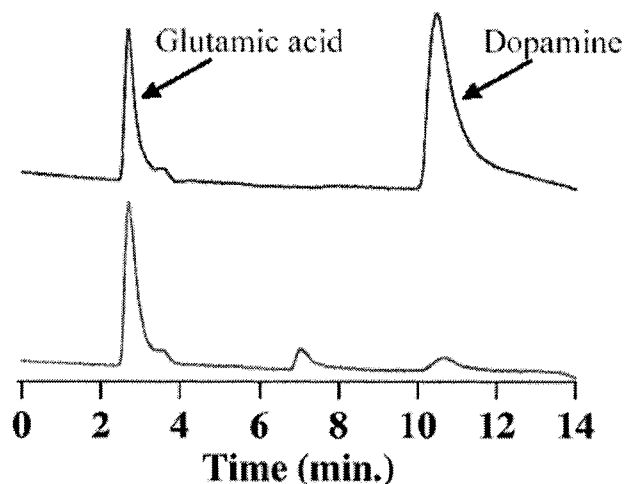


Figure 4-9. HPLC chromatographs of the solution containing dopamine (0.5 mM) and glutamic acid (10 mM) before (blue) and after (red) the introduction of PLA-MSN.

Given that the signal transduction mechanism of the PLA-MSN system is based on the covalent capture of substrates by the surface-bound OPTA groups, the different degrees of concentration decrease of these two analytes in solution would represent the selectivity of the PLA-MSN system. Despite the initial 20:1 concentration ratio between glutamic acid and dopamine, the results showed a 96% decrease of dopamine concentration, whereas only a 2% decrease of the concentration of glutamic acid was observed (Table 4-5).<sup>6</sup>

Table 4-5. HPLC analysis of dopamine and glutamic acid before and after the introduction of PLA-MSN.

	Dopamine		Glutamic acid	
	Integrated Peak Area	Retention time (min)	Integrated Peak Area	Retention time (min)
Before introduction of PLA-MSN	403270	10.54	140508	2.67
After 10 min of mixing with PLA-MSN	16499	10.72	138267	2.67

The observed large difference in the rates of diffusion is most likely due to the different electrostatic, hydrogen bonding, and dipolar interactions between these neurotransmitters and the PLA layer in pH 7.4 buffer solutions. The isoelectric points (pIs) of dopamine, tyrosine, and glutamic acid are 9.7, 5.7, and 3.2, respectively, whereas the pI of PLA is typically below 2.0,<sup>8</sup> which means the dopamine will be positively charged and the others will be negatively charged under our experimental conditions. Similar effects of pI have also been reported previously.<sup>9</sup> For example, Blanco et. al reported that proteins with low pI values, such as bovine serum albumin (pI = 4.6) were released faster from a PLGA-based polymer than those with high pIs, such as lysozyme (pI = 11.2).<sup>9a</sup>

### Conclusions

We report on the synthesis and characterization of a poly-(lactic acid)-coated, MCM-41-type mesoporous silica nanosphere (PLA-MSN) material as a fluorescence probe. By utilizing the PLA layer as a *gatekeeper* to regulate the penetration of molecules in and out of the nanoscale pores, we successfully select the molecular recognition events between several structurally simple neurotransmitters, i.e., dopamine, tyrosine, and glutamic acid and a pore surface-anchored *o*-phthalic hemithioacetal (OPTA) group

### Acknowledgements

This research was supported at Ames Laboratory by the U.S. DOE, office of BES, under contract W-7405-Eng-82 and by the NSF (CHE-0239570).

### References

1. Sawa, A.; Snyder, S. H. *Science (Washington, DC)* **2002**, *296*, 692 and references therein.
2. (a) Stucky, G. D.; Zhao, D.; Yang, P.; Lukens, W.; Melosh, N.; Chmelka, B. F. *Stud. Surf. Sci. Catal.* **1998**, *117*, 1. (b) Dai, S.; Burleigh, M. C.; Shin, Y.; Morrow, C. C.;

- Barnes, C. E.; Xue, Z. *Angew. Chem., Int. Ed.* **1999**, *38*, 1235. (c) Stein, A.; Melde, B. J.; Schroden, R. C. *Adv. Mater. (Weinheim, Ger.)* **2000**, *12*, 1403.
3. (a) Lin, V. S.-Y.; Lai, C.-Y.; Huang, J.; Song, S.-A.; Xu, S. *J. Am. Chem. Soc.* **2001**, *123*, 11510. (b) Simons, S. S., Jr.; Johnson, D. F. *Anal. Biochem.* **1978**, *90*, 705.
  4. (4) Lai, C.-Y.; Trewyn, B. G.; Jeftinija, D. M.; Jeftinija, K.; Xu, S.; Jeftinija, S.; Lin, V. S.-Y. *J. Am. Chem. Soc.* **2003**, *125*, 4451.
  5. (a) Jogikalmath, G.; Stuart, J. K.; Pungor, A.; Hlady, V. *Colloids Surf. A* **1999**, *154*, 53-64. (b) Park, Y.-I.; Nagai, M. *Solid State Ionics* **2001**, *145*, 149.
  6. See the experimental details on materials preparation, N<sub>2</sub> adsorption isotherms, particle size distributions, SEM micrograph, XRD spectra, HPLC analysis of the competitive neurotransmitter detection of PLA-MSN, kinetic and titration measurements of DHMSN, as well as detailed analysis of solid state <sup>13</sup>C and <sup>29</sup>Si NMR experiments.
  7. Choi, I. S.; Langer, R. *Macromolecules* **2001**, *34*, 5361.
  8. Gomez-Lopera, S. A.; Plaza, R. C.; Delgado, A. V. *J. Colloid Interface Sci.* **2001**, *240*, 40.
  9. (a) Blanco, D.; Alonso, M. J. *Eur. J. Pharm. Biopharm.* **1998**, *45*, 285. (b) Dalmia, A.; Liu, C. C.; Savinell, R. F. *J. Electroanal. Chem.* **1997**, *430*, 205. (c) O'Brien, K. B.; Esguerra, M.; Klug, C. T.; Miller, R. F.; Bowser, M. T. *Electrophoresis* **2003**, *24*, 1227.
  10. Mora, F.; del Arco, A.; Segovia, G. *J. Physiol. Biochem.* **2001**, *57*, 97.
  11. (a) Yee, J. K.; Parry, D. B.; Caldwell, K. D.; Harris, J. M. *Langmuir* **1991**, *7*, 307. (b) Millot, M. C.; Sebille, B.; Mahieu, J. P. *J. Chromatogr.* **1986**, *354*, 155.
  12. (a) Yee, J. K.; Parry, D. B.; Caldwell, K. D.; Harris, J. M. *Langmuir* **1991**, *7*, 307. (b) Millot, M. C.; Sebille, B.; Mahieu, J. P. *J. Chromatogr.* **1986**, *354*, 155.
  13. (a) Pines, A.; Gibby, M. G.; Waugh, J. S. *J. Chem. Phys.* **1973**, *59*, 569. (b) Peersen, O. B.; Wu, X.; Kustanovich, I.; Smith, S. O. *J. Magn. Reson. A* **1993**, *104*, 334.
  14. Huh, S.; Wiench, J. W.; Yoo, J.-C.; Pruski, M.; Lin, V. S. Y. *Chem. Mater.* **2003**, *15*, 4247.
  15. Maciel, G. E.; Sindorf, D. W.; Bartuska, V. J. *J. Chromatogr.* **1981**, *205*, 438.

16. Freeman, F.; Angeletakis, C. N. *J. Org. Chem.* **1982**, *47*, 4194.
17. Grant, D. M.; Paul, E. G. *J. Am. Chem. Soc.* **1964**, *86*, 2984.

Chapter 5. A Mesoporous Silica Nanosphere-Based Carrier System with Chemically Removable CdS Nanoparticle Caps for Stimuli-Responsive Controlled Release of Neurotransmitters and Drug Molecules

The paper was published in *The Journal of American Chemical Society*

*J. Am. Chem. Soc.* **2003**; *125* (15), 4451- 4459,

Lai, C.-Y.; Trewyn, B. G.; Jeftinija, D. M.; Jeftinija, K.; Xu, S.; Jeftinija, S.; Lin, V. S.-Y.

Department of Chemistry and Department of Biomedical Science, Iowa State University,

Ames, Iowa 50011-3111

Abstract

An MCM-41 type mesoporous silica nanosphere-based (MSN) controlled-release delivery system has been synthesized and characterized using surface-derivatized cadmium sulfide (CdS) nanocrystals as chemically removable caps to encapsulate several pharmaceutical drug molecules and neurotransmitters inside the organically functionalized MSN mesoporous framework. We studied the stimuli-responsive release profiles of vancomycin- and adenosine triphosphate (ATP)-loaded MSN delivery systems by using disulfide bond-reducing molecules, such as dithiothreitol (DTT) and mercaptoethanol (ME), as *release triggers*. The biocompatibility and delivery efficiency of the MSN system with neuroglial cells (astrocytes) *in vitro* were demonstrated. In contrast to many current delivery systems, the molecules of interest were encapsulated inside the porous framework of the MSN not by adsorption or sol-gel types of entrapment but by capping the openings of the mesoporous channels with size-defined CdS nanoparticles to physically block the drugs/neurotransmitters of certain sizes from leaching out. We envision that this new MSN system could play a significant role in developing new generations of site-selective, controlled-release delivery nanodevices.

## Introduction

Several attractive features, such as stable mesoporous structures, large surface areas, tunable pore sizes and volumes, and well-defined surface properties of the organically functionalized MCM-type mesoporous silica materials<sup>1</sup> have made them ideal for hosting molecules of various sizes, shapes, and functionalities. Therefore, developing new mesoporous silica-based carrier systems for controlled-release delivery of drugs,<sup>2</sup> biocides, genes, or even proteins<sup>3</sup> in vitro or in vivo is of keen interest.

Many important site-selective deliveries, e.g., deliveries of highly toxic antitumor drugs, such as Taxol, require "zero release" before reaching the targeted cells or tissues. However, the release of encapsulated compounds of many current drug delivery systems typically takes place immediately upon dispersion of the drug/carrier composites in water.<sup>4</sup> Also, the release mechanism of many biodegradable polymer-based drug delivery systems relies on the hydrolysis-induced erosion of the carrier structure.<sup>5</sup> Such systems typically require the use of organic solvents<sup>6</sup> for drug loading, which could sometimes trigger undesirable modifications of the structure or function or both of the encapsulated molecules, such as protein denaturation and aggregation. Herein, we report the synthesis of a novel MCM-41 type mesoporous silica-based controlled-release delivery system that is stimuli-responsive and chemically inert to the matrix-entrapped compounds. The system consists of a 2-(propylthiol)ethylamine functionalized mesoporous silica nanosphere (MSN) material with an average particle size of 200.0 nm and an average pore diameter of 2.3 nm. As depicted in Figure 5-1, the mesopores of the MSN material were used as reservoirs to soak up aqueous solutions of various pharmaceutical drug molecules and neurotransmitters, such as vancomycin and adenosine triphosphate (ATP). The openings of the mesopores of the drug/neurotransmitter-loaded MSN material were then capped in situ by allowing the pore surface-bound 2-(propylthiol)ethylamine functional groups to covalently capture the water-soluble mercaptoacetic acid-derivatized cadmium sulfide (CdS) nanocrystals<sup>7</sup> via a literature-reported amidation reaction.<sup>8</sup> The resulting disulfide linkages between the MSNs and the CdS nanoparticles are *chemically labile* in nature and can be cleaved with various disulfide-reducing agents, such as dithiothreitol (DTT) and mercaptoethanol (ME).

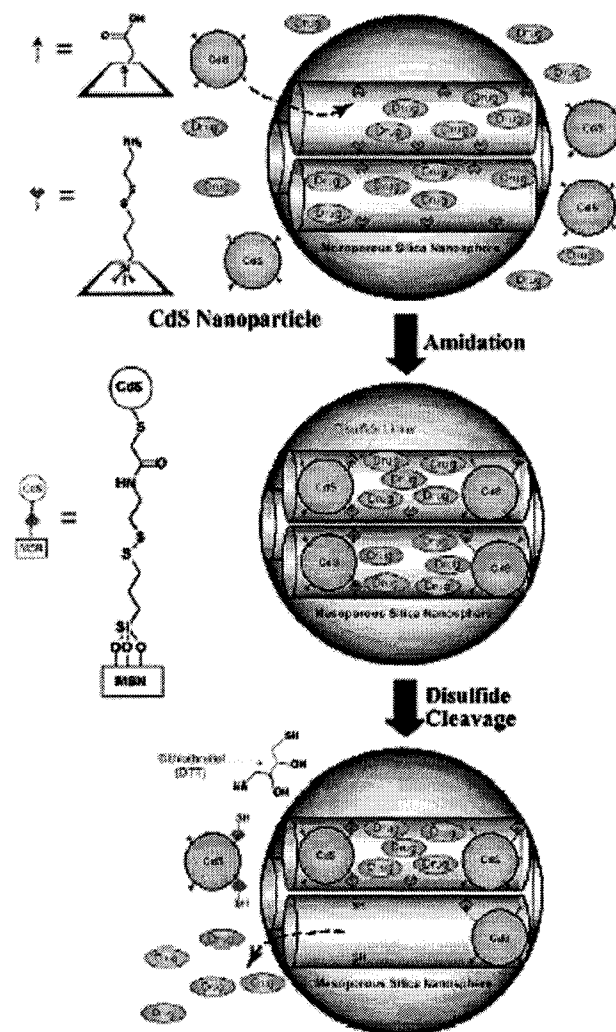


Figure 5-1 Schematic representation of the CdS nanoparticle-capped MSN-based drug/neurotransmitter delivery system. The controlled-release mechanism of the system is based on chemical reduction of the disulfide linkage between the CdS caps and the MSN hosts.

Hence, the release of the CdS nanoparticle caps from the drug/neurotransmitter-loaded MSNs can be regulated by introducing various amounts of *release triggers*. In this study, we investigated the stimuli-responsive release profiles, the biocompatibility with neuroglial cells (astrocytes) *in vitro*, and the delivery efficiency of vancomycin and adenosine triphosphate (ATP) encapsulated inside the CdS-capped MSN system.



## Materials and Methods

### Experimental Section

**Materials.** Cadmium nitrate tetrahydrate (99.99%), sodium sulfide, mercaptoacetic acid, 3-mercaptopropyltrimethoxysilane (MPTMS), *n*-cetyltrimethylammonium bromide (CTAB), tetraethyl orthosilicate (TEOS), 2-aminoethanethiol hydrochloride, 1-[3-(dimethylamino)propyl]-3-ethylcarbodiimide hydrochloride (EDC), dithiothreitol (DTT), and aldrithiol-2 were purchased (Aldrich) and used as received. Vancomycin hydrochloride and adenosine triphosphate disodium salt (ATP) were obtained from Sigma and used without further purification. Nanopure water (18.1 MHz) prepared from a Barnstead E-pure water purification system was employed throughout. PBS buffer (10.00 mM, pH 7.4) solutions with the total ionic strength of 0.06 M were prepared and used as the solvent for all the loading and release experiments of vancomycin and ATP.

### CdS Nanoparticle Preparation

**Synthesis of Mercaptoacetic Acid-Derivatized Cadmium Sulfide (CdS) Nanoparticles.** The synthetic procedures were modified from the previous literature report by Alivisatos and co-workers.<sup>7</sup> Mercaptoacetic acid ( $2.15 \times 10^{-3}$  mol, 150.00  $\mu$ L) was added to an aqueous solution (270.00 mL) of cadmium nitrate tetrahydrate ( $3.00 \times 10^{-4}$  mol), forming a turbid blue solution, followed by adjusting the solution pH to 11 with 0.01 M NaOH. Sodium sulfide ( $1.50 \times 10^{-4}$  mol) was dissolved in 10.0 mL of H<sub>2</sub>O and rapidly added to the cadmium nitrate solution with vigorous stirring. The reaction mixture was protected from light and stirred for 10 min. It was concentrated to about one-tenth of its original volume using a rotary evaporator, and anhydrous methanol was added until the precipitate formed, yielding the mercaptoacetic acid-capped, water-soluble cadmium sulfide nanoparticles (CdS).

**Synthesis of MCM-41-Type Mesoporous Silica Nanosphere with 2-(Propyldisulfanyl)ethylamine Functionality (Linker-MSN)**

The MSN material was synthesized by derivatization of a mercaptopropyl-functionalized mesoporous silica nanosphere material (thiol-MSN) prepared by the following procedures: *n*-Cetyltrimethylammonium bromide (CTAB, 1.00 g,  $2.74 \times 10^{-3}$  mol) was first dissolved in 480 mL of Nanopure water. NaOH(aq) (2.00 M, 3.50 mL) was added to CTAB solution, followed by adjusting the solution temperature to 353 K. TEOS (5.00 mL,  $2.57 \times 10^{-2}$  mol) was first introduced dropwise to the surfactant solution, followed by the dropwise addition of MPTMS (0.97 mL,  $5.13 \times 10^{-3}$  mol). The mixture was allowed to stir for 2 h to give rise to white precipitates (as synthesized thiol-Sphere). The solid product was filtered, washed with deionized water and methanol, and dried in air. To remove the surfactant template (CTAB), 1.50 g of as-synthesized thiol-Sphere was refluxed for 24 h in a solution of 9.00 mL of HCl (37.4%) and 160.00 mL of methanol followed by extensive washes with deionized water and methanol. The resulting surfactant-removed thiol-MSN material was placed under high vacuum to remove the remaining solvent in the mesopores. The chemically accessible thiol group surface coverage of the thiol-MSN material was quantified to be  $7.64 \times 10^{-4}$  mol/g by our previously published method.<sup>9a</sup> The purified thiol-MSN material (1.00 g) was treated with a methanol solution (60.00 mL) of 2-(pyridyldisulfanyl)ethylamine (PDEA) ( $9.12 \times 10^{-4}$  mol), which was synthesized via a literature procedure,<sup>10</sup> at room temperature for 24 h under vigorous stirring to undergo the desired disulfide bond exchange reaction. The resulting MSN material with 2-(propyldisulfanyl)ethylamine functionality was filtered and washed with methanol and dried in air.

#### Loading of Vancomycin and ATP into the Mesoporous Framework of Linker-MSN and the Capping of the Mesopores with Mercaptoacetic Acid-Functionalized CdS Nanoparticles

The purified linker-MSN material (100.00 mg) was incubated in the aforementioned PBS buffer solution (0.60 mL, pH 7.4) of ATP or vancomycin (3.00  $\mu$ mol in both cases) for 24 h. The mercaptoacetic acid-functionalized CdS nanoparticles (0.15 mmol) were dissolved in 2.00 mL of PBS buffer with vancomycin or ATP (0.01 mmol in both cases). 1-[3-(Dimethylamino)propyl]-3-ethylcarbodiimide hydrochloride (EDC) (57.50 mg, 0.30 mmol) was added to the CdS/drug solution. The reaction mixture was allowed to stir for 24 h,

followed by centrifuging the suspension at 12 000 rpm for 3 min. The resulting precipitates (ATP- or vancomycin-loaded, CdS-capped MSNs) were isolated and dried under vacuum.

#### DTT-Induced Drug/Neurotransmitter Release Study

CdS-capped MSN with vancomycin or ATP (10.00 mg) material was dispersed in 1.50 mL of PBS buffer (pH 7.4), followed by repeating wash/sonication/centrifugation cycles for five times to remove physisorbed, uncapped vancomycin or ATP molecules on the exterior surface of the material. The purified MSN/drug composite was redispersed in 3.50 mL of PBS buffer (pH 7.4). Aliquots were taken every 4 h over a time period of 12 h from the MSN/water suspension and injected to an analytical HPLC system (Hitachi LC/3DQMS with a reverse phase C18 column (Vydac), 0.4 cm × 25 cm) to monitor the leaching of the mesoporous channel encapsulated vancomycin or ATP molecules. After 12 h, dithiothreitol (DTT, 18.50 mM) was added to the suspension to cleave the disulfide linkage between the CdS nanoparticle and the MSN. The kinetic profiles of the DTT-induced release of vancomycin and ATP were monitored by following two literature-reported HPLC separation conditions.<sup>20</sup> The peaks/areas at 280 and 258 nm were monitored/integrated for the quantitative analysis of amounts of released vancomycin and ATP, respectively.

#### Instrumental Methods, Conditions, and Parameters for the Structure Characterizations of Linker-MSN and CdS-Capped MSN Materials

Powder XRD diffraction data were collected on a Scintag XRD 2000 X-ray diffractometer using Cu K $\alpha$  radiation. Nitrogen adsorption and desorption isotherm, surface area (SA), and median pore diameter (MPD) were measured using a Micromeritics ASAP2000 sorptometer. Sample preparation included degassing at 130 °C for 1 h. Nitrogen adsorption and desorption isotherms of these materials were obtained at -196 °C. Specific surface areas and pore size distributions were calculated using the Brunauer-Emmett-Teller (BET) and Barrett-Joyner-Halenda (BJH) method, respectively. Particle morphology of these materials was determined by scanning electron microscopy (SEM) using a JEOL 840A scanning electron microscope with 10 kV accelerating voltage and 0.005 nA of beam current for imaging. For transmission electron microscopy (TEM) studies, a small aliquot was

removed and placed between two clean glass slides. Slides were squeezed between fingers and rubbed back and forth to break up larger clumps. The resulting powder was washed into a Petri dish with acetone. The mixture was stirred and ultrasonically agitated. While still in suspension a lacey carbon-coated TEM grid was pulled through the suspension. The grid was allowed to dry in air and then examined in an Amray 1845 FE-SEM followed by examination with a Philips model CM-30 TEM operated at 300 kV. The specimen was given no further treatment, as it appeared stable under beam bombardment. The preparation for the microtomed samples included embedding into a derivation of EPON epoxy resin using EmBed 812. This mixture was centrifuged and cured for 24 h at 60 °C. The embedded block was microtomed to obtain thin sections of 60-80-nm thickness by using a Reichert Ultracut S ultramicrotome with a diamond knife (Diatome). The floated sections were mounted on a 400 mesh Pd-coated Cu grid. The TEM images of these microtomed samples were recorded using a Philips model CM-30 TEM operated at 300 kV at 69 000 to 340 000 electron optical magnification.

#### Experimental Methods and Conditions for Controlled-Release Studies of CdS-Capped, ATP-Encapsulated MSN with Neuroglia Cells (Astrocytes) in Vitro

Wistar rats, raised at Iowa State University, were used for these experiments. Animal care and experimental protocols were in accordance with the guidelines and approval of the Iowa State University Committee on Animal Care.

#### Cell Cultures

Enriched primary astrocyte cultures from neonatal (P<sub>0</sub> to P<sub>3</sub>) rat cerebral cortex were prepared as previously described.<sup>15a</sup> Briefly, freshly dissected cortical tissues from three animals were incubated 50 min at 37 °C in 2.00 mL of Earle's balanced salt solution (EBSS; Gibco-Invitrogen Co.) containing papain (1.54 mg/mL; Sigma-Aldrich Co.). After incubation, tissue was rinsed with EBSS solution and incubated for 5 min in trypsin-inhibitor solution (1 mg/mL; Gibco-Invitrogen Co.). After being rinsed, once with EBSS solution and once with culture medium (consisting of  $\alpha$ -minimum essential medium ( $\alpha$ -MEM; Gibco-Invitrogen Co.) supplemented with 10% heat-inactivated fetal bovine serum (FBS; Gibco-Invitrogen Co.)

and 1.00 mL of penicillin-streptomycin solution (Sigma-Aldrich Co.) per 100 mL, the tissue was mechanically dispersed in culture medium by triturating through a fire-polished glass pipet. The cell suspension was transferred to sterile 15-mL centrifuge tubes and spun at 1000g for 10 min. Cell pellets were resuspended in culture medium ( $\alpha$ -MEM supplemented with 10% heat-inactivated FBS and 1.00 mL of penicillin-streptomycin solution per 100.00 mL) and plated in culture flasks. Cells were maintained at 37 °C in a humidified 5% CO<sub>2</sub>/95% air atmosphere. Culture medium was changed every 2 to 3 days. When mixed cultures reached confluence (9-12 days), the flasks were shaken (260 rpm) for 90 min to remove microglia and dividing type I astroglia. After shaking the cells, medium was replaced, and the flasks were incubated for 1 h to equilibrate with CO<sub>2</sub> in the fresh medium. Cultures were then shaken overnight (12-18 h) at 260 rpm at 37 °C. Cultures enriched in type I astroglia were obtained by trypsinizing (0.25%; Sigma-Aldrich Co.) attached cells for 5 min. Trypsin was inactivated by adding  $\alpha$ -MEM supplemented with the 10% heat-inactivated FBS (serum contains protease inhibitors). Cells were plated on poly-L-lysine-coated coverslips (10.00  $\mu$ g/mL; MW 100 000; Sigma-Aldrich Co.) at a density of  $3.00 \times 10^4$  cells/cm<sup>2</sup>. All experiments were performed on cells that had been in culture for 2-4 days after replating.

#### Characterization of Glial Cultures

An antibody against glial fibrillary acidic protein (GFAP) was used to identify astrocytes following the procedure described in the subsequent Immunocytochemistry section. We confirmed that glial cultures were neuron-free by using antibodies against the tubular protein MAP-2. In astrocyte-enriched cultures immunoreactivity for MAP-2 was absent, while neurons were immunopositive in parallel cultures that contained neurons.

#### Immunocytochemistry

After fixation with 4% paraformaldehyde (Fisher Chemical) for 30 min at room temperature, cells were incubated for 30 min in a 50% goat serum solution containing 1% bovine serum albumin (BSA; Sigma-Aldrich Co.) and 100.00 mM L-lysine (Sigma-Aldrich Co.), to block nonspecific binding, and 0.4% Triton X-100 to permeabilize the membrane. Immunocytochemistry was performed using antibodies raised against glial fibrillary acidic

protein (GFAP; 1:5000; Sigma-Aldrich Co.) and microtubule associated protein (MAP-2; 1:2000; Sigma-Aldrich Co.). Positive controls were established with these antibodies using cortical glia and neurons. Negative controls were established by omitting the specific antiserum. Antibody visualization was accomplished by the employment of the biotinylated secondary antibody, the Vectastain ABC kit (Vector) and the nickel-enhanced 3-3'-diaminobenzidine method.<sup>21</sup> Cells were dehydrated in graded alcohol, cleaned in xylene, and sealed with acrytol on glass slides as shown in Appendix B.

### Intracellular Calcium Imaging

The effect of experimental manipulation on the intracellular calcium concentration ( $[Ca^{2+}]_i$ ) of cultured cells was evaluated by ratiometric imaging techniques.<sup>17</sup> Cells were loaded with Fura 2-AM (5.00  $\mu$ M; Molecular Probes) for 40-60 min at 37 °C; 1.00  $\mu$ L of 25% (w/w) of Pluronic F-127 (Molecular Probes) was mixed with every 4.00 nM of AM ester to aid solubilization of the ester into aqueous medium. Coverslips containing glial cells were washed with normal HEPES-saline solution and further incubated for 10 min at 37 °C to allowed ester hydrolysis of Fura 2-AM. Normal HEPES-saline solution contains (in mM): NaCl 140.00, KCl 5.00, MgCl<sub>2</sub> 2.00, CaCl<sub>2</sub> 2.00, and HEPES (Sigma-Aldrich Co.) 10 (pH 7.4). All image processing and analysis were performed using an Attofluor system with Zeiss microscope. Background subtracted, rationed images (340/380 nm) were used to calculate the  $[Ca^{2+}]_i$  according to a literature-reported method.<sup>19</sup> Calibration was performed in situ according to the procedure provided by the Attofluor, using the Fura-2 Penta K<sup>+</sup> salt (Molecular Probes) as a standard. Using wavelengths of 340 and 380 nm, Fura 2-AM was excited, and the emitted light was collected at 520 nm.

## Results and Discussion

To prepare the MSN material functionalized with a chemically labile linker that can covalently capture the CdS nanoparticles, we first synthesized a mercaptopropyl-derivatized mesoporous silica nanosphere material (thiol-MSN) via our recently reported co-condensation method.<sup>9</sup> As illustrated in Figure 5-2, the surfactant-removed thiol-MSN

material was treated with a methanol solution of 2-(pyridyldisulfanyl)ethylamine, which was synthesized via a literature procedure,<sup>10</sup> at room temperature for 24 h under vigorous stirring to yield the MSN material with 2-(propyldisulfanyl)ethylamine functionality (linker-MSN).

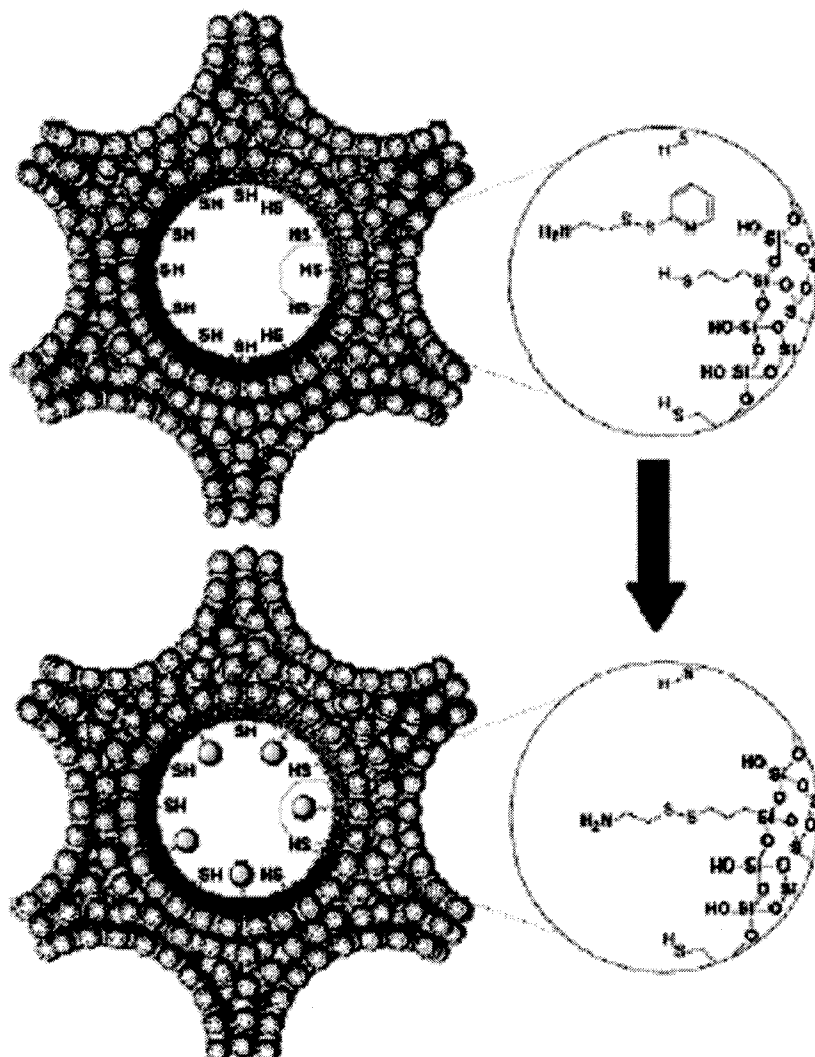


Figure 5-2. Synthesis of 2-(propyldisulfanyl)ethylamine functionalized mesoporous silica nanosphere (linker-MSN) material.

As depicted in Figure 5-3a, b, c, and e, the spherical particle shape and the MCM-41 type of hexagonally packed mesoporous structure of the linker-MSN material are confirmed by scanning and transmission electron microscopy (SEM and TEM, respectively). The  $N_2$  adsorption/desorption isotherms of the material further revealed a BET isotherm typical of

MCM-41 structure (type IV) with a surface area of 941.0 m<sup>2</sup>/g and a narrow BJH pore size distribution (average pore diameter = 2.3 nm). The linker-MSN (100.0 mg) was used as a chemically inert host to soak up the aqueous solutions of vancomycin (3.0 μmol) and ATP (15.5 μmol).

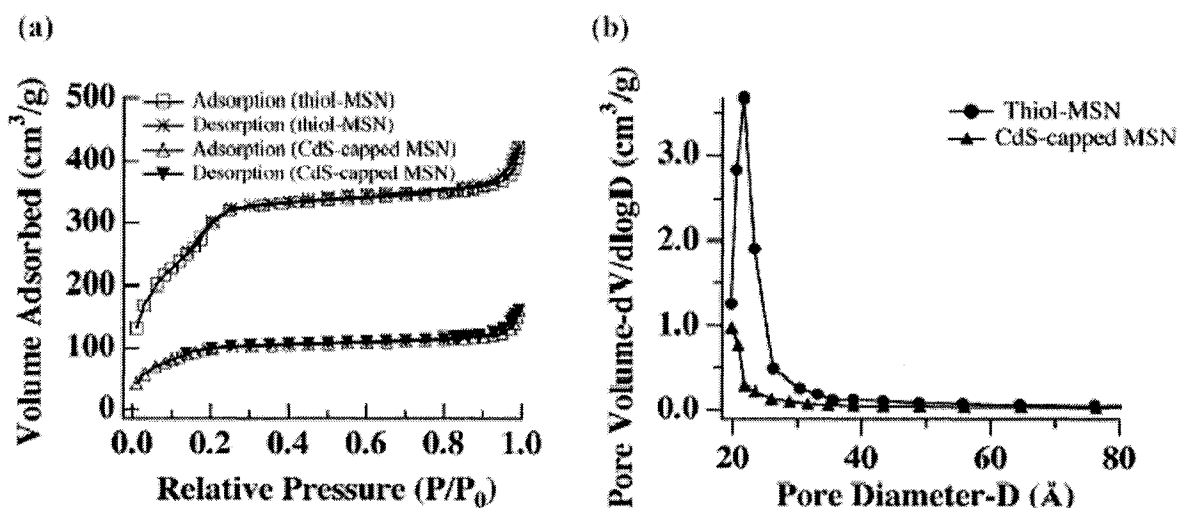


Figure 5-3. (a) BET nitrogen adsorption/desorption isotherms of the thiol-MSN material before and after covalent encapsulation of the mercaptoacetic acid-functionalized CdS nanoparticles. (b) BJH pore size distributions for the thiol-MSN and CdS-capped MSN nanocomposite materials. The decrease in surface area and the disappearing of the maximum peak in BJH pore size distribution plot indicate that the mesopores of MSN are capped by the CdS nanoparticles.

TEM investigations of the CdS-capped MSN also provided direct evidence of the CdS distribution both on and in the organically functionalized MSN material. As shown in Figure 5-4d, where the mesopores (porous channels) are represented by the alternating black and white stripes, the CdS nanoparticles are clearly visible on the outside edge and inside the mesopores of the MSN depicted by the lighter areas (indicated by the arrowheads). As opposed to these features observed in the case of CdS-capped MSN, the TEM micrograph of the linker-MSN (Figure 5-4c) prior to the CdS "capping" showed smooth edges and nice contrasts between the mesoporous channels and the silica matrix. Furthermore, compared with the periodically well-organized hexagonal array of mesopores represented by the bright dots shown on the TEM micrograph of the linker-MSN orientated along the pore axis (Figure 5-4e), an additional layer of CdS nanoparticles on the outside of the MSN material and a



large area of disordered hexagonal array of mesopores indicated by the arrows in Figure 5-4f were observed in the case of CdS-capped MSN material.

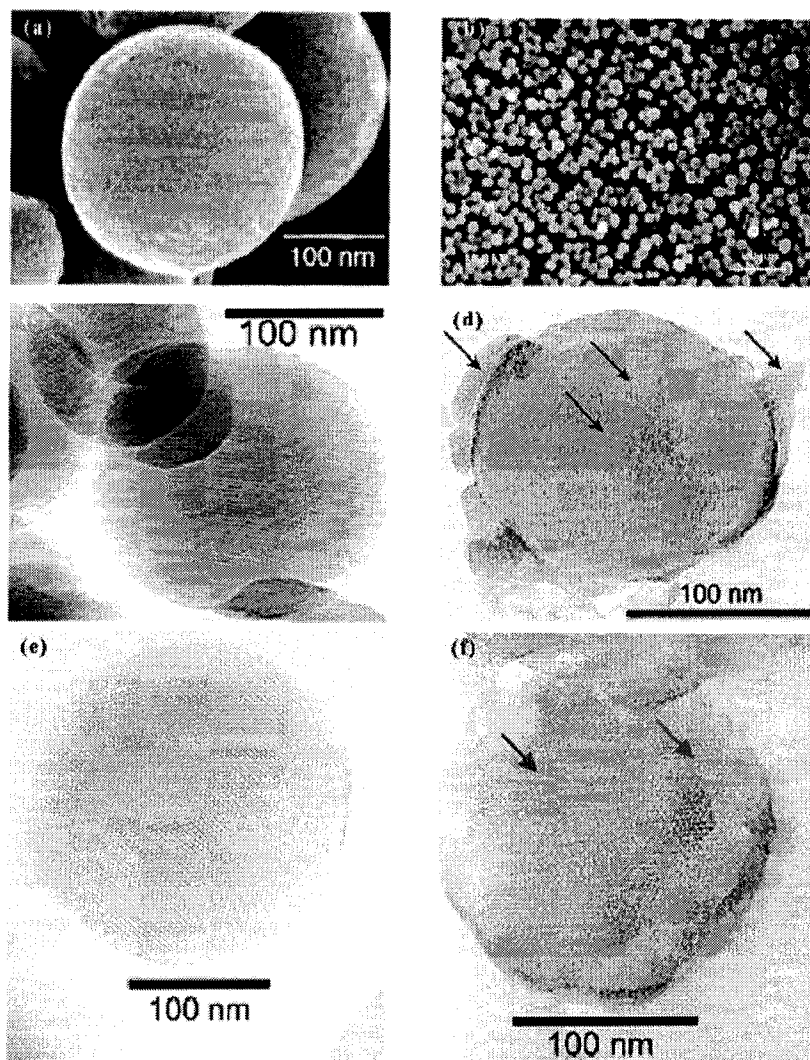


Figure 5-4. SEM (a and b) and TEM (300 kV) micrographs of the linker-MSN (c and e). The MCM-41 type of mesoporous channel structure of the nanospheres is visualized with the parallel stripes (c) and the hexagonally packed light dots (e) shown in the micrographs. The TEM micrographs (d and f) of the CdS-capped MSN clearly exhibit aggregations of CdS nanoparticles on the exterior surface of MSN material represented by dots in the areas indicated by black arrows in (d). A large area (left side of the MSN particle indicated by the blue arrow) displaying light dots packed in a disordered symmetry and an area (green arrow) where the mesopores are hexagonally arranged represent the CdS nanoparticle-capped and uncapped areas of MSN particle shown in (f), respectively. The TEM micrographs (d-f) were measured on ultramicrotomed samples with section thickness of 60-80 nm.

In contrast to the "disordered" area, a small area with mesopores that are packed with a hexagonal symmetry was also noticed on the micrograph. These different areas could be attributed to the fact that most, but not all, mesopores are capped with the CdS nanoparticles. To design a chemically removable cap, we synthesized a mercaptoacetic acid-coated, photoluminescent CdS nanocrystal material with an average particle diameter of 2.0 nm via a literature-reported procedure.<sup>7</sup> As illustrated in Figure 5-1, the water-soluble CdS Nanocrystals with mercaptoacetic acid groups were covalently captured and formed amide bonds by reacting with the mesopore surface-bound 2-(propyl-disulfanyl)ethylamine linkers of the MSN/drug composite material in aqueous solutions. The resulting reaction suspensions were centrifuged, and the CdS-capped MSN/drug composite materials along with the unreacted CdS nanoparticles were filtered. The concentrations of the free vancomycin and ATP molecules in the filtrate were then determined by HPLC. The calculated concentration decreases of solution vancomycin and ATP were attributed to the amounts of mesopore-encapsulated vancomycin (2.5  $\mu$ mol) and ATP (4.7  $\mu$ mol) per 100.0 mg of linker-MSN material. These numbers correspond to ca. 83.9 and 30.3 mol % loading efficiency, respectively.

The successful incorporation of CdS nanoparticles to the MSN matrix was confirmed by various spectroscopy methods.<sup>11</sup> As shown in Figure 5-5a, the covalent immobilization of the surface-functionalized CdS nanoparticles to the linker-MSN material reduced the intensity of the powder X-ray diffraction (XRD) peaks. Such a reduction of scattering contrast between the pores and the framework of the MCM-41 materials due to the pore-filling effect has been reported previously in the literature.<sup>12</sup> Compared with the  $d_{100}$  value of the linker-MSN material, a small increase in that of CdS-capped MSN was observed. The increase of the  $d_{100}$  values may be attributed to the covalent linkage induced pore-filling effect between the CdS nanoparticles and the mesoporous silica matrix. Figure 5-5b showed the high-angle XRD diffraction patterns of the linker-MSN and the CdS-capped MSN materials within the  $2\theta$  range of  $10^\circ - 70^\circ$ . In contrast to the low-intensity diffuse peak of noncrystalline silica observed in the linker-MSN material (Figure 5-5b), two additional peaks are detected in the CdS-capped MSN sample. As depicted in Figure 5-5b, these two peaks are attributed to the diffraction of (111) and (220) lattice planes of the CdS nanoparticles

attached to the mesoporous silica.<sup>13</sup> To further confirm that these CdS nanoparticle "caps" were indeed *covalently* linked to the mesopore surface-bound linker groups, the <sup>13</sup>C solid-state CP-MAS NMR spectra of both the CdS-capped MSN and the linker-MSN were carefully compared and the existence of the covalent linkage between the CdS and MSN materials was clearly observed as shown in the Appendix B.<sup>11</sup>

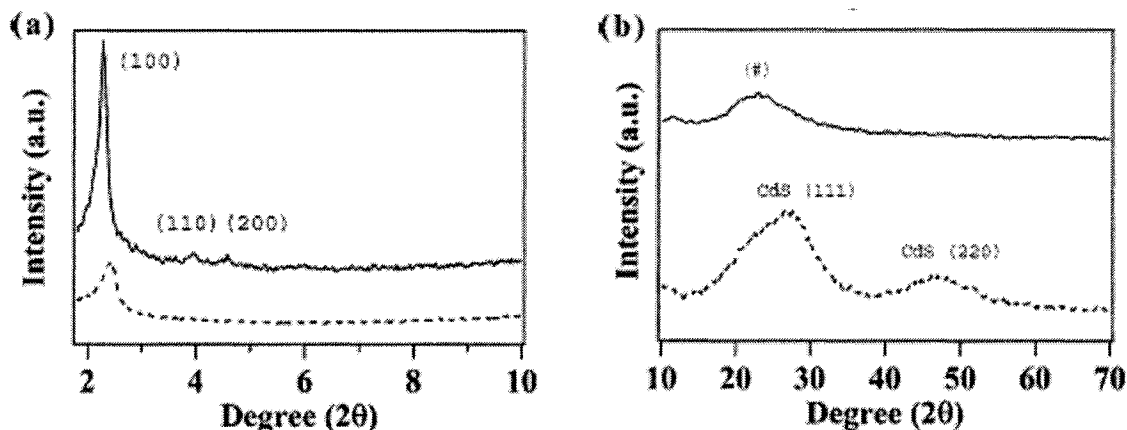


Figure 5-5 Low (a) and high (b) angle powder X-ray diffraction patterns (XRD) of the linker-MSN material before (solid line) and after (dashed line) the immobilization of CdS nanocrystals. (# is the diffuse peak of noncrystalline silica.)

Table 5-1. Structural parameters of the thiol-MSN and the CdS-capped MSN materials

	Powder XRD					Nitrogen Sorption Isotherms		
	Low angle (Silica) (Å)			High angle (CdS) (Å)		BET surface area (m <sup>2</sup> /g)	BET pore volume (mL/g)	BJH pore diameter (Å)
	<i>d</i> <sub>100</sub>	<i>d</i> <sub>110</sub>	<i>d</i> <sub>200</sub>	<i>d</i> <sub>111</sub>	<i>d</i> <sub>220</sub>			
Thiol-MSN	38.6	22.4	19.3	-	-	941.2	0.582	23.0
CdS-capped MSN	36.7	-	-	3.2	1.9	342.3	0.203	-

As shown in Figure 5-6a, the CdS-capped MSN drug/neurotransmitter delivery system exhibited less than 1.0% of drug release in 10 mM PBS buffer solutions (pH 7.4) over a period of 12 h. The result suggested a good capping efficiency of the CdS nanoparticles for encapsulation of the vancomycin and ATP molecules against the undesired leaching problem. Addition of disulfide-reducing molecules, such as DTT and ME, to the aqueous suspension

of CdS-capped MSNs triggered a rapid release of the mesopore-entrapped drug/neurotransmitter. Within 24 h, the release reached 85% of the total release seen in 3 days of vancomycin and ATP after the introduction of 18.5 mM DTT (Figure 5-6a).

Interestingly, the rates of release of vancomycin and ATP showed similar diffusional kinetic profiles, indicating the lack of interaction between these released molecules and the mesoporous silica matrix. However, 53.8% (1.6  $\mu$ mol) of the encapsulated vancomycin was released after 3 days of the DTT-induced uncapping of the mesopores, while only 28.2% (1.3  $\mu$ mol) of the entrapped ATP molecules was able to diffuse away. Such a large difference between the portion of vancomycin and ATP released from the MSN material implied that ATP molecules were more strongly physisorbed to the organically functionalized mesoporous channels than the vancomycin molecules. On the basis of several reports in the literature,<sup>14</sup> vancomycin has an isoelectric point (pI) of 8.3 and therefore is cationically charged under our experimental condition (pH 7.4). Conversely, ATP is anionic in pH 7.4 aqueous solutions. Given that the surface of the linker-MSN material is decorated with the 2-(propylsulfanyl)ethylamine functionality, which is cationic (ammonium cation) at pH 7.4, the attractive electrostatic interaction between the ATP molecules and the linker-functionalized mesopores could be attributed to the stronger physisorption of ATP, whereas the repulsive electrostatic interaction between vancomycin molecules and the linker-derivatized mesopores disfavor the surface adsorption of vancomycin.

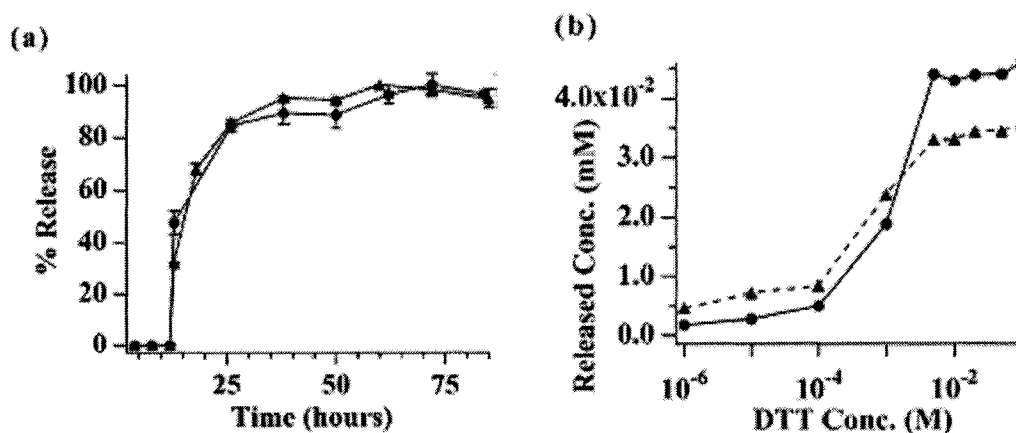


Figure 5-6. The DTT-induced release profiles of Vancomycin (---) and ATP (-▲-) from the CdS-capped MSN system: (a) % release over time. (b) The DTT concentration-dependent releases. Released analyte concentrations were measured with CdS-MSNs (2.3 mg) in pH 7.4 PBS buffers (0.8 mL) after 24 h of the DTT additions.

These results suggested that perhaps only those molecules that are not in direct contact with the pore surface, i.e., nonphysisorbed molecules, could be released under our experimental conditions. Furthermore, in both vancomycin and ATP cases, the amount of drug release after 24 h of the addition of DTT showed similar DTT concentration dependencies (Figure 5b), indicating the rate of release is dictated by the rate of removing the CdS caps. To demonstrate the biocompatibility and utility of our controlled-release delivery system for selective stimulation of certain cell types, ATP-loaded MSNs were introduced into an established astrocyte culture. It has been previously shown that ATP molecules evoke a receptor-mediated increase in intracellular calcium in astrocytes,<sup>15</sup> which is an important regulatory mechanism for many intercellular communications and cooperative cell activities.<sup>16</sup> Astrocyte type-1 cultures were obtained from neonatal rats by following previously published protocol<sup>17</sup> to ensure the absence of neurons that complicate experimental interpretation. Phase-contrast microscopy indicated that cultures were indeed enriched in type-1 astrocytes and devoid of neurons. Immunocytochemistry experiments on these cells demonstrated that all the cultures are more than 95.0% immunopositive for glial fibrillary acidic protein (GFAP) and lacked MAP-2 immunoreactivity.<sup>18</sup> The observed results further confirmed that these cultures are indeed type-1 astrocytes and not neurons. To determine the effect of ATP on cultured astrocytes, we used ratiometric-imaging techniques<sup>17,19</sup> to monitor the glial calcium levels. Cells were loaded with the membrane-permeant  $\text{Ca}^{2+}$ -chelating fluorescent dye (Fura-2 AM),<sup>19</sup> which is a widely used and highly sensitive indicator of intracellular calcium concentration ( $[\text{Ca}^{2+}]_i$ ). The ATP-induced increases of  $[\text{Ca}^{2+}]_i$  (calcium transients)<sup>19</sup> represented by the color changes (increases of fluorescence) of the pseudocolor images of the cells were detected using an Attolfluor system with Zeiss microscope.

To measure the effect of ATP released from the MSN system, astrocytes cultured in the presence of surface immobilized, CdS-capped MSNs with ATP molecules encapsulated inside of the mesoporous channels were first loaded with Fura-2 AM and then placed in a flow cell with a volume of 50.0  $\mu\text{L}$  and a flow rate of 200.0  $\mu\text{L}/\text{min}$  in a flow direction from the top to the bottom of the images shown in Figure 5-7. As shown in Figure 5-7a and c, perfusion application of ME (1 mM for 5 min) resulted in a drastic decrease in the

fluorescence intensity of CdS at the areas of the ATP-loaded MSN piles (MSN-1 and MSN-2) indicating the CdS caps have been released and diffused away from the surface-bound MSNs.

Furthermore, we observed a pronounced increase in intracellular  $[Ca^{2+}]_i$  represented by the color change of the pseudocolor images of Cell-1 and -2 (Figure 5-7a) and the corresponding upward shift of the red and blue curves of those two cells in the time course plot (Figure 5-7c). The observations suggested that the ATP molecules released from the mesoporous silica nanospheres located at the MSN-1 pile have reached their receptors on the cell surface of those astrocytes (for example, Cell-1 and -2) located at the downstream areas of the flow and thereby triggered the corresponding ATP receptor-mediated increase in intracellular calcium concentration. It is interesting to note that only the cells that were situated at the downstream areas relative to the MSN-1 pile (Figure 5-7a) are stimulated by the perfusion application of ME. Throughout the whole period of ME application, no obvious color changes could be observed in the pseudocolor images of those astrocytes that were located at the upstream areas, such as Cell-5, as shown in Figure 5-7a. The result indicated that the intracellular calcium concentrations of those "upstream" astrocytes relative to the MSN-1 pile were not affected by the perfusional introduction of ME. Given that the flow direction is from the top to the bottom of these images, such a phenomenon could be attributed to the fact that the ATP molecules released from the immobilized piles of MSNs by the perfusion application of ME could not diffuse against the flow to reach and stimulate the "upstream" astrocytes (Cell-5).

To confirm that the increase of  $[Ca^{2+}]_i$  was not induced by the ME or the CdS released from the MSNs, two control experiments were performed. First, we obtained an enriched astrocyte type-1 culture via the same protocol but without the presence of MSNs. As shown in Figure 5-8, the perfusion application of ME (1.0 mM for 5 min) to these cells showed no increase in  $[Ca^{2+}]_i$ . A high concentration of ATP (100.0  $\mu$ M) was later introduced to these ME-treated astrocytes. All cells responded to the ATP application with obvious increases in  $[Ca^{2+}]_i$ . Clearly, the ME application did not stimulate the calcium channel activity of these astrocytes to create any noticeable increase in  $[Ca^{2+}]_i$ . Also, such ME treatments did not cause any obvious damage to these cells and they could still respond normally to ATP stimulation.

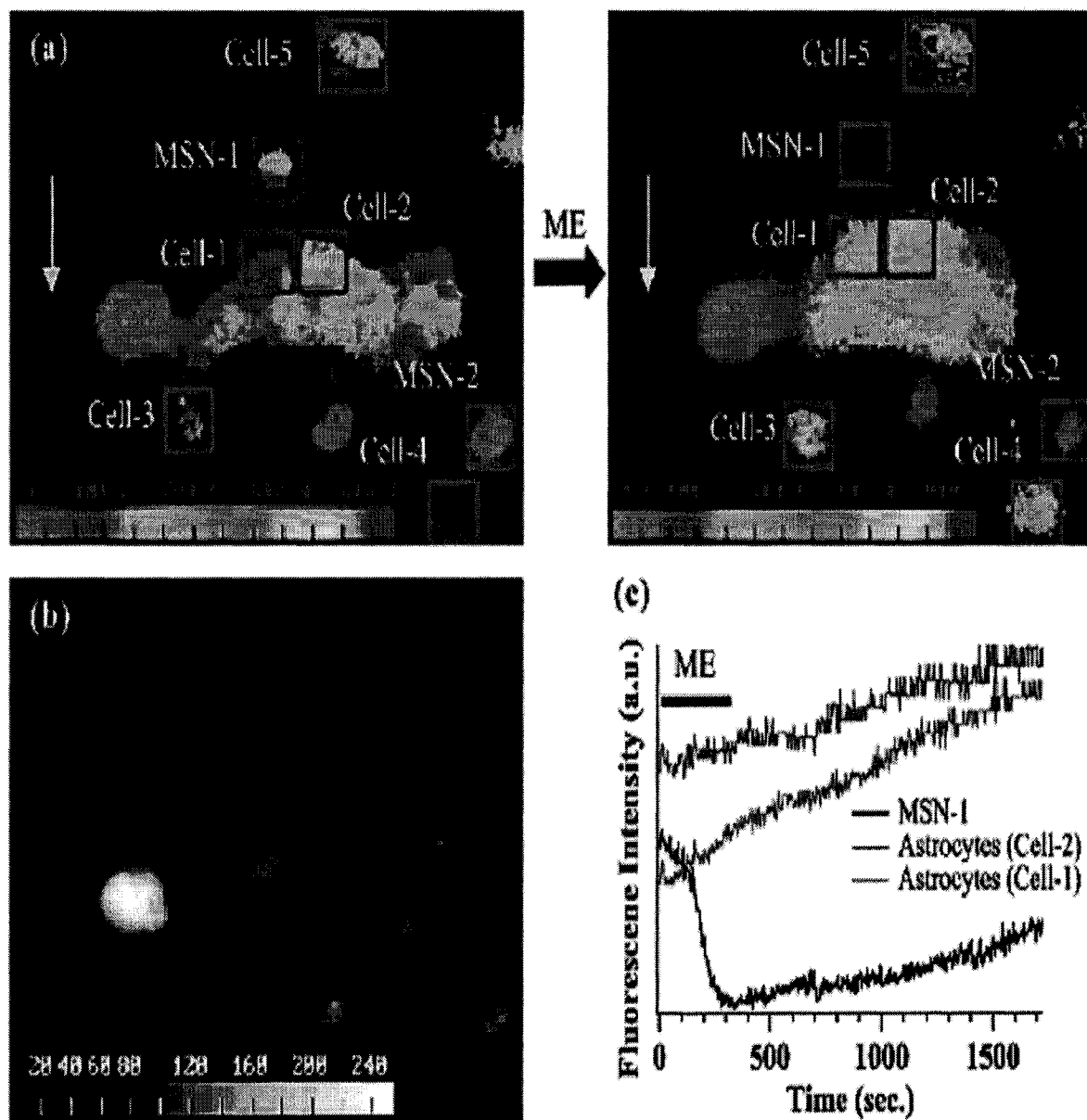


Figure 5-7. Effect of ATP release from CdS-capped MSNs on astrocytes. (a) Top panels show the pseudocolor images of astrocytes loaded with Fura-2 at resting level (top left panel) and after the application of ME (top right panel). The yellow arrows indicate the flow direction of HEPES buffer (pH 7.4). (b) Left bottom panel shows the fluorescence of cells and CdS at 520 nm ( $\lambda_{\text{ex}} = 380$  nm). (c) Right bottom graph is a time course of astrocytes and CdS-capped MSN fluorescence prior to and after the application of ME. (Black bar represents the application time period of ME).

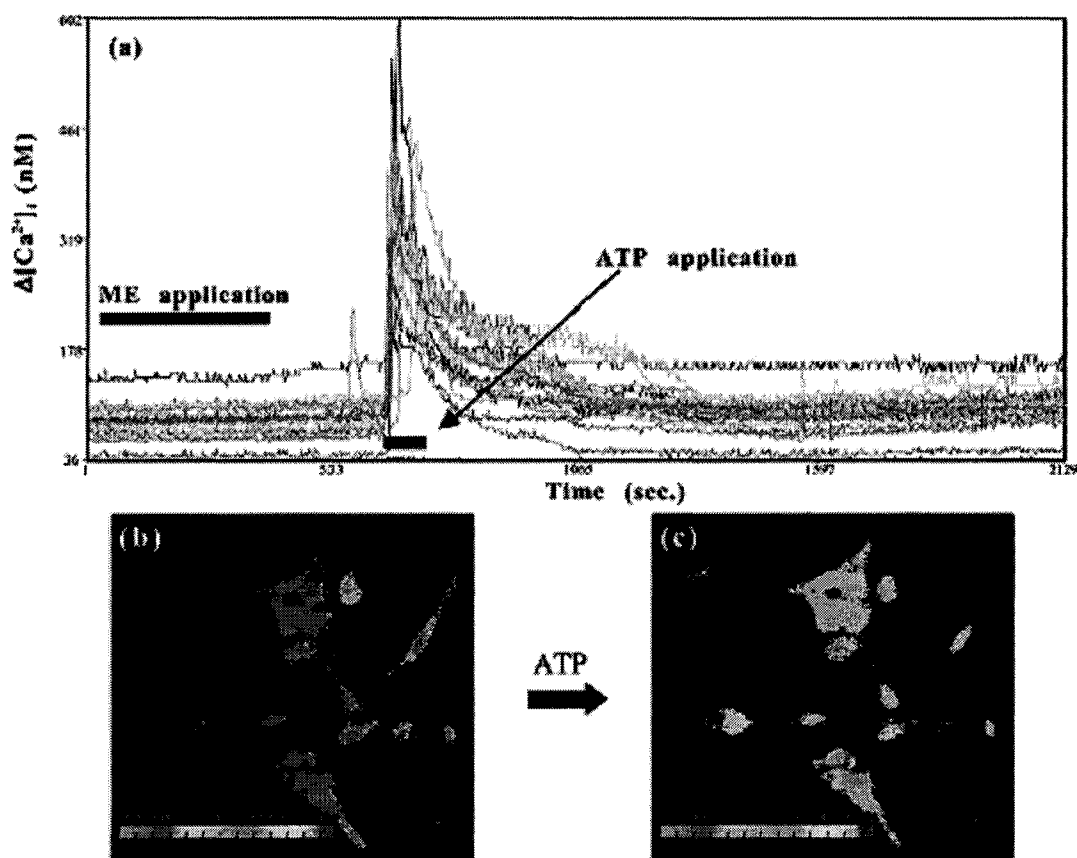


Figure 5-8 (a) Images showing that application of ME on an astrocyte culture loaded with the intracellular  $Ca^{2+}$ -chelating fluorophore (Fura 2-AM) without the presence of MSN failed to produce any  $[Ca^{2+}]_i$  response of astrocytes. (b) Pseudo-color image of astrocytes taken after the ME application showed no increase or decrease in  $[Ca^{2+}]_i$  of the cells. (c) The same cells responded to the perfusion application of 100.0  $\mu$ M ATP indicated by the increase of fluorescence intensity of the pseudo-color image of astrocytes, i.e.,  $[Ca^{2+}]_i$  increases.

To determine the effect of CdS nanoparticles on the  $[Ca^{2+}]_i$  of astrocytes under our experimental conditions, we cultured the enriched type-1 astrocytes in the presence of CdS-capped MSNs without ATP encapsulation. Perfusion application of 100.0  $\mu$ M ATP only increased the fluorescence intensity ( $[Ca^{2+}]_i$  increased) of the areas where the astrocytes are located, whereas the fluorescence intensity of those of CdS-capped MSNs stayed constant as depicted in the pseudo-color images of the culture before (Figure 5-9a) and after (Figure 5-9b) the ATP application. This result showed that apparently the astrocytes responded normally to ATP stimulation in the presence of CdS-capped MSNs. The culture of astrocytes and CdS-capped MSNs was then subjected to the same ME application. As shown in Figure 8b and c,



no detectable changes in  $[Ca^{2+}]_i$  were observed in the areas of astrocytes, but drastic decreases of fluorescence could be noticed easily in those areas of CdS-capped MSNs indicating the release of CdS caps upon ME application.

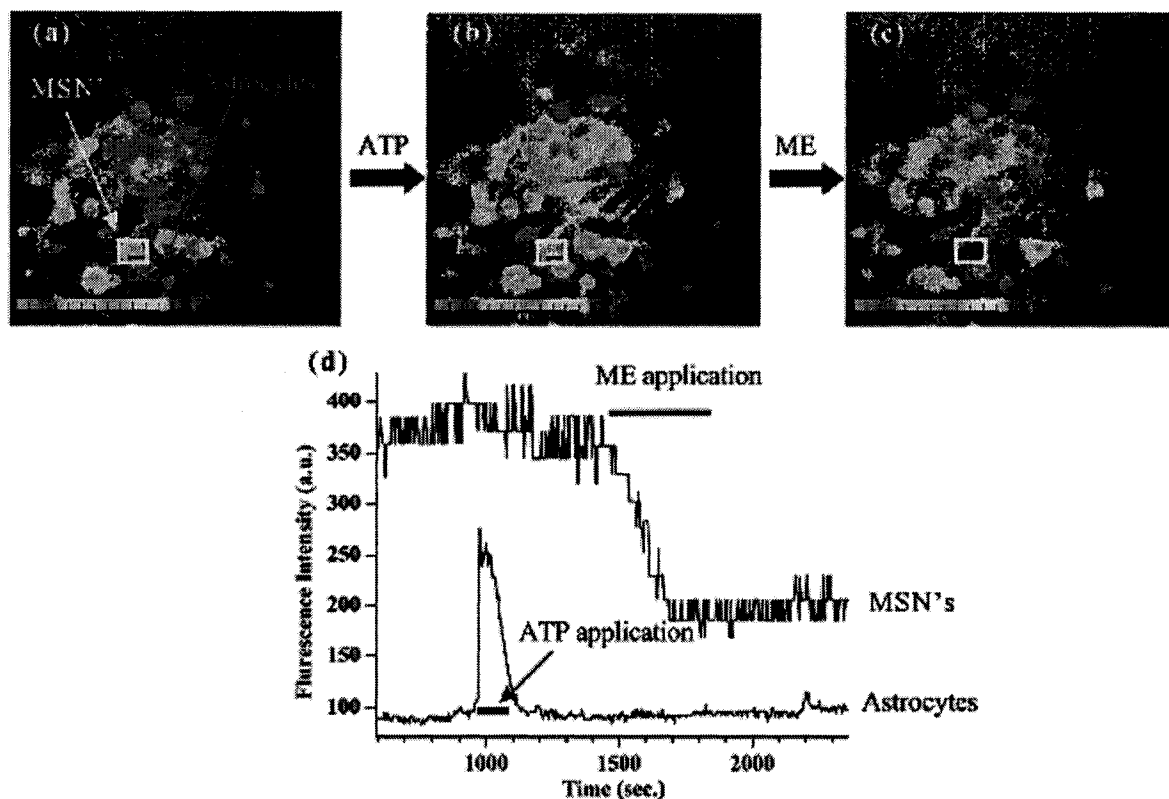


Figure 5-9 Pseudo-color images of an astrocyte culture in the presence of random piles of CdS-capped MSNs with empty mesoporous channels (no ATP encapsulation) before (a) and after (b) the application of ATP (100.0  $\mu$ M). An increase in  $[Ca^{2+}]_i$  of the astrocytes (lower square, red) located adjacent to a pile of MSNs (upper square, yellow) upon the perfusion application of ATP was observed (d, lower curve). The result suggested that the astrocytes are responsive to ATP stimulation. Interestingly, significant decrease of the fluorescence intensity (c and d, upper curve) of the pile of MSNs (upper square, yellow) was observed upon the perfusion application of ME due to the uncapping of CdS (diffusing away from the area of interest). Concurrently, the adjacent astrocytes did not show any detectable response during the application of ME.

## Conclusions

In conclusion, we have demonstrated that the organically functionalized MCM-41 type of mesoporous silica nanosphere material can be used as a novel controlled-release delivery carrier that are stimuli responsive. Given that the loading and release mechanism of

the MSN system is based on the capping and uncapping of the openings of the mesopores with CdS nanoparticles, no chemical modification of the molecules of interest is needed. In addition, the biocompatibility and stability of the MSN material allow us to utilize such a system to investigate various intercellular chemical/neurochemical interactions in vitro. We envision that this MSN system could play a significant role in developing new generations of site-selective, controlled-release delivery, and interactive sensory nanodevices.

### Acknowledgements

This research was supported by the United States DOE Ames Laboratory (MPC-PSI grant) and the NSF (CAREER award: CHE-0239570 and IBN-9604862). We thank Dr. M. J. Kramer and Mr. F. C. Laabs for experimental assistance in TEM measurements of the materials and helpful discussions.

### References

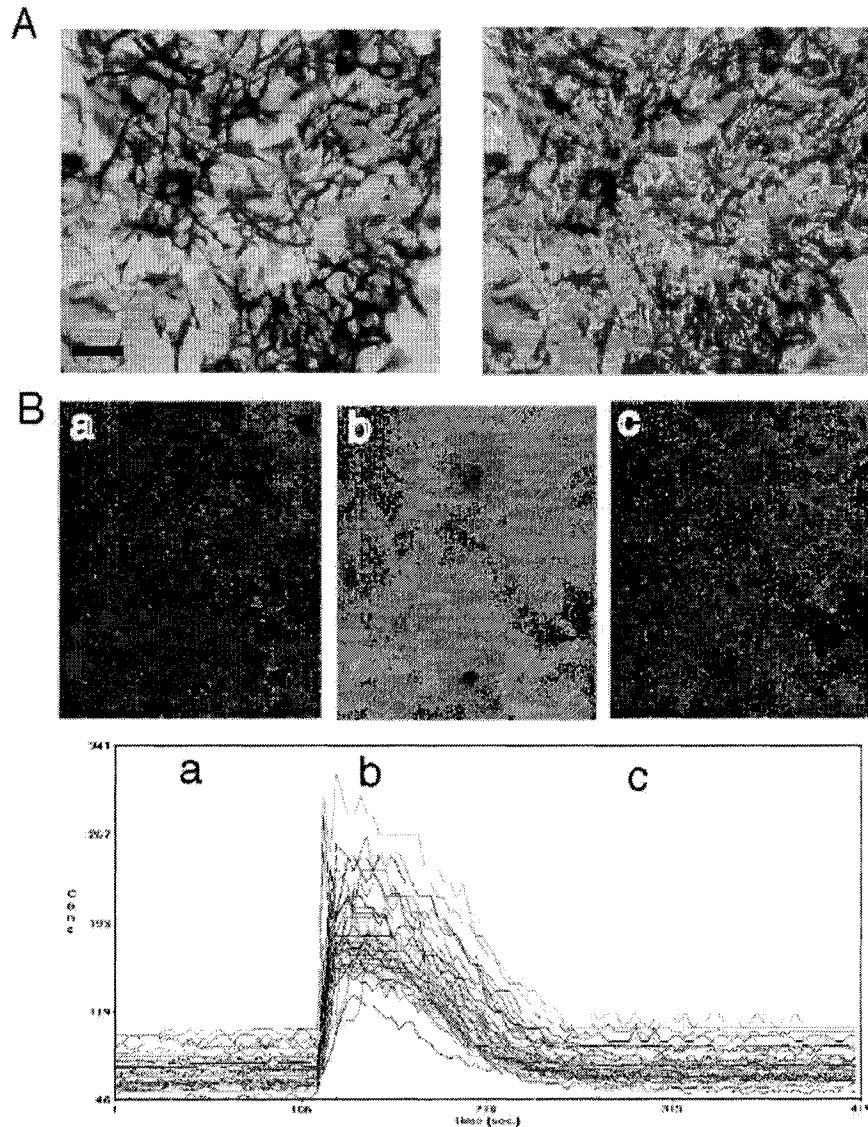
1. (a) Stein, A.; Melde, B. J.; Schroden, R. C. *Adv. Mater. (Weinheim, Ger.)* **2000**, *12*, 1403. (b) Sayari, A.; Hamoudi, S. *Chem. Mater.* **2001**, *13*, 3151 and references therein.
2. (a) Vallet-Regi, M.; Ramila, A.; del Real, R. P.; Perez-Pariente, J. *Chem. Mater.* **2001**, *13*, 308. (b) Munoz, B.; Ramila, A.; Perez-Pariente, J.; Diaz, I.; Vallet-Regi, M. *Chem. Mater.* **2003**, *15*, 500. (c) Ramila, A.; Munoz, B.; Perez-Pariente, J.; Vallet-Regi, M. *J. Sol.-Gel Sci. Technol.* **2003**, *26*, 1199.
3. (a) Diaz, J. F.; Balkus, K. J., Jr. *J. Mol. Catal. B: Enzym.* **1996**, *2*, 115. (b) Han, Y.-J.; Stucky, G. D.; Butler, A. *J. Am. Chem. Soc.* **1999**, *121*, 9897. (c) Kisler, J. M.; Dahler, A.; Stevens, G. W.; O'Connor, A. J. *Microporous Mesoporous Mater.* **2001**, *44-45*, 769. (d) Yiu, H. H. P.; Wright, P. A.; Botting, N. P. *Microporous Mesoporous Mater.* **2001**, *44-45*, 763. (e) Takahashi, H.; Li, B.; Sasaki, T.; Miyazaki, C.; Kajino, T.; Inagaki, S. *Microporous Mesoporous Mater.* **2001**, *44-45*, 755.

4. (a) Radin, S.; Ducheyne, P.; Kamplain, T.; Tan, B. H. *J. Biomed. Mater. Res.* **2001**, *57*, 313. (b) Aughenbaugh, W.; Radin, S.; Ducheyne, P. *J. Biomed. Mater. Res.* **2001**, *57*, 321. (c) Kortesus, P.; Ahola, M.; Kangas, M.; Kangasniemi, I.; Yli-Urpo, A.; Kiesvaara, J. *Int. J. Pharm.* **2000**, *200*, 223.
5. (a) Uhrich, K. E.; Cannizzaro, S. M.; Langer, R. S.; Shakesheff, K. M. *Chem. Rev.* **1999**, *99*, 3181. (b) Langer, R. *Acc. Chem. Res.* **1993**, *26*, 537 and references therein.
6. Li, Y.; Kissel, T. *J. Controlled Release* **1993**, *27*, 247 and references therein.
7. Colvin, V. L.; Goldstein, A. N.; Alivisatos, A. P. *J. Am. Chem. Soc.* **1992**, *114*, 5221.
8. Chan, W. C.; Nie, S. *Science (Washington, D. C.)* **1998**, *281*, 2016.
9. (a) Lin, V. S.-Y.; Lai, C.-Y.; Huang, J.; Song, S.-A.; Xu, S. *J. Am. Chem. Soc.* **2001**, *123*, 11510. (b) Lin, V. S.-Y.; Radu, D. R.; Han, M.-K.; Deng, W.; Kuroki, S.; Shanks, B. H.; Pruski, M. *J. Am. Chem. Soc.* **2002**, *124*, 9040.
10. Ebright, Y. W.; Chen, Y.; Kim, Y.; Ebright, R. H. *Bioconjugate Chem.* **1996**, *7*, 380.
11. See Supporting Information for the BET isotherm, BJH pore size distribution, and solid-state  $^{13}\text{C}$  CPMAS NMR spectra of both the linker-MSN and the CdS-capped MSN materials.
12. (a) Marler, B.; Oberhagemann, U.; Vortmann, S.; Gies, H. *Microporous Mater.* **1996**, *6*, 375. (b) Winkler, H.; Birkner, A.; Hagen, V.; Wolf, I.; Schmechel, R.; Von Seggern, H.; Fischer, R. A. *Adv. Mater. (Weinheim, Ger.)* **1999**, *11*, 1444. (c) Zhang, W.-H.; Shi, J.-L.; Wang, L.-Z.; Yan, D.-S. *Chem. Mater.* **2000**, *12*, 1408. (d) Zhang, W.-H.; Shi, J.-L.; Chen, H.-R.; Hua, Z.-L.; Yan, D.-S. *Chem. Mater.* **2001**, *13*, 648.
13. (a) Kumar, A.; Mandale, A. B.; Sastry, M. *Langmuir* **2000**, *16*, 9299. (b) Diaz, D.; Rivera, M.; Ni, T.; Rodriguez, J.-C.; Castillo-Blum, S.-E.; Nagesha, D.; Robles, J.; Alvarez-Fregoso, O.-J.; Kotov, N. A. *J. Phys. Chem. B* **1999**, *103*, 9854. (c) Weller, H.; Schmidt, H. M.; Koch, U.; Fojtik, A.; Baral, S.; Henglein, A.; Kunath, W.; Weiss, K.; Dieman, E. *Chem. Phys. Lett.* **1986**, *124*, 557. (d) Yang, J.; Zeng, J.-H.; Yu, S.-H.; Yang, L.; Zhou, G.-E.; Qian, Y.-T. *Chem. Mater.* **2000**, *12*, 3259.
14. Takacs-Novak, K.; Noszal, B.; Tokes-Kovesdi, M.; Szasz, G. *Int. J. Pharm.* **1993**, *89*, 261 and references therein.

15. (a) Jeremic, A.; Jeftinija, K.; Stevanovic, J.; Glavaski, A.; Jeftinija, S. *J. Neurochem.* **2001**, *77*, 664. (b) Neary, J. T.; Laskey, R.; Van Breemen, C.; Blicharska, J.; Norenberg, L. O. B.; Norenberg, M. D. *Brain Res.* **1991**, *566*, 89. (c) Zhu, Y.; Kimelberg, H. K. *J. Neurochem.* **2001**, *77*, 530.
16. (a) Wang, Z.; Haydon, P. G.; Yeung, E. S. *Anal. Chem.* **2000**, *72*, 2001. (b) Newman, E. A.; Zahs, K. R. *Science (Washington, D.C.)* **1997**, *275*, 844.
17. Jeftinija, S. D.; Jeftinija, K. V.; Stefanovic, G.; Liu, F. *J. Neurochem.* **1996**, *66*, 676.
18. See Supporting Information for the experimental details of immunocytochemistry and stimulatory effect of ATP on the cultured astrocytes.
19. Gryniewicz, G.; Poenie, M.; Tsien, R. Y. *J. Biol. Chem.* **1985**, *260*, 3440.
20. (a) Farin, D.; Piva, G. A.; Gozlan, I.; Kitzes-Cohen, R. *J. Pharm. Biomed. Anal.* **1998**, *18*, 367. (b) Veciana-Nogues, M. T.; Izquierdo-Pulido, M.; Vidal-Carou, M. C. *Food Chem.* **1997**, *59*, 467.
21. Jeftinija, S.; Liu, F.; Jeftinija, K.; Urban, L. *Regul. Pept.* **1992**, *39*, 123.

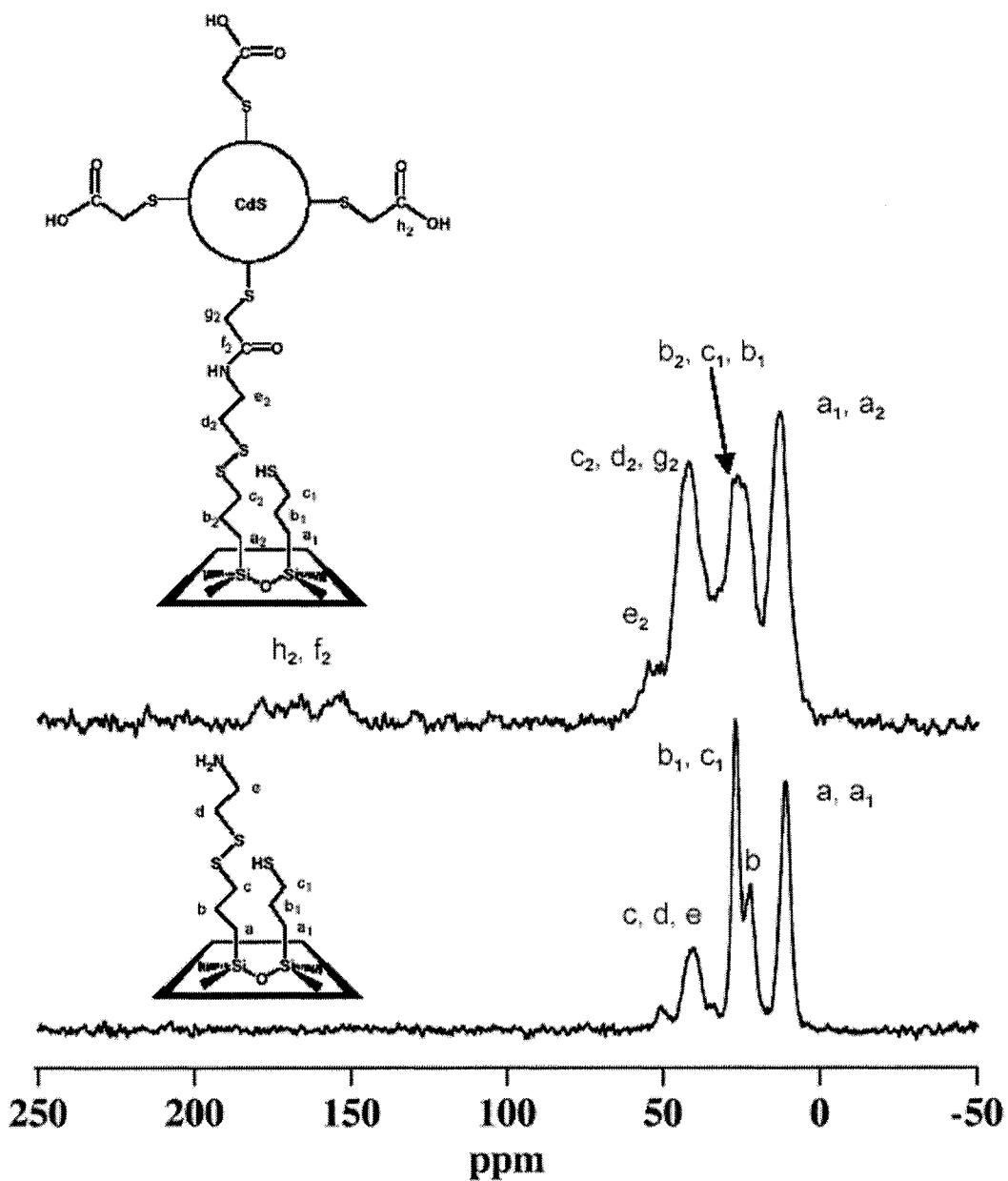
## Appendix A

## Immunocytochemistry



Appendix A **(A)** Stimulatory effect of ATP on cultured astrocytes. Panel illustrates bright field (left image) and phase contrast (right image) images of GFAP immunostained cortical astrocytes. **(B)** Panels illustrate pseudocolor images of baseline **(a)**, ATP-induced increase **(b)**, and recovered **(c)** ratio in fluorescence of free and bound Fura-2. Images a taken at the time indicated on time course graph in lower panel. Black bar represents the duration of perfusion application of ATP 10  $\mu$ M. In resting conditions, the cytoplasmic calcium level of glia was  $91 \pm 2$  nM ( $n=136$ , in three separate experiments). Perfusion application of ATP (10  $\mu$ M) for 60 seconds reliably raised the cytoplasmic level of free calcium in all cells tested. The increase of intracellular calcium reached the peak of  $207 \pm 7$  nM ( $n = 136$ , in three separate experiments) in about 10 seconds after the onset of ATP application and was sustained for several minutes. Space bar = 100  $\mu$ M.

## Appendix B



Appendix B. Solid state  $^{13}\text{C}$  CP-MAS NMR spectra of the surfactant-removed linker-MSN (below) and CdS-capped MSN (above).

Chapter 6. Real-Time ATP Imaging of Tunable Release from a MCM-41-type Mesoporous Silica Nanosphere-Based Delivery System

A paper submitted to *Chemistry of Materials*

Gruenhagen, J.A.; **Lai, C.-Y.**; Radu, D.R.; Lin, V.S.-Y.; Yeung, E.S.

Ames Laboratory-USDOE and Department of Chemistry, Iowa State University, Ames, Iowa  
50011-3111

Abstract

We designed a mesoporous silica nanosphere (MSN) material with tunable release capability for drug delivery applications. Adenosine 5-triphosphate (ATP) molecules were encapsulated within the MSNs by immersing dry nanospheres in aqueous solutions of ATP followed by capping of the mesopores with *chemically removable caps*, such as CdS nanoparticles and poly(amido amine) dendrimers (PAMAM), via a disulfide linkage. We employed luciferase chemiluminescence imaging to investigate the kinetics and mechanism of the ATP release with various disulfide-reducing agents as uncapping triggers. By varying the chemical nature of the “cap” and “trigger” molecules in our MSN system, we discovered that the release profiles could indeed be regulated in a controllable fashion.

Introduction

Nanomaterial<sup>1</sup> research has attracted much attention recently for their potential applications in electronics,<sup>2-4</sup> electro-optics,<sup>5</sup> biosensors,<sup>6-8</sup> etc. One particularly interesting application is the development of novel nanomaterials-based drug delivery systems. Traditionally, responsive polymer systems have been employed in such devices.<sup>9,10</sup> For example, degradable polymers are synthesized in the presence of the drug molecule of interest.<sup>11</sup> The resulting polymer/drug composite materials usually exhibit slow rates of drug release under normal conditions. Upon stimulation, the degradation of polymer matrix is accelerated, and the release of drug molecules is thereby enhanced. Drug delivery polymers

that are responsive toward several types of stimulants, such as temperature, pH, and magnetic/electric field, have been reported in the literature.<sup>12-15</sup>

In addition to polymer-based drug delivery systems, the organically functionalized MCM-type mesoporous silica materials<sup>16,17</sup> offer several attractive features, such as stable mesoporous structures, large surface areas, tunable pore sizes and volumes, and well-defined surface properties, that are ideal for encapsulation of pharmaceutical drugs,<sup>18-21</sup> proteins,<sup>22-26</sup> and other biogenic molecules.<sup>27</sup> We have recently reported the synthesis and characterization of a unique drug delivery system, which is based on a mesoporous silica nanosphere (MSN) material and surface-derivatized CdS nanocrystals.<sup>27</sup> In contrast to many current polymer-based delivery systems, the molecules of interest were encapsulated inside the porous framework of the MSN not by adsorption or sol-gel types of entrapment, but by covalently capping the openings of the mesoporous channels with size-defined CdS nanocrystals to physically block the drugs from leaching out. Drug molecules loaded into the pores were released by the addition of disulfide bond-reducing molecules as “uncapping triggers”. The rate of release was controlled by the concentration of the trigger molecules. Prior to uncapping, the CdS-capped MSN system exhibited negligible release of drug molecules. The “zero release” feature along with the ability to tune the rate of release by varying stimulant concentrations are important prerequisites for developing delivery systems for many site-specific applications, such as delivery of highly toxic anti-tumor drugs, hormones, and neurotransmitters to certain cell types and tissues. To investigate the release mechanism and kinetics, we monitored the dithiothreitol- (DTT) and mercaptoethanol- (ME) triggered release of ATP and vancomycin from the CdS-capped MSN system utilizing high performance liquid chromatography (HPLC).<sup>27</sup> While successful, HPLC was only sensitive enough to detect drug release on the hour timescale, which cannot provide the detailed temporal profile of release.

To gain further insight on how the release mechanism and kinetics can be fine tuned by the chemical nature of the “cap” and “trigger” molecules in our MSN system, we report herein on the synthesis and characterization of a new adenosine triphosphate (ATP) loaded MSN material capped with poly(amido amine) dendrimers (PAMAM).<sup>28-30</sup> As depicted in Scheme 6-1, a highly sensitive method of ATP chemiluminescence imaging was used to monitor the release of ATP from MSN materials capped with PAMAM dendrimers or CdS



nanoparticles that are triggered by three different disulfide reducing agents, i.e., DTT, ME, and tris(2-carboxyethyl)phosphine (TCEP),<sup>31</sup> in real time. The imaging method was based on our previously reported luminescence imaging assay by detecting the ATP-induced chemiluminescence of luciferase *in situ*.<sup>32</sup> Through use of an intensified charge-coupled device (iCCD) camera attached to a microscope, real-time imaging of release of ATP from glial cells with a detection limit of  $10^{-8}$  M was achieved.<sup>33</sup> By using this highly sensitive and selective imaging method, we investigated the effects of the aforementioned uncapping triggers in regulating the magnitudes and kinetics of ATP release from the two MSN materials capped with CdS nanoparticles and PAMAM dendrimers.

## Materials and Methods

### Experimental Section

Firefly luciferase (from *Photinus pyralis*) was obtained from R & D Systems (Minneapolis, MN). All other chemicals were from Aldrich (Milwaukee, WI) and Sigma (St. Louis, MO) and used as received. Low ionic strength HEPES buffer contained 10 mM 4-(2-hydroxyethyl)-1-piperazineethanesulfonic acid (HEPES), 5 mM KCl, and 5 mM NaCl (pH = 7.75). Chemiluminescence imaging solution was comprised of low ionic strength HEPES buffer with 100  $\mu\text{g}/\text{mL}$  firefly luciferase and 205  $\mu\text{M}$  D-luciferin. Nanopure water (18.1 MHz) prepared from a Barnstead E-pure water purification system was employed throughout. PBS buffer (10 mM, pH 7.4) solutions with the total ionic strength of 0.06 M were prepared and used as the solvent for all the loading experiments.

Loading of ATP into the mesoporous framework of linker-MSN and the capping of the mesopores with mercaptoacetic acid-functionalized CdS nanoparticles

2-(Propyl)disulfanyl)ethylamine-functionalized MSN (linker-MSN) and mercaptoacetic acid-derivatized cadmium sulfide (CdS) nanoparticles were synthesized and purified as described previously.<sup>27</sup> The purified linker-MSN material (100 mg) was incubated in a 10 mM PBS buffer (0.60 mL, pH 7.4) solution of ATP (5 mM) for 24 h. The

mercaptoacetic acid-functionalized CdS nanoparticles (0.15 mmol) were dissolved in 2 mL of the aforementioned PBS buffer with ATP (5 mM). 1-[3-(Dimethylamino)propyl]-3-ethylcarbodiimide hydrochloride (EDC, 57.5 mg, 0.30 mmol) was added to the CdS/ATP solution. The resulting solution of CdS was then added to the MSN/ATP suspension. The reaction mixture was stirred at room temperature for 24 h. The suspension was centrifuged at 12 000 rpm for 3 min. The precipitates (ATP-loaded, CdS-capped MSNs) were isolated and dried under vacuum. Previous to each ATP imaging experiment, ATP-loaded MSN (10 mg) was redispersed in 1.5 mL of PBS buffer (pH 7.4), followed by repeating wash/sonication/centrifugation cycles for five times to remove physisorbed ATP molecules from the exterior surface of the material.

Loading of ATP into the mesoporous framework of linker-MSN and the capping of the mesopores with G2.5 or G4.5 PAMAM dendrimers

The purified linker-MSN material (100 mg) was incubated in the aforementioned PBS buffer solution (0.7 mL, pH 7.4) of ATP (5 mM) for 24 h. The G2.5 and G4.5 PAMAM dendrimers were purchased from Aldrich as 10% and 5% w/w methanol solutions, respectively. In a typical experiment, 2 mL of G2.5 or G4.5 PAMAM dendrimer-containing methanol solution was first evaporated, followed by the addition of 2 mL of PBS buffer containing EDC (30 mg, 0.16 mmol) to re-dissolve and activate the PAMAM dendrimers. The resulting PAMAM solution was then added to the MSN with ATP (5mM) suspension. The reaction mixture was stirred at room temperature for 24 h. The resulting precipitates (ATP- loaded, G2.5 or G4.5-capped MSNs) were isolated and purified via the same washing procedures described above.

Scanning and transmission electron microscopy

Particle morphology of these materials was determined by scanning electron microscopy (SEM) using a JEOL 840A scanning electron microscope with 10 kV accelerating voltage and 0.005 nA of beam current for imaging. For transmission electron microscopy (TEM) studies, a small aliquot of ATP-loaded MSN was placed between two clean glass slides. Slides were rubbed back and forth to break up larger clumps. The resulting powder was washed into a petri dish with acetone. The mixture was stirred and ultrasonically

agitated. While still in suspension, a lacey carbon-coated TEM grid was pulled through the suspension. The grid was allowed to dry in air and then examined in an Amray 1845 FE-SEM followed by examination with a Philips model CM-30 TEM operated at 300 kV with 69 000 to 340 000 electron optical magnification. The specimen was given no further treatment, as it appeared stable under beam bombardment.

#### ATP imaging

ATP imaging was performed on the stage of an inverted microscope (Axiovert 100 TV, Zeiss, Germany). Chemiluminescence signal was collected with a Zeiss Aplanachromat 20X microscope objective (NA = 0.75) and detected with an iCCD (EEV 576 x 384 pixels CCD chip, Roper Scientific, Trenton, NJ) attached to the camera mount of the microscope. Nanosphere bulk samples were incubated in imaging solution for at least four hours prior to conducting experiments. The nanospheres were centrifuged down and the supernatant was replaced with fresh imaging solution. Images were collected at a frequency of 0.80 Hz with 1000 ms exposure times. All experiments were performed at room temperature.

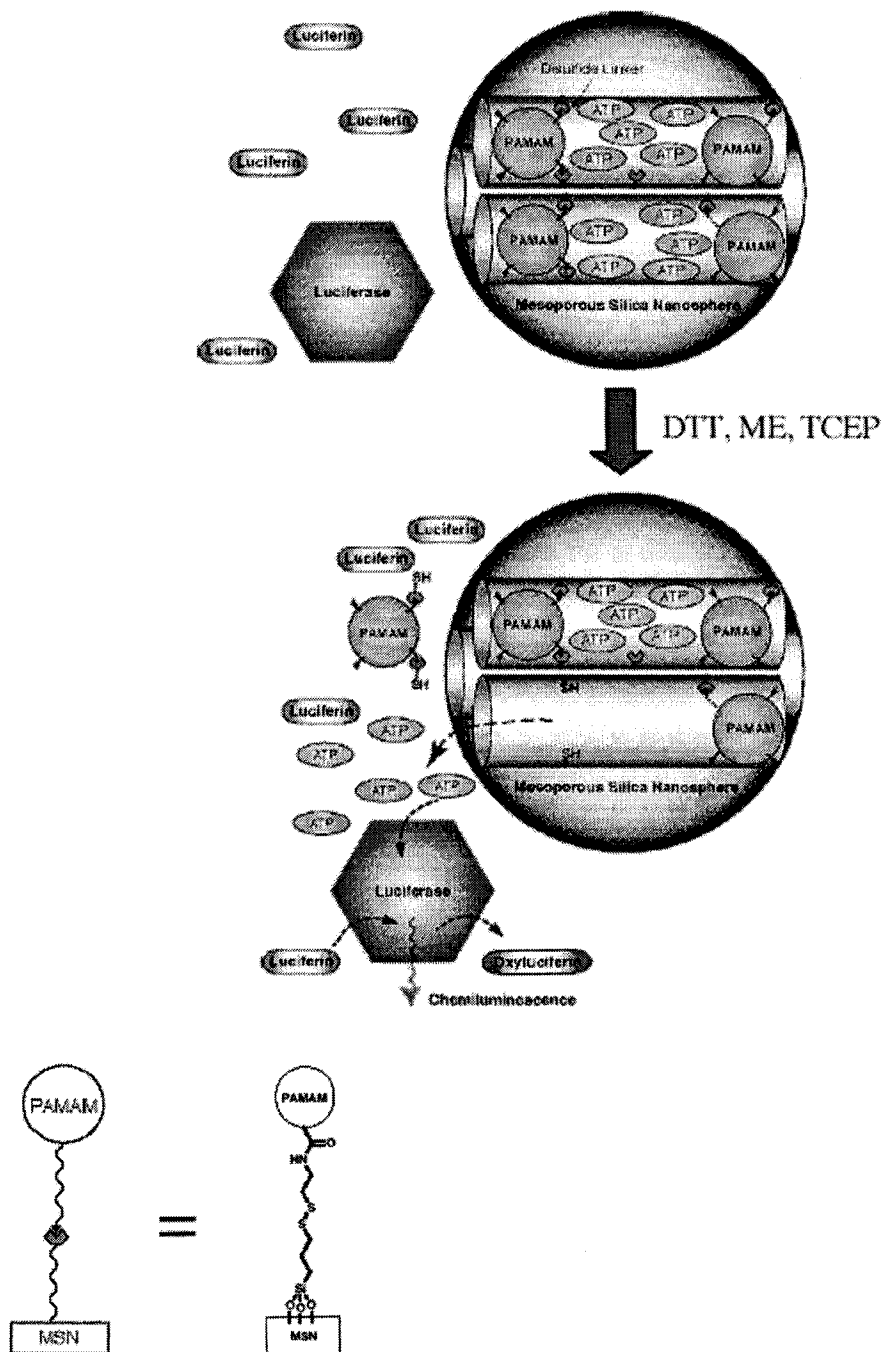
#### Data presentation/analysis

Chemiluminescence signal was obtained and processed with Winview32 software (Roper Scientific). The number of pixels over a threshold value was tabulated for each particle and each frame of data. The ATP concentrations were calculated from a calibration curve obtained with the identical imaging parameters. Displayed images are the average of 50 frames for clarity.

## Results and Discussion

#### Characteristics of end-capped mesoporous silica nanospheres

The synthesis and characterization of ATP-loaded, CdS-capped MSN material (CdS-MSN) were described in our previous report.<sup>27</sup> (see Scheme 6-1).



Scheme 6-1.

As shown in Figure 6-1A, the G4.5 PAMAM dendrimer-capped MSN (PAMAM-MSN) material consists of spherical-shaped nanoparticles with an average particle diameter of 200 nm.

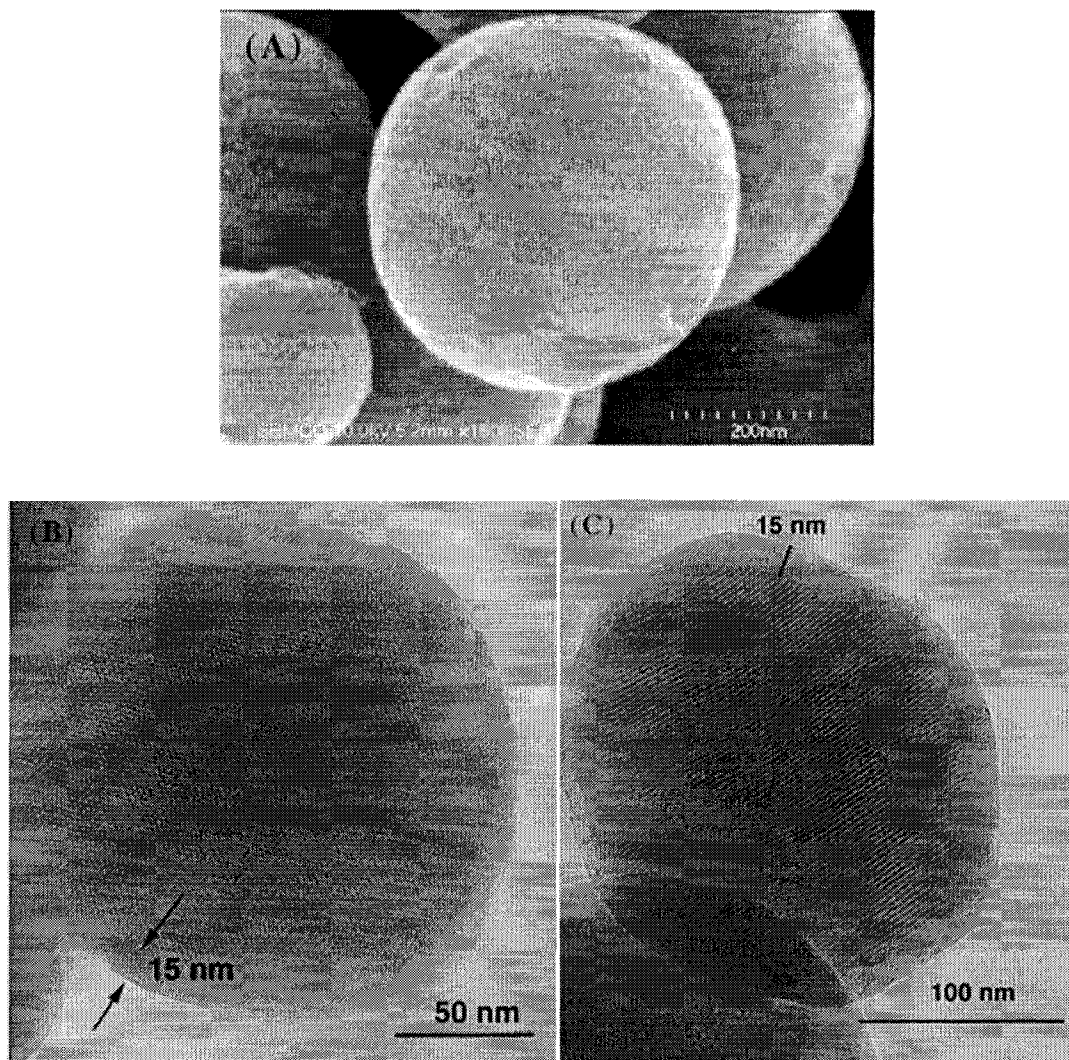


Figure 6-1. SEM (A) and TEM (B, C) micrographs of PAMAM dendrimer-capped MSN. The channel structure is revealed as the hexagonally packed dots shown in B. The lines traversing the entire particle in C are the pores, as viewed perpendicular to the pore axis. Also visible is the PAMAM dendrimer coating along the entire perimeter of the particle.

The MCM-41 type of mesoporous channel structure of the PAMAM-MSN was visualized with the linear pores (2.3 nm in diameter) traversing their entire length and the hexagonally array of mesopores shown in the transmission electron micrographs (Figure 6-1B and C). An even layer of G4.5 dendrimers coated on the exterior surface of MSN material was clearly observed in the TEM micrographs (Figure 6-1B and 6-1C). As shown in Figure

6-2, the presence of the PAMAM dendrimers and ATP molecules in our MSN delivery system was also confirmed by the solid state CP- and DP-MAS  $^{13}\text{C}$ ,  $^{31}\text{P}$ , and  $^{29}\text{Si}$  NMR spectroscopy described in our prior reports.<sup>27, 34-37</sup>

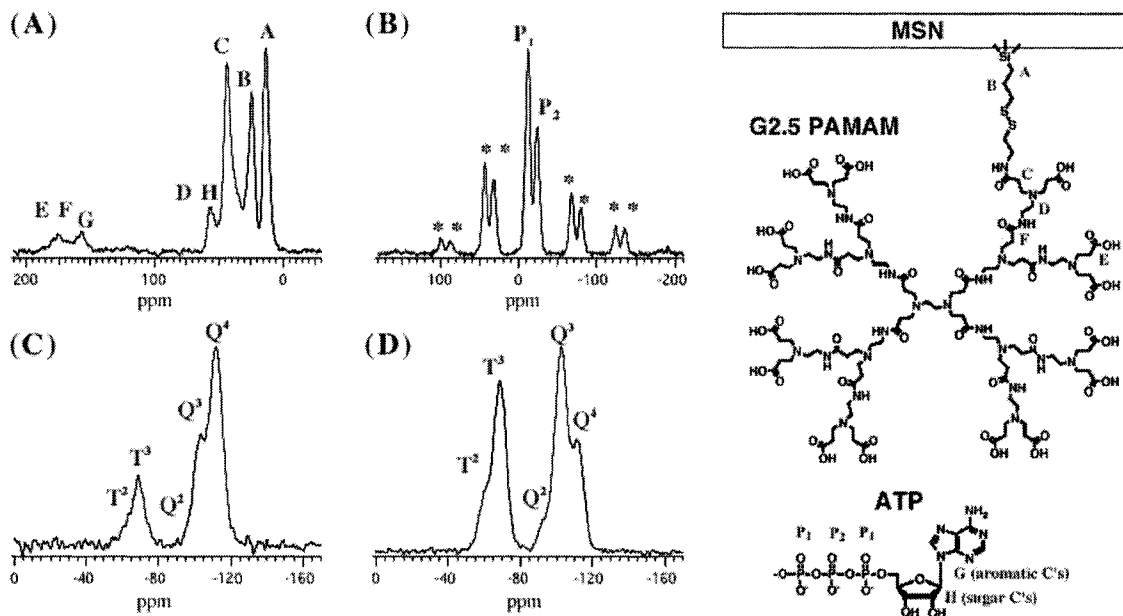


Figure 6-2. Solid state  $^{13}\text{C}$  CPMAS (A),  $^{31}\text{P}$  CPMAS (B),  $^{29}\text{Si}$  DPMAS (C), and  $^{29}\text{Si}$  CPMAS (D) spectra of ATP-loaded MSN material capped with G2.5 PAMAM dendrimers.  $^{29}\text{Si}$  CPMAS spectrum was acquired by using 1 ms contact time. \* are spinning side bands.

Chemiluminescent imaging of ATP release was chosen for the following reasons: (1) The method is extremely sensitive since luciferase has a luminescence efficiency of 0.88.<sup>38</sup> (2) The reaction kinetics of luciferase catalyzed ATP chemiluminescence are exceedingly rapid.<sup>39</sup> (3) The luciferase enzyme employed in ATP imaging measures approximately  $5.5 \times 6.5 \times 8.1$  nm in size<sup>40</sup> and therefore cannot enter the uncapped pores of the nanospheres. This ensures that any detected chemiluminescence must result from release of ATP from the MSNs. (4) There is no interference from the fluorescent MSNs.

### Compatibility of ATP imaging and the MSN-based drug delivery system

Though detection of ATP via firefly luciferase-catalyzed chemiluminescence is highly specific for ATP, experiments were conducted to ensure that the uncapping molecules did not interfere with the detection scheme. Excessive concentrations of these agents could diminish the activity of firefly luciferase.

As depicted in Figure 6-3A, the chemiluminescence from injection of a 66 nM ATP standard was four times lower for luciferase containing 500  $\mu$ M ME than for luciferase without ME. In our previous report,<sup>27</sup> 1 mM ME was employed to remove the CdS caps from their nanospheres. Thus, it was not a suitable uncapping agent for use with our detection scheme. As illustrated in Figure 6-3a, addition of 10 mM DTT to luciferase imaging solution also caused a significant reduction in chemiluminescence from injected ATP standards. In this case, however, the reduction in signal was only by a factor of 2. Previous experiments demonstrated that DTT concentrations of 0.1-10 mM were effective in uncapping the CdS-capped nanospheres.<sup>27</sup> Therefore, further experiments were conducted to determine if lower concentrations of DTT also interfered with detection of ATP. In Figure 6-3B, DTT concentrations of 20 mM, 10 mM, and 5 mM showed progressively less interference with the detection of ATP chemiluminescence. Finally, 1 mM DTT did not interfere with our detection scheme significantly. Thus, DTT was employed as the uncapping agent in our initial experiments.

Based on work by Whitesides and coworkers,<sup>31</sup> TCEP is a biocompatible disulfide bond-cleaving molecule and is widely used in cell cultures. Thus, we also examined the effect of TCEP as an uncapping trigger. As shown in Figure 6-3A, 5 mM TCEP did not cause any significant interference with the detection of injected ATP standards. Since only 100  $\mu$ M TCEP was necessary to induce significant uncapping of the nanospheres,<sup>27</sup> this compound was applicable for our experiments.

In Figure 6-3A, the control experiment (no uncapping agent present) provides a calibration curve for the detection of ATP from luciferase-catalyzed chemiluminescence. The limit of detection was calculated to be 0.5 nM ATP, and the signal was linear over three orders of magnitude (0.5-66 nM ATP;  $R^2 = 0.9997$ ).

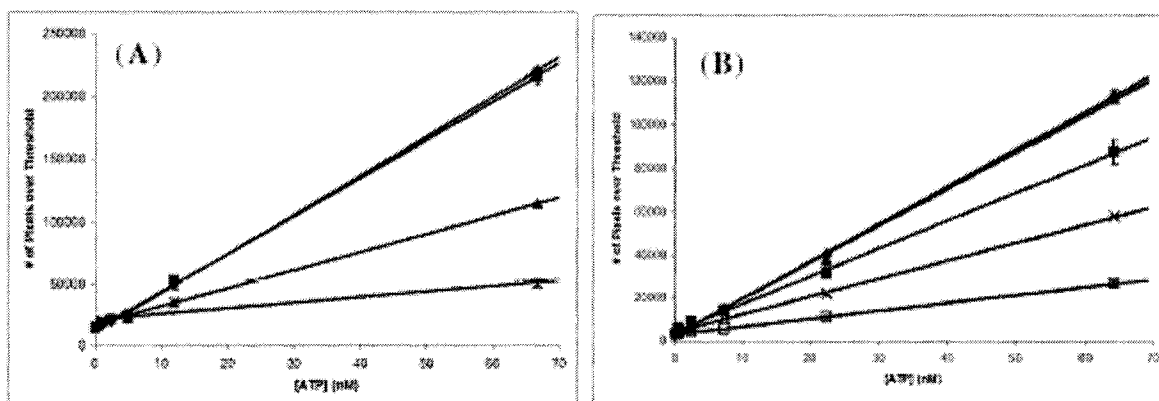


Figure 6-3. Effect of disulfide-cleaving molecules on chemiluminescence signal. Chemiluminescence signal from ATP standards was collected as detailed in the experimental section. (A) ATP standards were injected into imaging solution containing 5 mM TCEP (v), 10 mM DTT (σ), 1 mM ME (X), and imaging solution only (λ). (B) ATP standards were injected into imaging solution containing DTT concentrations of 20 mM (□), 10 mM (X), 5 mM (v), 1 mM (σ), and 0 mM (λ).

#### Detection of release of encapsulated ATP from CdS-MSN

Prior to the release experiments, the MSN particles were first thoroughly rinsed with a high ionic strength buffer to remove most of the physisorbed ATP. The nanospheres were then bathed in the imaging solution containing luciferase for 4 h, where the remaining physisorbed ATP was broken down enzymatically into ADP and inorganic phosphate. Prior to uncapping with DTT, the purified MSN generated no significant ATP release. In contrast, upon addition of 10 mM DTT, significant levels of ATP were released from the MSNs. Figure 6-4A depicts nine frames of chemiluminescence data obtained from a representative experiment. The optical image shows an aggregate of MSNs in the lower right region. The maximal ATP release was observed 129 s after stimulation, as illustrated in the signal profile in Figure 6-4B.

The magnitude of the ATP signal rose quickly in an initial burst and then quickly decreased again. The rate of signal decline slowed greatly approximately 3-4 min after stimulation, and the magnitude of release approached pre-stimulation levels 8-10 min after stimulation. As previously observed via HPLC, the majority of the ATP which is released is detected in the first hour after stimulation with DTT.<sup>27</sup> The results here suggest that in fact the majority of release occurs in the first few min after uncapping.



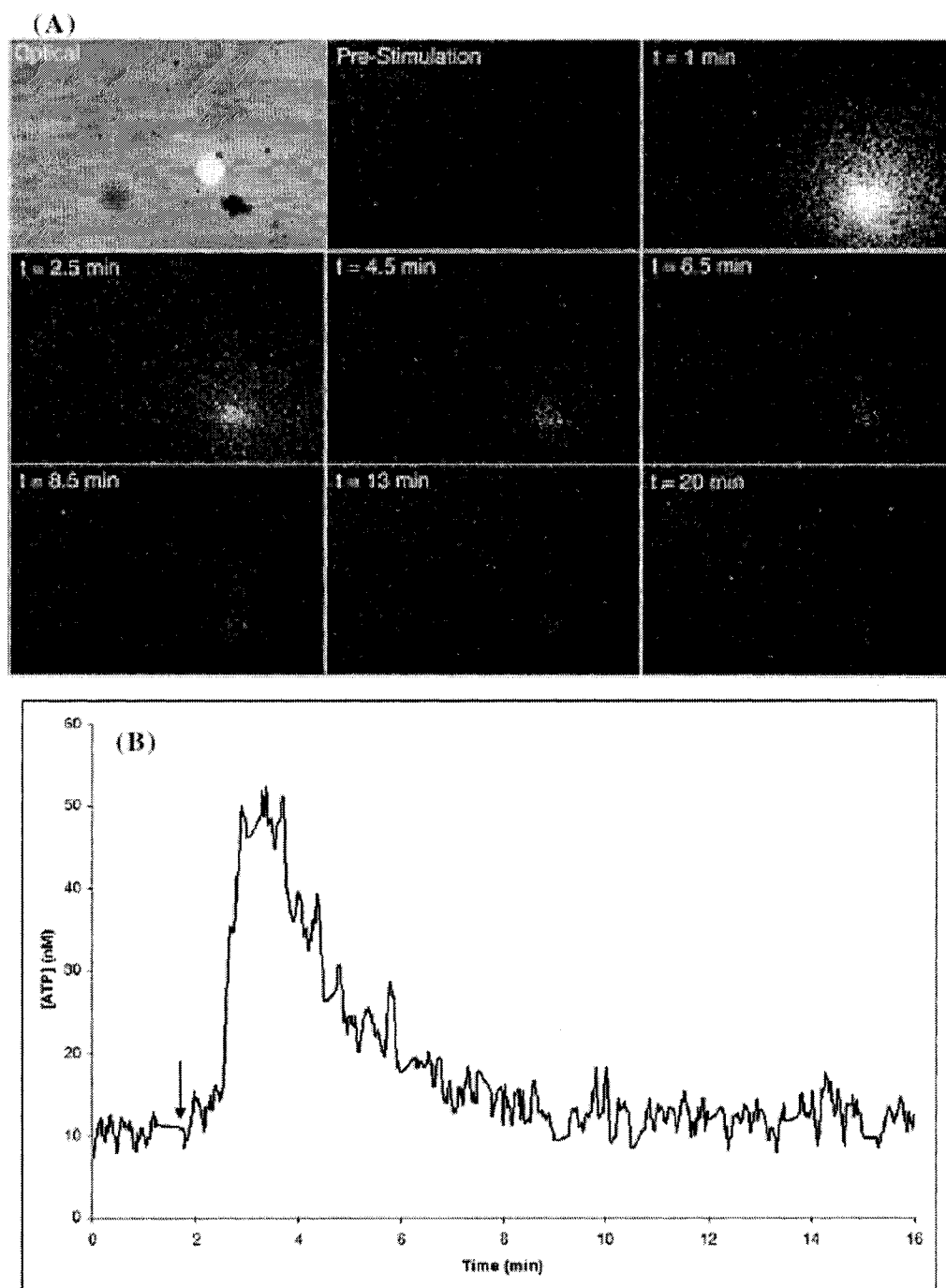


Figure 6-4. Release of encapsulated ATP from MCM-type mesoporous nanospheres. Chemiluminescence signal from ATP release was collected as detailed in the experimental section. (A) 1st frame—optical image of CdS-capped MCM-type mesoporous nanosphere aggregate. Other frames—chemiluminescence images depicting release of encapsulated ATP from the nanospheres stimulated with 5 mM DTT. (B) Time course for release of ATP from (A). Arrow indicates point of stimulation.

The initial peak in the signal likely represents release of a pool of free ATP near the opening of the pores. Additionally, the release following the initial burst (3-10 min) is likely associated with diffusion of free ATP from the center of the particle through the pores to the extracellular solution. Finally, the very low-level release detected previously over a period of days would correspond to release of physisorbed ATP from within the pores. Given that the mesopore surface was functionalized with 2-(propylsulfanyl)ethylamine groups, the electrostatic adsorption of ATP within the pores would be expected. The combined data obtained by HPLC and ATP chemiluminescence imaging describe the complete release profile for the MSNs. The results further illustrate how these two methods complement one another.

#### Comparison of uncapping of MSNs by DTT and TCEP

As TCEP was the most compatible reducing agent for use with our detection system, it was also utilized for uncapping ATP-loaded CdS-MSNs. Surprisingly, the amount of ATP released was attenuated while the temporal maximum of release was extended compared to stimulation of identical MSN material with DTT, as illustrated in Table 6-1. These results indicate that TCEP cannot cleave the disulfide bonds securing the CdS caps to the MSNs as quickly as can DTT. Several explanations can be proposed for this phenomenon. First and foremost, since the reducing power of DTT is greater than that of TCEP,<sup>31</sup> the rate of disulfide cleavage for the linkers is likely slower for TCEP than DTT. Thus the rate of CdS nanocrystal release and subsequent ATP release would be delayed. Another possible explanation of this phenomenon is the charge of TCEP. The CdS nanocrystals are derivatized with carboxylic acid moieties and are thus negatively charged across their entire surface. TCEP is also negatively charged while DTT is neutral in charge in the imaging solution. Therefore, DTT can more easily diffuse into the nanosphere structure to reach and cleave the disulfide linkers. Finally, since TCEP is larger than DTT, its diffusion through the CdS nanocrystal caps could be sterically hindered. The actual basis for the attenuated release of ATP in the case of TCEP stimulation likely is a combination of the above. Further investigation of the stimulant diffusion and reaction kinetics would be necessary to pinpoint the reason.

Table 6-1. Characteristics of release of encapsulated ATP from CdS-capped MCM-type mesoporous nanospheres for various reducing agents.

Uncapping Agent	Release Maximum (min)	Release Maximum (nM ATP)
5 mM DTT	1.8 ± 0.8	32.1 ± 9.8
5 mM TCEP	8.0 ± 2.3	4.5 ± 0.8

#### Effect of DTT concentration on release of encapsulated ATP from CdS-MSN

We examined the effect of varying the concentration of uncapping agent on the magnitude of ATP release. DTT concentrations from 5  $\mu$ M to 5 mM were added to CdS-MSNs. The 5 mM DTT was employed to ensure complete uncapping of the nanospheres, though it decreased the luminescence efficiency as demonstrated above. This was compensated for by employing the calibration curve for imaging solution containing 5 mM DTT to determine the ATP concentration. As depicted in Figure 6-5, the magnitude of ATP release varied with DTT concentration. 5 mM DTT induced release of  $32.9 \pm 1.6$  nM ATP compared to only  $8.0 \pm 2.9$  nM ATP for 5  $\mu$ M DTT.

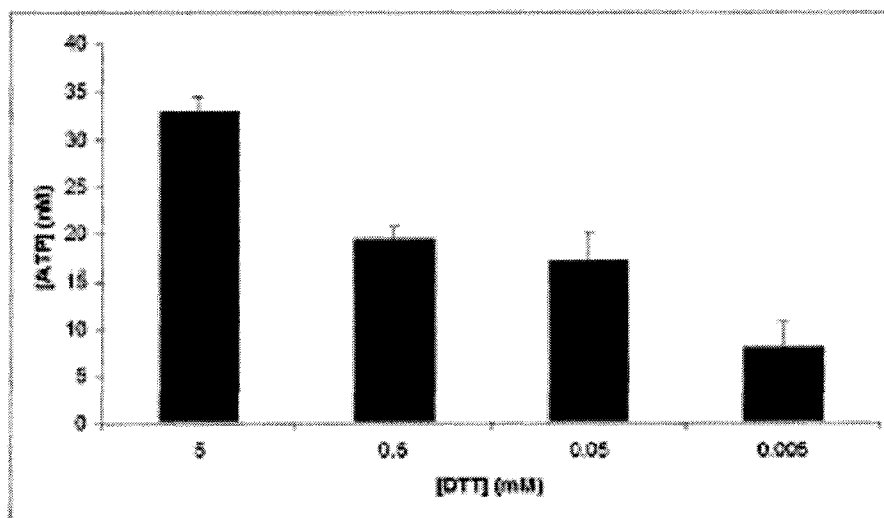


Figure 6-5. Effect of uncapping agent concentration on the magnitude of release of encapsulated ATP from MCM-type mesoporous nanospheres. Chemiluminescence signal from ATP release was collected as detailed in the experimental section.

Thus the lower concentrations of DTT were unable to completely uncap all of the MSN pores or, at least, were unable to uncap all of the pores simultaneously. These results corroborate those obtained previously with HPLC.<sup>27</sup>

#### Release of ATP from PAMAM-MSN

To investigate the influence of different capping moieties on the release kinetics, the release of ATP from MSNs capped with PAMAM dendrimers was also studied. Two types of PAMAM dendrimers (generations 2.5 and 4.5) have been successfully attached to cap the pores of the linker-functionalized MSN. When stimulated with 5 mM DTT, release of ATP was detected from both types of PAMAM-MSNs. The release profiles are displayed in Figure 6 for generation 2.5 and generation 4.5 PAMAM-MSNs. These release profiles were smoothed by averaging the release for all 50 frames of each imaging file.

Also depicted in Figure 6 is the release profile previously shown in Figure 6-4B for DTT stimulation. For comparison purposes, this profile was processed identically to those for dendrimer-MSNs. Upon stimulation with DTT, the generation 2.5 PAMAM-MSN showed no immediate release of ATP. Only after 20-30 min was a small amount of release observed from the nanospheres. This ATP release slowly increased to a maximum approximately 1.5 h after stimulation and slowly decreased back towards baseline levels. For nanospheres with generation 4.5 dendrimer caps, release occurred more quickly. ATP signal began 5 min after the addition of DTT, and maximum release was observed 11 min after stimulation. For both types of dendrimer-capped nanospheres, the maximum amount of release was smaller and the time required was longer than those of CdS-MSNs.

Apparently, the PAMAM dendrimer caps are more flexible than the CdS nanocrystal caps. After forming one link to the nanosphere, it is possible that a dendrimer can flex slightly and form additional bonds to the opening of the MSN pore. The CdS nanocrystals, on other hand, are solid particles and perhaps lack flexibility and therefore may form fewer bonds to the nanosphere. Hence, in the case of PAMAM-MSN, more disulfide bonds would need to be broken in order to release the dendrimer caps upon stimulation. Additionally, with more bonds formed, the dendrimer caps would be held tighter to the nanosphere allowing less

room for the reducing agents to diffuse into the pores to reach the disulfide linkers. In fact, the generation 2.5 PAMAM is smaller in size than the 2.3 nm diameter pores of the MSN.

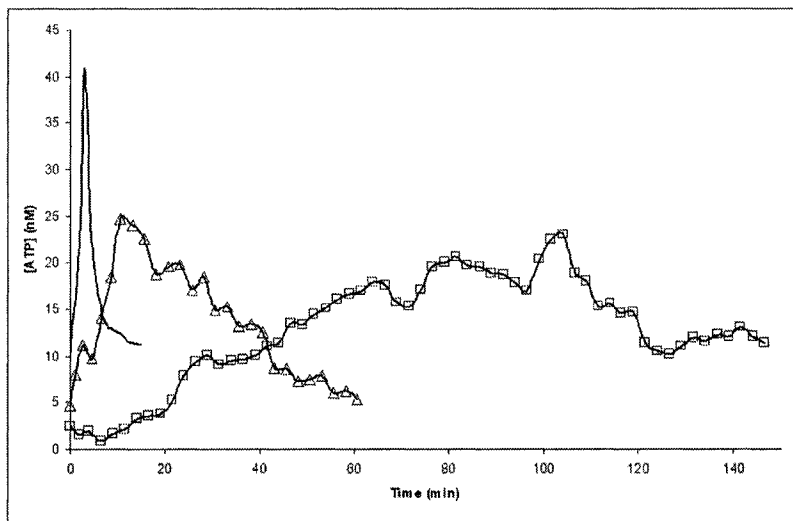


Figure 6-6. Release of encapsulated ATP from dendrimer-capped MCM-41-type mesoporous nanospheres. Chemiluminescence signal from ATP release was collected as detailed in the experimental section. Plots depict release stimulated with 5 mM DTT at time = 2 min for generation 2.5 PAMAM dendrimer-capped particles ( $\square$ ), generation 4.5 PAMAM dendrimer-capped particles ( $\triangle$ ) and CdS nanocrystal-capped particles (solid line).

Therefore, these dendrimers could diffuse into and bind inside the pores. Thus, each pore could be bound by more than one generation 2.5 dendrimer capping molecule. This would decrease the rate of capped ATP release significantly, as was observed in our experiments. Upon further examination of Figure 6-6, it appears that the total released ATP from the PAMAM-MSN is actually greater than that of the CdS-MSN. As observed via TEM images in an earlier report,<sup>27</sup> the capping efficiency for CdS nanocrystals is only 57%. In contrast, the dendrimer-capped particles have a capping efficiency of nearly 100%. This indicates that though the nanospheres were loaded with the same concentration of ATP, the dendrimer-capped particles contain more ATP than the CdS-capped particles. Thus, more ATP is present to be released upon introduction of DTT.

## Conclusions

Real-time imaging of ATP release via luciferase-catalyzed chemiluminescence is a highly sensitive and selective method. We applied this imaging technique to the study of ATP release from mesoporous silica nanospheres end-capped with CdS nanocrystals and PAMAM dendrimers. The kinetics revealed a pulse-type release from CdS-capped particles upon uncapping. In contrast, the dendrimer-capped nanospheres exhibited release of ATP in a more gradual and plateau-like profile. Understanding the release mechanisms and release kinetics of these systems will aid in the development of more advanced particle designs. By varying the capping molecules as well as the uncapping triggers, we envision that the release profile of a drug of interest can be fine-tuned depending on whether a high concentration, one-time drug release or a lower level, continuous drug release treatment is desired.

## Acknowledgments

The authors would like to thank Dr. M. Pruski and Dr. J. W. Wiench for their help in solid state NMR measurements, and Brian G. Trewyn for assistance in sample preparation and helpful discussions. V.S.-Y. L. thanks NSF (CHE-0239570) for support. E.S.Y. thanks the Robert Allen Wright Endowment for Excellence for support. The Ames Laboratory is operated for the U.S. Department of Energy by Iowa State University under Contract No. W-7405-Eng-82. This work was supported by the Director of Science, Office of Basic Energy Sciences, Division of Chemical Sciences.

## References

1. Wilson, M.; Kannangara, K.; Smith, G.; Simmons, M.; Raguse, B. *Nanotechnology: Basic Science and Emerging Technologies*; Chapman and Hall/CRC: Boca Raton, FL, 2002.

2. Macucci, M.; Iannaccone, G.; Greer, J.; Martorell, J.; Sprung, D. W. L.; Schenk, A.; Yakimenko, I. I.; Berggren, K.-F.; Stokbro, K.; Gippius, N. *Nanotechnology* **2001**, *12*, 136.
3. Dai, L. In *Perspectives of Fullerene Nanotechnology*; Osawa, E., Ed.; Kluwer Academic Publishers: Dordrecht, Netherlands, 2002.
4. Allan, G.; Delerue, C.; Krzeminski, C.; Lannoo, M. In *Nanostructured Materials*; Knauth, P., Schoonman, J., Eds.; Kluwer Academic Publishers: Norwell, MA, 2002, 161.
5. Krenn, J. R. *Nature Mater.* **2003**, *2*, 210.
6. Cullum, B. M.; Vo-Dinh, T. *Biomedical Photonics Handwork*; CRC Press LLC: Boca Raton, FL, 2003.
7. Lin, V. S. Y.; Lai, C.-Y.; Huang, J.; Song, S.-A.; Xu, S. *J. Am. Chem. Soc.* **2001**, *123*, 11510.
8. Livage, J.; Coradin, T.; Roux, C. *J. Phys.: Condensed Matter* **2001**, *13*, R673.
9. Uhrich, K. E.; Cannizzaro, S. M.; Langer, R. S.; Shakesheff, K. M. *Chem. Rev. (Washington, D. C.)* **1999**, *99*, 3181.
10. Langer, R. *Acc. Chem. Res.* **1993**, *26*, 537.
11. Li, Y.; Kissel, T. *J. Controlled Release* **1993**, *27*, 247.
12. Peppas, N. A.; Huang, Y.; Torres-Lugo, M.; Ward, J. H.; Zhang, J. *Annu. Rev. Biomed. Eng.* **2000**, *2*, 9.
13. Kost, J.; Langer, R. *Adv. Drug Delivery Rev.* **2001**, *46*, 125.
14. Ishihara, K.; Kobayashi, M.; Ishimaru, N.; Shonohara, I. *Polym. J.* **1984**, *16*, 625.
15. Fischel-Ghodsian, F.; Brown, L.; Mathiowitz, E.; Brandenburg, D.; Langer, R. *Proc. Natl. Acad. Sci. U.S.A.* **1988**, *85*, 2403.
16. Stein, A.; Melde, B. J.; Schroden, R. C. *Adv. Mater. (Weinheim, Germany)* **2000**, *12*, 1403.
17. Sayari, A.; Hamoudi, S. *Chem. Mater.* **2001**, *13*, 3151.
18. Vallet-Regi, M.; Ramila, A.; del Real, R. P.; Perez-Pariente, J. *Chem. Mater.* **2001**, *13*, 308.

19. Munoz, B.; Ramila, A.; Perez-Pariente, J.; Diaz, I.; Vallet-Regi, M. *Chem. Mater.* **2003**, *15*, 500.
20. Ramila, A.; Munoz, B.; Perez-Pariente, J.; Vallet-Regi, M. *J. Sol.-Gel Sci. Technol.* **2003**, *26*, 1199.
21. Mal, N. K.; Fujiwara, M.; Tanaka, Y.; Taguchi, T.; Matsukata, M. *Chem. Mater.* **2003**, *15*, 3385.
22. Diaz, J. F.; Balkus, K. J., Jr. *J. Mol. Catal. B: Enzymatic* **1996**, *2*, 115.
23. Han, Y.-J.; Stucky, G. D.; Butler, A. J. *Am. Chem. Soc.* **1999**, *121*, 9897.
24. Kisler, J. M.; Stevens, G. W.; O'Connor, A. J. *Mater. Phys. Mech.* **2001**, *4*, 89.
25. Yiu, H. H. P.; Wright, P. A.; Botting, N. P. *Microporous Mesoporous Mater.* **2001**, *44-45*, 763.
26. Takahashi, H.; Li, B.; Sasaki, T.; Miyazaki, C.; Kajino, T.; Inagaki, S. *Microporous Mesoporous Mater.* **2001**, *44-45*, 755.
27. Lai, C.-Y.; Trewyn, B. G.; Jeftinija, D. M.; Jeftinija, K.; Xu, S.; Jeftinija, S.; Lin, V. S. Y. *J. Am. Chem. Soc.* **2003**, *125*, 4451.
28. Tomalia, D. A.; Baker, H.; Dewald, J.; Hall, M.; Kallos, G.; Martin, S.; Roeck, J.; Ryder, J.; Smith, P. *Macromolecules* **1986**, *19*, 2466.
29. Roberts, J. C.; Bhalgat, M. K.; Zera, R. T. *J. Biomed. Mater. Res.* **1996**, *30*, 53.
30. Tang, M.; Redemann, C. T.; Szoka, F. C., Jr. *Bioconjugate Chem.* **1996**, *7*, 703.
31. Burns, J. A.; Butler, J. C.; Moran, J.; Whitesides, G. M. *J. Org. Chem.* **1991**, *56*, 2648.
32. Gould, S. J.; Subramani, S. *Anal. Biochem.* **1988**, *175*, 5.
33. Wang, Z.; Haydon, P. G.; Yeung, E. S. *Anal. Chem.* **2000**, *72*, 2001.
34. Huh, S.; Chen, H.-T.; Wiench, J. W.; Pruski, M.; Lin, V. S. Y. *J. Am. Chem. Soc.* **2004**, *126*, 1010.
35. Huh, S.; Wiench, J. W.; Trewyn, B. G.; Song, S.; Pruski, M.; Lin, V. S. Y. *Chem. Commun. (Cambridge)* **2003**, 2364.
36. Huh, S.; Wiench, J. W.; Yoo, J.-C.; Pruski, M.; Lin, V. S. Y. *Chem. Mater.* **2003**, *15*, 4247.



37. Radu, D. R.; Lai, C.-Y.; Wiench, J. W.; Pruski, M.; Lin, V. S. Y. *J. Am. Chem. Soc.* **2004**, *126*, 1640.
38. Chiu, N. H. L.; Christopoulos, T. K. *Clin. Chem.* **1999**, *45*, 1954.
39. McElroy, W. D.; DeLuca, M. *Bioluminescence and Chemiluminescence: Basic Chemistry and Analytical Applications*; Academic Press: New York, 1981.
40. Conti, E.; Franks, N. P.; Brick, P. *Structure* **1996**, *4*, 287.

Chapter 7. A Polyamidoamine Dendrimer-capped Mesoporous Silica Nanosphere-based  
Gene Transfection Reagent

The paper was published in *The Journal of American Chemical Society*

*J. Am. Chem. Soc.* **2004**; *126(41)*, 13216-13217.

Radu, D. R.; **Lai, C.-Y.**; Jeftinija, K.; Rowe, E. W.; Jeftinija, S.; Lin, V. S.-Y.

Department of Chemistry and Department of Biomedical Science, Iowa State University,  
Ames, Iowa 50011-3111

### Abstract

We synthesized a MCM-41 type mesoporous silica nanosphere (MSN) based gene transfection system, where second generation (G2) PAMAMs were covalently attached to the surface of MSN. The G2-PAMAM-capped MSN material (G2-MSN) was used to complex with a plasmid DNA (pEGFP-C1) that is encoding for an enhanced green fluorescence protein. The gene transfection efficacy, uptake mechanism, and biocompatibility of the G2-MSN system with various cell types, such as neural glia (astrocytes), human cervical cancer (HeLa), and Chinese hamster ovarian (CHO) cells were investigated.

### Introduction

Recent reports in the literature have demonstrated that polyamidoamine (PAMAM) dendrimers can serve as non-viral gene transfection reagents.<sup>1</sup> However, only those PAMAMs of high generations ( $G > 5$ ) have been shown to be efficient in gene transfection.<sup>1a</sup> The required procedures for the synthesis and purification of these high G PAMAMs are usually tedious and low-yield. In contrast, the low G PAMAMs ( $G < 3$ ) are nontoxic and easy to be synthesized. Despite the benefits, the smaller molecular sizes and the limited surface charges of the low G PAMAMs prohibit efficient complexation with plasmid DNAs in solution due to the entropy penalty.<sup>1a</sup> Herein, we report a novel gene transfection system,

where second generation (G2) PAMAMs were covalently attached to the surface of a MCM-41 type mesoporous silica nanosphere (MSN)<sup>2</sup> material as depicted in Figure 7-1.

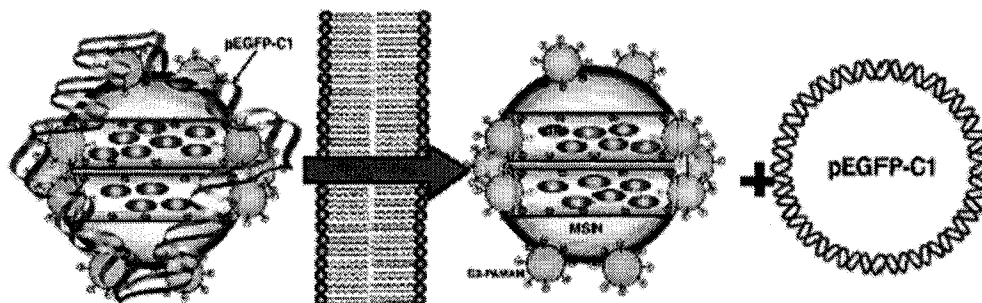


Figure 7-1. Schematic representation of a non-viral gene transfection.

## Materials and Methods

### Experimental Section

#### Synthesis of ICP-MSN

*N*-Cetyltrimethylammonium bromide (CTAB, 1.00 g, 2.74 mmol) was dissolved in 480 mL of nanopure water. Sodium hydroxide aqueous solution (2.00 M, 3.50 mL) was introduced to the CTAB solution and the temperature of the mixture was adjusted to 353 K. Tetraethoxysilane (TEOS, 5.00 mL, 22.4 mmol) was added dropwise to the surfactant solution under vigorous stirring. The mixture was allowed to react for 2 h to give rise to a white precipitate. This solid crude product was filtered, washed with deionized water and methanol, and dried in air to yield the as-synthesized MSN. To remove the surfactant template (CTAB), 1.50 g of the as-synthesized MSN was refluxed for 24 h in a methanolic solution of 9.00 mL of HCl (37.4%) in 160.00 mL methanol. The resulting material was filtered and extensively washed with deionized water and methanol. The surfactant-free MSN material was placed under high vacuum to remove the remaining solvent from the mesopores. MSN (1.00 g) was refluxed for 20 h in 80.00 mL of anhydrous toluene with 0.25 mL (1.00 mmol) of 3-isocyanatopropyltriethoxysilane to yield the 3-isocyanatopropyl-functionalized MSN (ICP-MSN) material.

### Synthesis of G2-MSN without Texas Red

The purified ICP-MSN (0.15 g) was added to anhydrous ethanol (3.00 mL). A second-generation (G2) polyamidoamine dendrimer (PAMAM, 2.00 mL, 0.11 mmol) was then added to the ICP-MSN ethanol solution. The amino groups of the G2-PAMAM were allowed to react with the ICP functional groups present on the surface of MSN for 20 h at room temperature to yield the G2-PAMAM-capped MSN material (G2-MSN). The resulting G2-MSN material was filtered and washed thoroughly with ethanol, methanol and acetone and dried under high vacuum.

### Synthesis of Texas Red-loaded G2-MSN

The purified ICP-MSN (0.15 g) was added to an anhydrous ethanol solution (3.00 mL) of Texas Red™ (5.00 mM, Molecular Probe). The solution mixture was stirred at room temperature for 20 h to allow the Texas Red to be encapsulated by the ICP-MSN. A second-generation (G2) polyamidoamine dendrimer (PAMAM, 2.00 mL, 0.11 mmol) was then added to the ICP-MSN/Texas Red solution. The amino groups of the G2-PAMAM were allowed to react with the ICP functional groups present on the surface of MSN for 20 h at room temperature to yield the Texas Red-loaded, G2-PAMAM-capped MSN material (Texas Red-loaded G2-MSN). The resulting G2-MSN material was filtered and washed thoroughly with ethanol, methanol and acetone and dried under high vacuum. To ensure the complete removal of Texas Red molecules physisorbed on the exterior surface of the G2-MSN, a Soxhlet extraction in ethanol was performed for 20 h. The resulting solid was filtered and dried in air.

### Characterization of ICP-MSN and G2-MSN

#### Powder X-Ray Diffraction

Powder XRD experiments were performed on a Scintag XDS 2000 diffractometer using a Cu K $\alpha$  radiation source. Low angle diffraction with a  $2\theta$  range of 1 to 10° was used to investigate the long-range order of the materials.

### Nitrogen adsorption/desorption isotherms

The surface area and median pore diameter were measured using N<sub>2</sub> adsorption/desorption measurements in a Micromeritics ASAP 2000 BET surface analyzer system. The data were evaluated using the Brunauer-Emmett-Teller (BET) and Barrett-Joyner-Halenda (BJH) methods to calculate the surface area and pore volumes/pore size distributions, respectively. Samples were prepared by degassing at 90 °C for 1 h and then at 150 °C for 4 h.

### Solid-state <sup>13</sup>C CP-MAS NMR

Solid-state <sup>13</sup>C CP-MAS NMR spectra were obtained at 75.47 MHz on a Bruker MSL300 spectrometer equipped with Bruker 4mm rotor MAS probe. Magic-angle sample spinning rate was maintained at 10 KHz for <sup>13</sup>C in order to minimize the spin band due to the high anisotropic chemical shifts of aromatic carbons. The NMR spectra consisted of 5,000 to 20,000 acquisitions with cross polarization times of 3 ms (<sup>13</sup>C) and pulse repetition times of 15 s (<sup>13</sup>C). All chemical shifts reported are referenced to liquid Me<sub>4</sub>Si (TMS).

### Scanning and Transmission Electron Micrographs (SEM and TEM) of G2-MSN

Particle morphology of these materials was determined by scanning electron microscopy (SEM) with 10 kV accelerating voltage and 0.005 nA of beam current for imaging. For transmission electron microscopy (TEM) studies, a small aliquot was taken from a suspension of methanol and placed in a lacey carbon-coated TEM grid, which was pulled through the suspension and allowed to dry in air. Thin sections of samples embedded in epoxy resin were obtained with ultramicrotomy (60-80 nm). The resulting sample was examined with a Philips model CM-30 TEM operated at 300 kV. The specimen was given no further treatment, as it appeared stable under beam bombardment.

### Gene Transfection Experiments of DNA-coated G2-MSNs

Human cervical cancer (HeLa) and Chinese Hamster Ovarian (CHO) cell lines were obtained from American Tissue Culture Collection (ATCC). HeLa and CHO cells were maintained in T75 flasks using DMEM (Dulbecco's modified Eagle's medium)

supplemented with 10% CS serum, 2 mM L-glutamine, 100 U/mL penicillin, 100  $\mu\text{g}/\mu\text{L}$  streptomycin, and 1  $\mu\text{g}/\mu\text{L}$  gentamycin. All cells were passaged every 2-3 days. A red-shifted variant of GFP expressed from pEGFP-C1 (Clontech, Palo Alto, CA) was used as reporter protein. All plasmids were amplified in the *E. coli* strain DH5 $\alpha$  and purified according to the manufacturer's protocol (Qiagen, USA). The isolated DNA was resuspended in Tris-EDTA (pH 8.0) at a concentration of 1  $\mu\text{g}/\mu\text{L}$ .

HeLa cells were first seeded onto 24-well plates ( $6 \times 10^4$  cells per well, in 0.6 mL growth medium) and 6-well plates ( $2 \times 10^5$  cells per well, in 1.5 mL growth medium) 24 h prior to the experiment. The former plating (24-well) was used for transfection efficiency measurements. The 6-well plating was used for imaging studies.

In a typical transfection experiment, 1  $\mu\text{g}$  of plasmid DNA encoding GFP was added to 10  $\mu\text{g}$  of G2-MSN suspension obtained by dispersing the nanosphere material in 30  $\mu\text{L}$  of HEPES buffer solution (10 mM HEPES, pH 7.4). The complex mixture was incubated for 2 h at 4  $^{\circ}\text{C}$ . A solution of 30  $\mu\text{L}$  of 100 mM  $\text{CaCl}_2(\text{aq})$  was added to the G2-MSN-DNA complex solution and allowed to incubate for another 2 h. The 50 mM  $\text{Ca}^{2+}$  was to enhance/stabilize the complexation between DNA and G2-MSN and protect the surface-bound DNA from enzymatic degradation as described in recent literature. The entire 60  $\mu\text{L}$  of the G2-MSN-DNA suspension was added to cells cultured on 24-well plates. Given that each well contained 0.6 mL DMEM, the addition of the suspension resulted in a final  $\text{Ca}^{2+}$  concentration of 4.5 mM. After incubation for 4 hours at 37  $^{\circ}\text{C}$ , the transfection mixture containing residual G2-MSN-DNA complexes was removed by washing the transfected cells with PBS buffer and cultured with DMEM supplemented with 10% calf serum (CS) and antibiotics. The cultures were maintained for 2 days to monitor gene expression. The transfected cells were then washed with PBS buffer and cultured with DMEM + 10% calf serum (CS) medium and antibiotics for 2 days for gene expression analysis or image studies. To compare the transfection efficiency of our G2-MSN system with other commercially available transfection reagents, three different reagents, PolyFect<sup>®</sup>, SuperFect<sup>®</sup> (Qiagen, Valencia, California) and Metafectene<sup>®</sup> (Biontix, Germany), were used to transfect the aforementioned cell types under the same experimental condition. First, 8 and 5  $\mu\text{L}$  of the stock solutions of PolyFect<sup>®</sup> (2 mg/mL) and SuperFect<sup>®</sup> (3 mg/mL), respectively, were

added to a 30  $\mu\text{L}$  of serum-free medium (DMEM) containing 1  $\mu\text{g}$  DNA. The solutions were incubated at room temperature for 15 min to allow the formation of stable complexes between DNA molecules and transfection reagents. The complexes were then added to a culture of HeLa cells in a 24 well plate with a cell density of  $6 \times 10^4$  cells/well that contained 350  $\mu\text{l}$  of pre-warmed DMEM + 10% CS medium and antibiotics. After 4 h of incubation, the transfection medium was discarded and replaced with fresh growth medium (DMEM + 10% CS medium and antibiotics). The cells were evaluated for expression of the enhanced green fluorescent protein (EGFP) by flow cytometry after 48 h post-transfection.

For Metafectene<sup>®</sup>, the protocol involved the addition of 5  $\mu\text{L}$  stock solution of Metafectene<sup>®</sup> (1mL stock solution was used as received from Biontex, Germany) to a 30  $\mu\text{L}$  of serum-free medium (DMEM) containing 1  $\mu\text{g}$  DNA. This solution was incubated at room temperature for 15 min to allow complex formation before the addition to the cells. The complexes were added to the aforementioned HeLa cell wells that contained 350  $\mu\text{L}$  of pre-warmed, serum-free DMEM. After 4 h of incubation, the transfection medium was discarded and replaced with fresh growth medium (DMEM + 10% CS medium and antibiotics). Cells were evaluated for expression of the enhanced green fluorescent protein (EGFP) by flow cytometry after 48 h post-transfection.

#### Stability Studies of pEGFP-C1 DNA and G2-MSN-DNA Complex after Bam H1 treatment

DNA was released from the G2-MSN particles by vigorous agitation in 2 M NaCl at 50 °C for 30 min. The supernatant was collected by micro-centrifugation at 14000 rpm at 4 °C for 15 min. After ethanolic precipitation, the DNA was resuspended in TE buffer and loaded in the gel.

#### Flow Cytometric Analysis of Transfection Efficiencies of G2-MSN and Other Reagents

Flow cytometric measurements were performed immediately after collection of cultured cells. All cells were trypsinized and resuspended in 0.5 mL of PBS before the FACS analysis. Positive and negative control experiments utilizing cultures of untransfected cells (HeLa cells only) and “mock”-transfected cells (cells incubated with MSNs without pEGFP-C1 plasmid) were measured with an EPICS-ALTRA flow cytometer (Beckman

Coulter, Miami, FL), using a 488 nm laser for GFP excitation. GFP fluorescence was detected using PMT2 in conjunction with a 525 nm band-pass filter. An electronic gate was set around cells based on the forward and side scatter properties of the population, and a minimum of 10,000 gated events per sample were collected and stored in list mode files. Data analysis was performed with FlowJo software (Tree Star, Ashland, OR). Scatter-gated events are displayed herein as single parameter histograms of logarithmic GFP fluorescence. All experiments were performed in quadruplicate. Untransfected cells were used for background calibration. The average transfection efficiencies of different transfection reagent systems on HeLa cells were summarized in Table 7-3.

#### Confocal Microscopy Imaging of Transfected Cells

HeLa cells were grown on coverslips in a 6-well culture plate. All of the samples were washed three times with PBS buffer and fixed with formaldehyde in PBS (3.7 %). The samples were excited by an argon laser ( $\lambda_{\text{ex}} = 488 \text{ nm}$ ) and the images were subject to a longpass filter ( $\lambda = 515 \text{ nm}$ ). Images were captured on an inverted Nikon Eclipse microscope connected to a Prairie Technologies (Middleton, WI) Scanning Laser Confocal Microscope controlled by Prairie Technologies software. Images were analyzed using Metamorph software (Universal Imaging, West Chester, PA).

#### Transmission Electron Micrographs of G2-MSN transfected Cells

To study the endocytosis of G2-MSN-DNA complexes, post-transfection cells on coverslips were fixed at selected time-points with 2% glutaraldehyde and 2% paraformaldehyde in PBS buffer, pH 7.2, at 4°C for 48 h. The samples were then washed in PBS followed by washing in 0.1M cacodylate buffer, pH 7.2, and post-fixed in 1% osmium tetroxide in 0.1M cacodylate buffer for 1 hour at room temperature. The samples were then washed briefly in dH<sub>2</sub>O and dehydrated through a graded ethanol series and cleared using ultra pure acetone and infiltrated and embedded with EPON epoxy resin (EmBed 812, Electron Microscopy Sciences, Ft. Washington, PA). Coverslips were embedded by inverting the slips (cell side down) onto upright beam capsules and polymerized at 60°C for 24 hours and 70°C for 24 h. The coverslips were removed from the resin with liquid nitrogen. Thin



sections were made using a Reichert Ultracut S ultramicrotome (Leica, Deerfield, IL) and collected onto copper grids and stained with 4% uranyl acetate in 50% methanol followed by Sato's lead stain. Images were collected using a JEOL 1200 EXII scanning and transmission electron microscope (Japan Electron Optics Laboratory, Peabody, MA.) at 80kV with a Megaview III digital camera and SIS Pro software (Soft Imaging System, Corp., Lakewood, CO).

### Cell Growth Studies

To further demonstrate the *in vitro* biocompatibility of the G2-MSN, growth studies were performed for HeLa and CHO cells. Two series of experiments were designed for both types of cells: one series studied the natural cells growth (without MSNs) and the other was monitored after MSNs application. All experiments were performed in triplicate. To ensure enough space and media for cell growing, the cells were seeded in T-25 flasks. In the experiments without MSNs, 18 flasks were loaded with the same amount of cells for each cell type. After allowing 24 h for cell adhesion, the cells were analyzed everyday (3 flasks per day) for 6 days. The cells were trypsinized and counted by using a Guava ViaCount® assay (Guava Technologies, Inc, USA). In the experiments with G2-MSNs, the cells were seeded for 24 h prior to the incubation with MSNs at 0.1mg/mL concentration in DMEM + 10% CS (calf serum) and antibiotics for 4 h. After the 4 h incubation, the cells were washed twice with PBS buffer and incubated for another 6 days. The aforementioned cell counting procedures were followed. All experiments were performed in triplicate (3 flasks /day). During the 6-day growth period, the cells were periodically examined under a phase contrast microscope. The cells were added with fresh media every other day or upon pH fluctuations (Phenol Red dye was used as pH indicator). The doubling times of the cell density of HeLa cells without and with MSNs were calculated from the semilog plots to be 20 h and 24 h, respectively. The doubling times of CHO cells without and with MSNs were calculated to be 21 h and 24 h, respectively. ( $R^2 \geq 97\%$  in the case of HeLa cells, whereas  $R^2 \geq 97.6\%$  for CHO cells)

## Results and Discussion

The G2-PAMAM-capped MSN material (G2-MSN) was used to complex with a plasmid DNA (pEGFP-C1) that codes for an enhanced green fluorescence protein.<sup>3</sup> We have investigated the gene transfection efficacy, uptake mechanism, and biocompatibility of the G2-MSN with neural glia (astrocytes), human cervical cancer (HeLa), and Chinese hamster ovarian (CHO) cells.

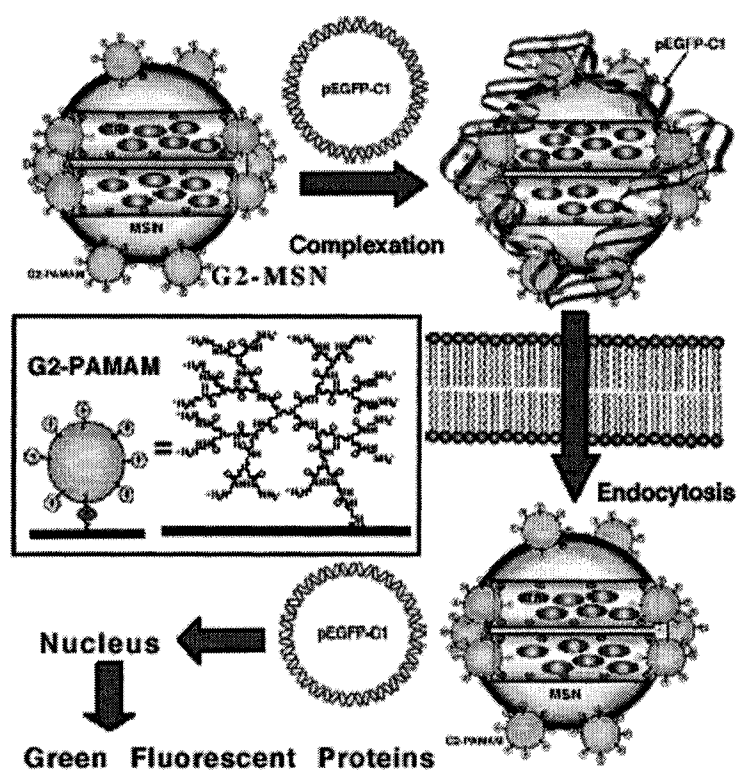


Figure 7-2. Schematic representation of a non-viral gene transfection system based on a Texas Red (TR)-loaded, G2-PAMAM dendrimercapped MSN material complexed with an enhanced green fluorescence protein (*Aequorea victoria*) plasmid DNA (pEGFP-C1).

In contrast to other recently reported silica nanoparticle-based gene transfer systems,<sup>4</sup> the mesoporous structure of the MSN allows membrane impermeable molecules, such as pharmaceutical drugs and fluorescent dyes, to be encapsulated inside the MSN channels.<sup>2,5</sup>

The system renders the possibility to serve as a universal transmembrane carrier for intracellular drug delivery and imaging applications. To the best of our knowledge, no uptake study of MCM-41 type mesoporous silicas into eukaryotic cells have been reported before. To construct the G2-MSN gene transfer system, a MSN material with an average particle size of 250 nm (avg. pore diameter = 2.7 nm) was synthesized via our previously reported method.<sup>2</sup> 3-Isocyanatopropyltriethoxysilane (0.25mL, 1 mmol) was grafted onto the pore surface of the MSN (1 g) in 80 mL of toluene for 20 h to yield the isocyanatopropyl-functionalized MSN (ICP-MSN) material. To visualize the interaction of MSNs and cells, we prepared a G2-MSN material loaded with a fluorescent dye (Texas Red™). ICP-MSN (0.15 g) was added to an anhydrous ethanol solution of Texas Red™ (5mM), and stirred for 20 h. The amine-terminated G2-PAMAMs were used as caps to encapsulate Texas Red molecules inside the porous channels of ICP-MSN. An ethanol solution of G2-PAMAM (0.11 mmol) was added to the MSN/Texas Red solution for 20 h to form urea linkage between amines of PAMAM and ICP groups of MSN (Figure 7-1,2 inset). The structure of G2-PAMAM-capped, Texas Red-encapsulated MSN were scrutinized by XRD, SEM, TEM, N<sub>2</sub> sorption isotherms, and <sup>13</sup>C CP-MAS NMR spectroscopy and also summarized in the following (Figure 7-3 to 5)<sup>6</sup>

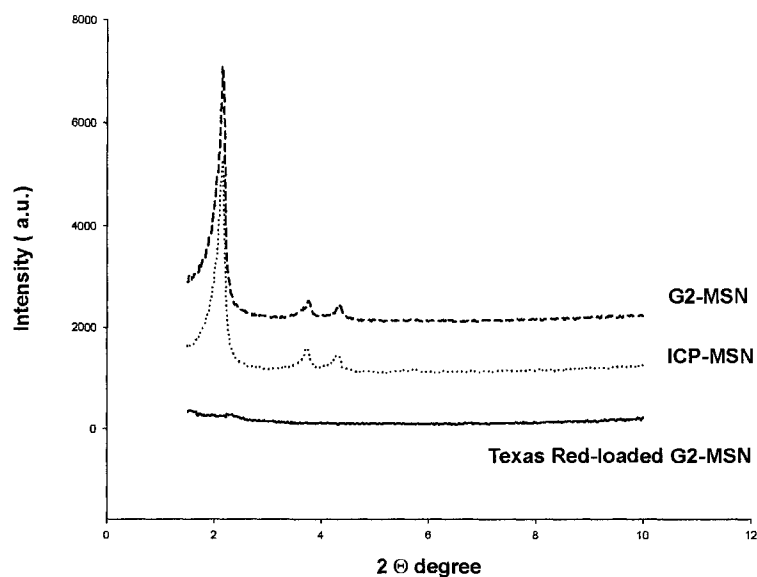


Figure 7-3. Powder X-Ray diffraction patterns of purified ICP-MSN, G2-MSN, and Texas Red-loaded G2-MSN materials. Both ICP-MSN and G2-MSN materials exhibit the typical diffraction patterns of MCM-41 type mesoporous silica with hexagonal symmetry. The changes in the Tex Red-loaded G2-MSN diffraction pattern might be caused by pore filling effect.

Table 7-1. Powder X-Ray diffraction patterns

Sample	Powder XRD Diffraction		
	$d_{100}$ (Å)	$d_{110}$ (Å)	$d_{200}$ (Å)
ICP-MSN	40.88	23.61	21.05
G2-MSN	40.88	23.48	21.05
Tex Red-loaded G2-MSN	39.41	--	--

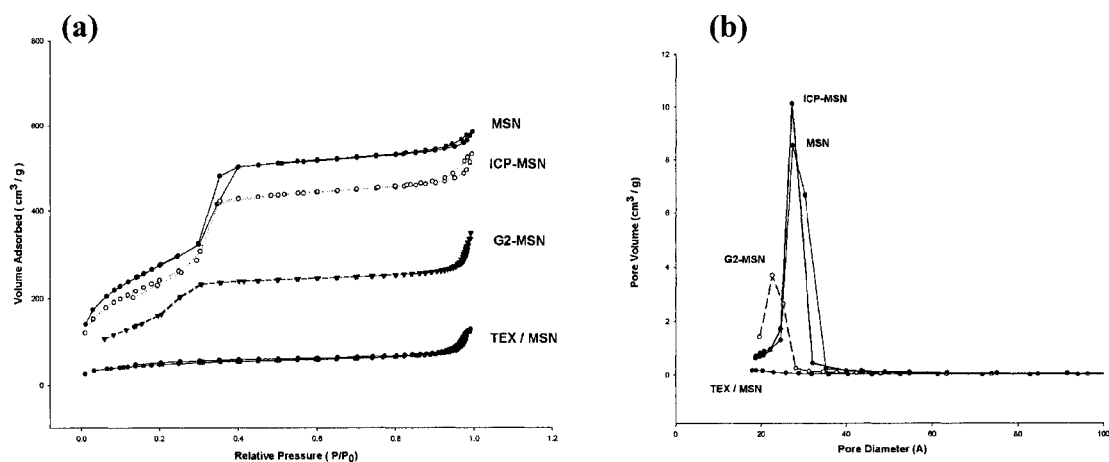


Figure 7-4. BET nitrogen adsorption/desorption isotherms (a) and BJH pore size distributions (b) of MSN, ICP-MSN, G2-MSN, and Texas Red-loaded G2-MSN materials. The BET isotherms of ICP-MSN and G2-MSN materials didn't exhibit any hysteresis indicated that there was no xerogel formation on the exterior surface of the MSN upon surface functionalization.

To study the complexation between the pEGFP-C1 DNA and G2-MSN in different weight ratios at physiological pH, agarose gel electrophoresis (0.8%, 45 mM TBE buffer) of pEGFP-C1 in the presence of G2-MSNs was performed for 3.5 h at 155 V. Figure 7-7a shows the electrophoretic shifts for pEGFP-C1 in the absence (lane 2) of G2-MSN and presence of increasing amounts (lane 3-8) of G2-MSN. The results demonstrated that the G2-MSN could bind with plasmid DNA to form stable DNA-MSN 1:5, as illustrated by the retention of pEGFP-C1 around the sample wells (lane 6-8).

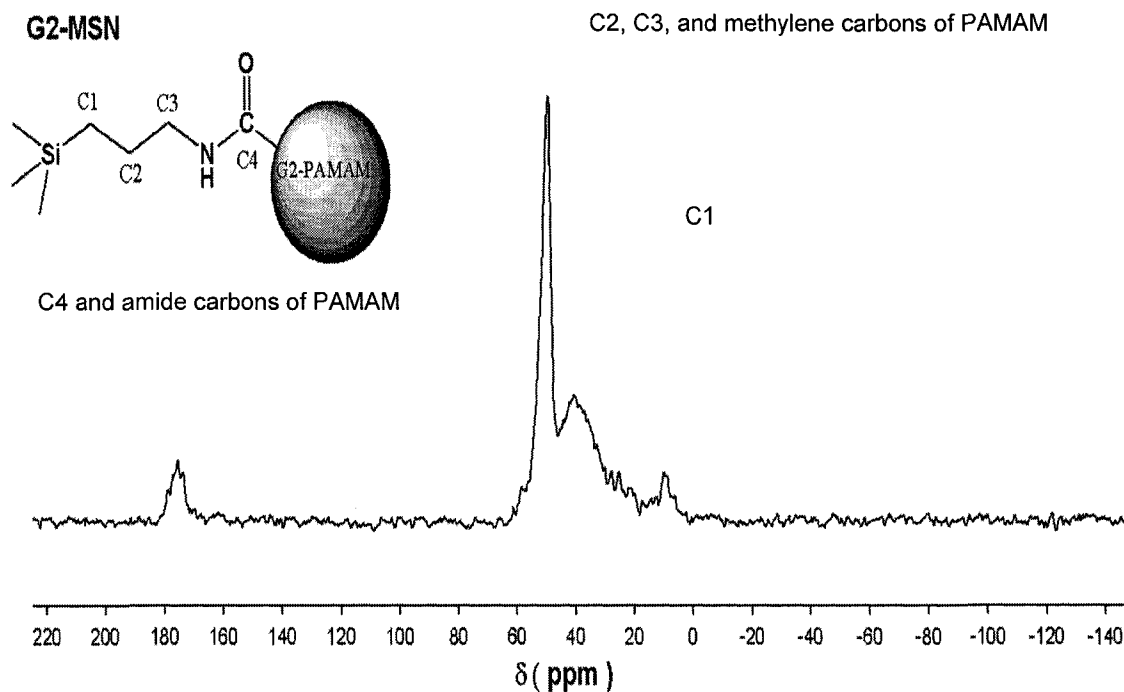
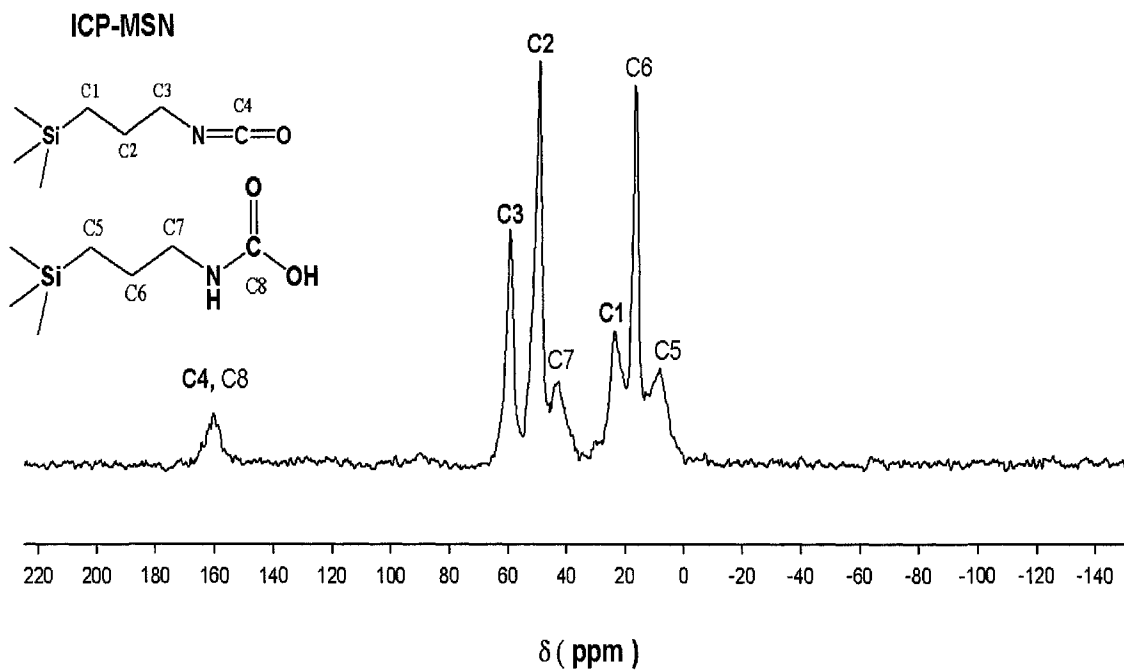


Figure 7-5.  $^{13}\text{C}$  solid state CP-MAS NMR spectra of the ICP-MSN (top) and G2-MSN (bottom) materials. Propyl-carbamic acid impurity from the hydrolyzed isocyanopropyl groups of the ICP-MSN was also observed in the spectrum of ICP-MSN.

Table 7-2. BET and BJH parameters

Sample	Nitrogen Sorption Isotherms		
	BET Surface Area	BET Pore Volume	BJH Pore diameter
	(m <sup>2</sup> /g)	(mL/g)	(Å)
MSN	959	0.865	27.3
ICP- MSN	842	0.755	27.2
G2-MSN	568	0.481	22.6
Texas Red-loaded G2-MSN	167	0.190	18.8

## Scanning and Transmission Electron Micrographs (SEM and TEM) of G2-MSN

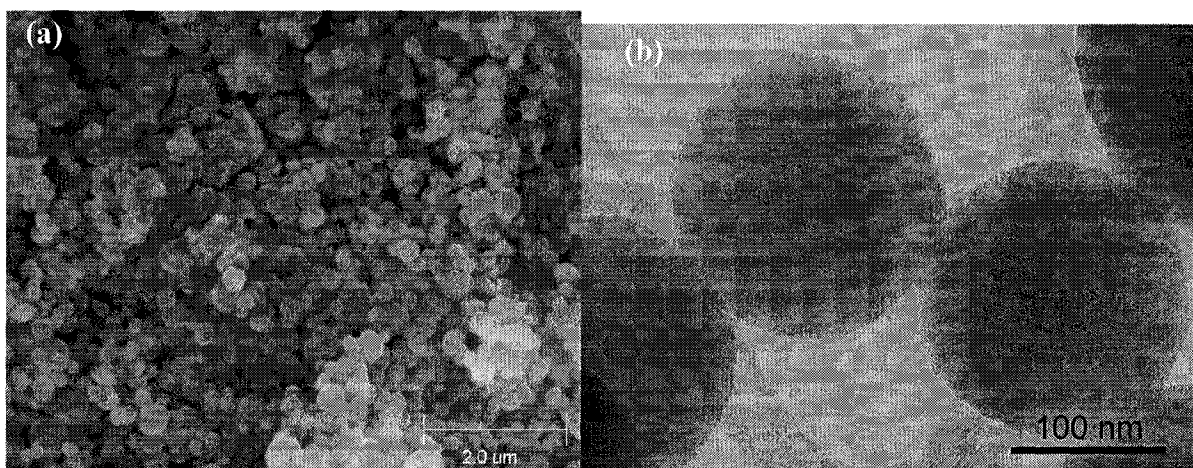


Figure 7-6. SEM (a) and TEM (300 kV) micrographs of the G2-MSN (b). The spherical shape of the silica particles is illustrated in the SEM image (a). The MCM-41 type of mesoporous channel structure of the G2-MSN is visualized by the parallel stripes shown in the micrograph (b).

Similar to the high G PAMAMs with large numbers of positive surface charges, each G2-MSN particle was covered with numerous covalently anchored G2PAMAMs. Thus, the resulting polycationic G2-MSN could complex with the polyanionic pEGFP-C1 efficiently without paying a large entropy penalty as in the case of free G2 PAMAMs complexing with plasmid DNAs.<sup>1a</sup> To examine whether the G2-MSN are efficient in protecting pEGFP-C1

DNA against enzymatic cleavage, a restriction endonuclease (*BamH* I, 2 units) was introduced to the DNA and the stable G2-MSN-DNA complexes containing 1  $\mu$ g of DNA.

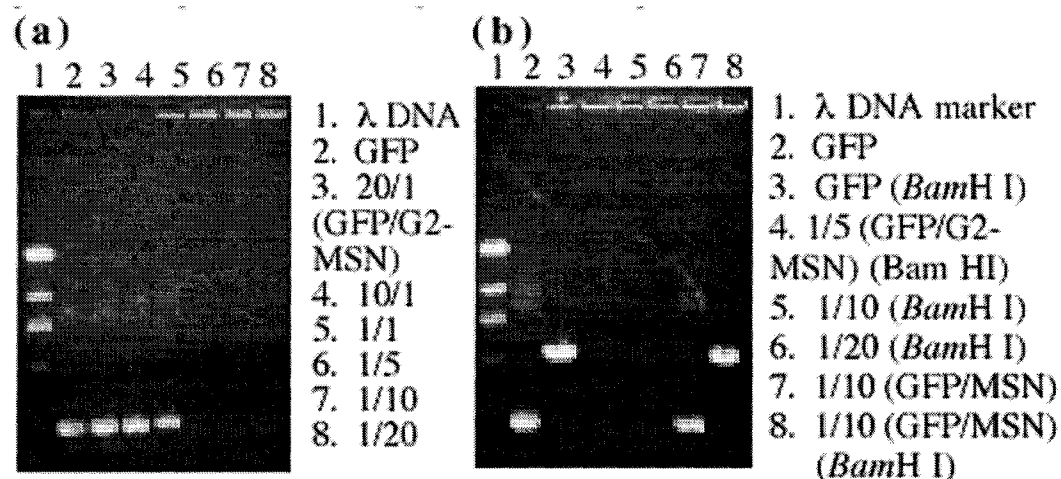


Figure 7-7. Complexation of G2-MSN with pEGFP-C1 DNA (GFP). (a) Electrophoretic gel shifts of GFP in the absence (lane 2) and increasing amounts of G2-MSN (lane 3-8). (b) Electrophoretic gel shifts of GFP complexed with 1a and uncapped MSN (MSN). Lane 2 is undigested free GFP, whereas lane 3 is the GFP digested with *BamH* I endonuclease. Lane 4-6 are GFP complexed with different ratios of G2-MSN and treated with *BamH* I. Lane 7 and 8 are the GFP complexed with uncapped MSN untreated and treated with *BamH* I respectively.

The samples were incubated for 2 h at 37 °C, followed by deactivation of enzyme at 70 °C for 15 min. As shown in Figure 7-7b, free pEGFP-C1 (lane 2) was digested and cleaved by *BamH* I, whereas the DNAs when complexed with MSNs (lane 4-6) were not cleaved by the enzyme under the same condition. We also extracted the pEGFP-C1 from the *BamH* I treated G2-MSN-DNA complex with 2 M NaCl(aq). The electrophoretic shift of the extracted DNA was the same as that of the free pEGFP-C1 suggested that the G2-MSN-DNA complex could protect DNA from enzymatic degradation.<sup>6</sup> Interestingly, pEGFP-C1 DNA was digested by *BamH* I in the presence of MSN without PAMAM caps (Figure 7-7b, lane 8).

The result indicated that the G2-MSN-DNA complex could protect pEGFP-C1 DNA from enzymatic degradation (Figure 7-9).

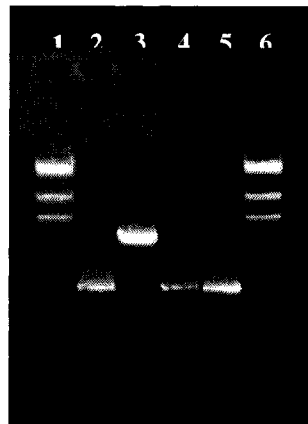


Figure 7-8. Electrophoretic gel shifts of stability Studies of pEGFP-C1 DNA and G2-MSN-DNA Complex after Bam H1 treatment. Lanes 1 and 6: DNA marker ( $\lambda$  DNA). Lanes 2 and 5: Undigested free plasmid DNA (pEGFP-C1). Lane 3: Free plasmid pEGFP-C1 after digestion with *BamH* I (2 U/ $\mu$ g DNA). Lane 4: The pEGFP-C1 extracted from the *BamH* I (2 U/ $\mu$ g DNA) treated G2-MSN-DNA complex with 2 M NaCl(aq).

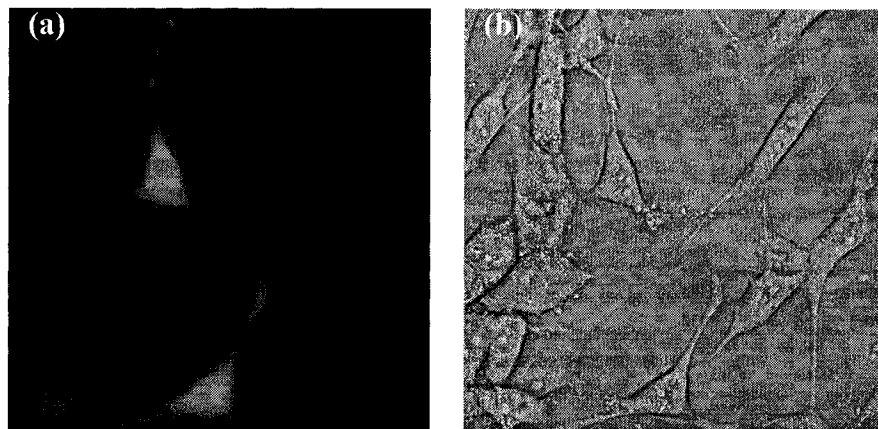


Figure 7-9. Fluorescent microscopy images of HeLa cells treated with G2-MSN-DNA complexes that have first been exposed to *BamH* I. (a) HeLa cells with green fluorescent proteins expressed. (b) Phase contrast image of the same region of interest.

To investigate the transfection efficacy of our system, G2-MSNs without Texas Red (10  $\mu$ g) were mixed with 1  $\mu$ g of pEGFP-C1.6 The MSN/DNA suspension (60  $\mu$ L/well) was further added to the cells on 24-well plates ( $6 \times 10^4$  cells per well, in 0.6 mL growth medium) and incubated for 4 hours at 37°C. The cells were then washed with PBS buffer and cultured with DMEM + 10% calf serum (CS) medium and antibiotics for 2 days. The transfected cells



were trypsinized and resuspended in 0.5 ml of PBS for direct flow cytometric analysis to evaluate the expression of GFP. Control experiments utilizing cultures of untransfected cells and “mock”-transfected cells (cells incubated with MSNs without pEGFP-C1) were measured with an EPICS-ALTRA flow cytometer. As shown in Figure 7-10 and Table 7-3, significant GFP-expression was observed. To compare the transfection efficiency of G2-MSN with other commercial transfection reagents, we conducted pEGFP-C1 transfection experiments on HeLa cells with PolyFect, SuperFect, and Metafectene under the same experimental conditions.<sup>6</sup> Flow cytometry analyses on the 48 h post transfection cells showed efficiencies of  $35 \pm 5\%$  (G2-MSN),  $15 \pm 2\%$  (PolyFect),  $10 \pm 2\%$  (SuperFect), and  $16 \pm 2\%$  (Metafectene).<sup>6</sup>

Table 7-3. Transfection Efficiencies of different transfection reagents on HeLa cells.

Transfection Reagent	Population (%)	X mean Intensity
G2-MSN	$35 \pm 5$	$129 \pm 13$
PolyFect <sup>®</sup>	$15 \pm 2$	$312 \pm 4$
SuperFect <sup>®</sup>	$10 \pm 2$	$250 \pm 50$
Metafectene <sup>®</sup>	$16 \pm 2$	$248 \pm 20$

The transfection enhancement of the G2-MSN could be attributed to the *particle sedimentation effect* as previously reported by Luo *et al.*<sup>4a,d</sup> To examine the mammalian cell membrane permeability, Texas Red-loaded G2-MSNs were introduced to GFP-transfected rat astrocytes. The confocal fluorescence micrograph (Figure 7-11b) clearly illustrated that the G2-MSNs (red fluorescent dots) entered into the cytoplasm of a green fluorescent neural glia cell.

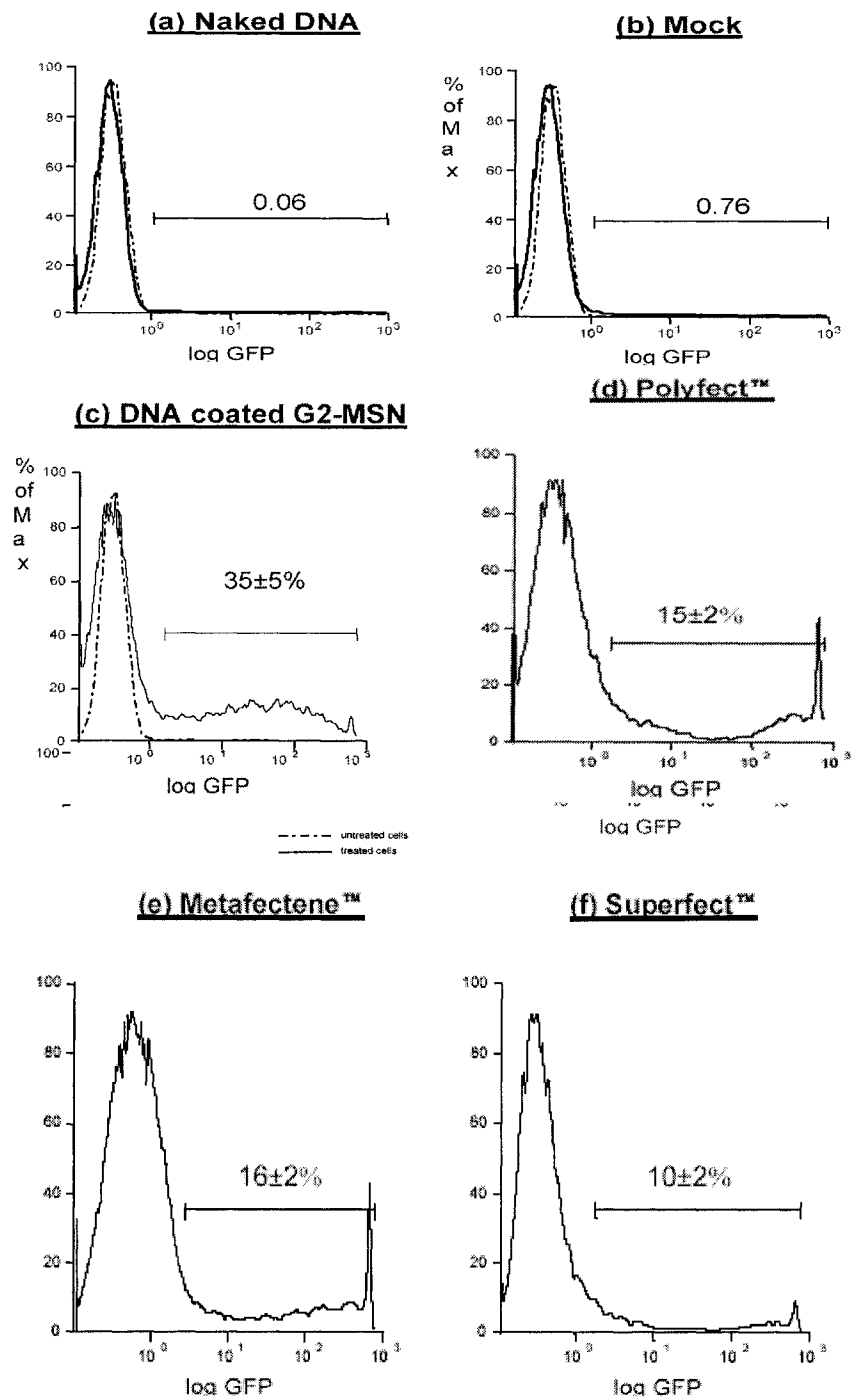


Figure 7-10. Flow cytometry analysis of the transfection of pEGFP in HeLa cells with G2-MSN. The flow cytometry histograms show distribution of events on the green (FL1) channel. (a) Nontransfected control experiment: HeLa cells (dashed line) and HeLa cells treated with pEGFP-C1 DNA (solid line). (b) “Mock” transfection control experiment: HeLa cells (dashed line) and HeLa cells treated with MSNs without DNA (solid line). (c) G2-MSN transfection results: HeLa cells (dashed line) and HeLa cells treated with pEGFP-C1 DNA-coated G2-MSNs. HeLa cells transfected different commercially available transfection reagents (d), (e), and (f).

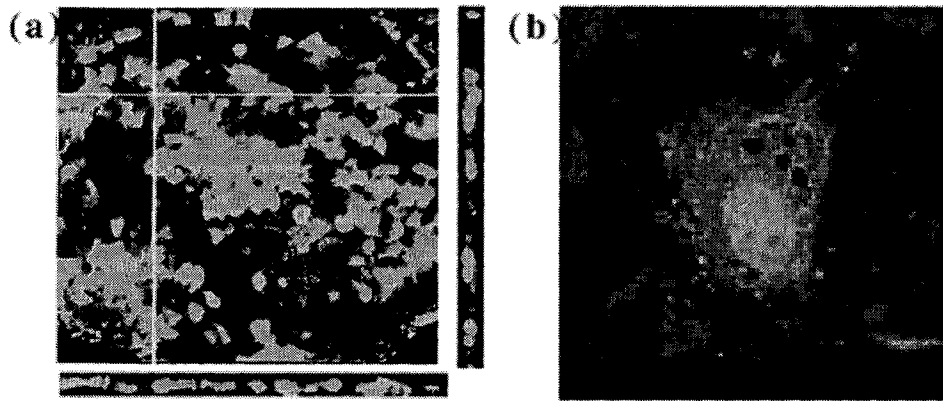
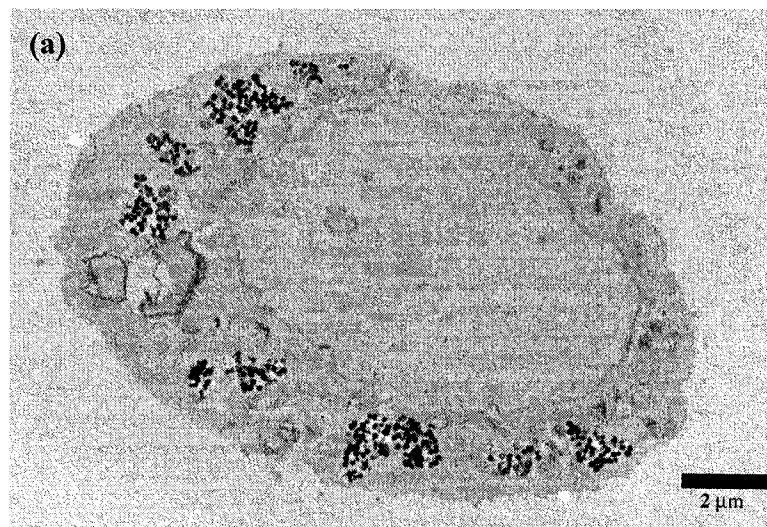
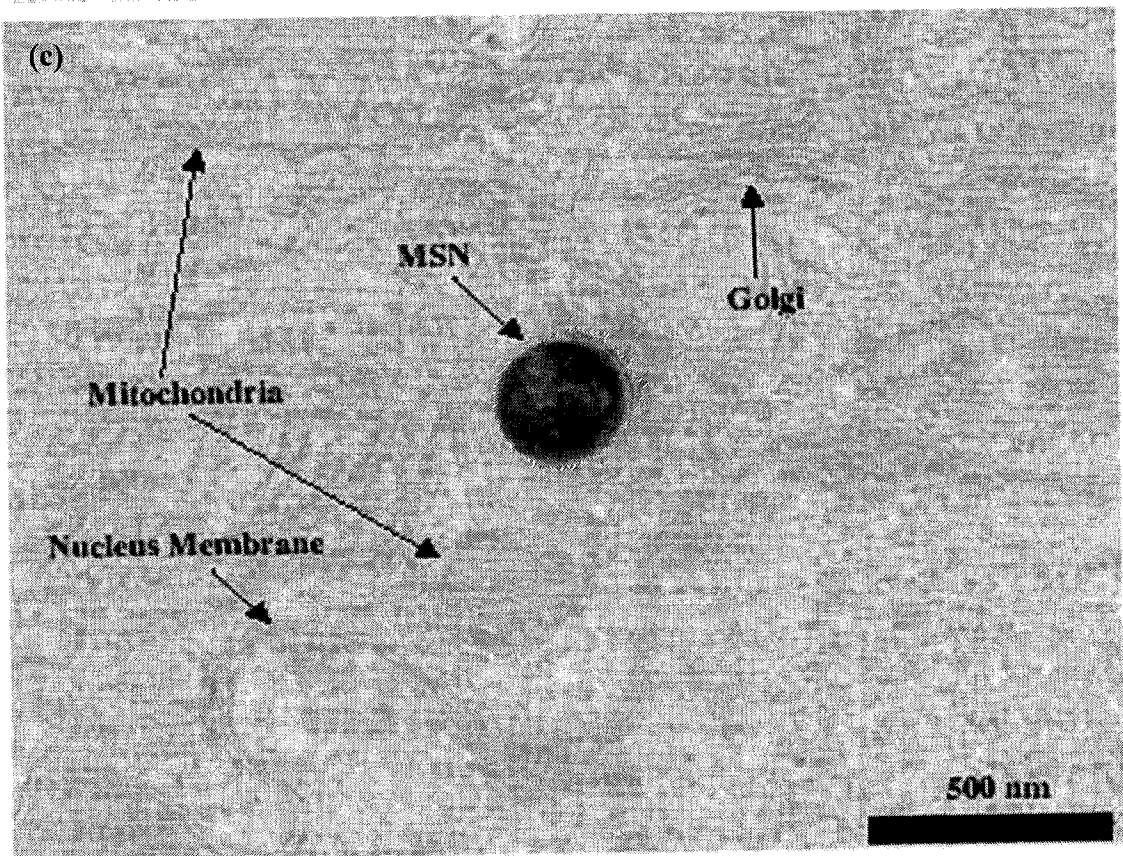
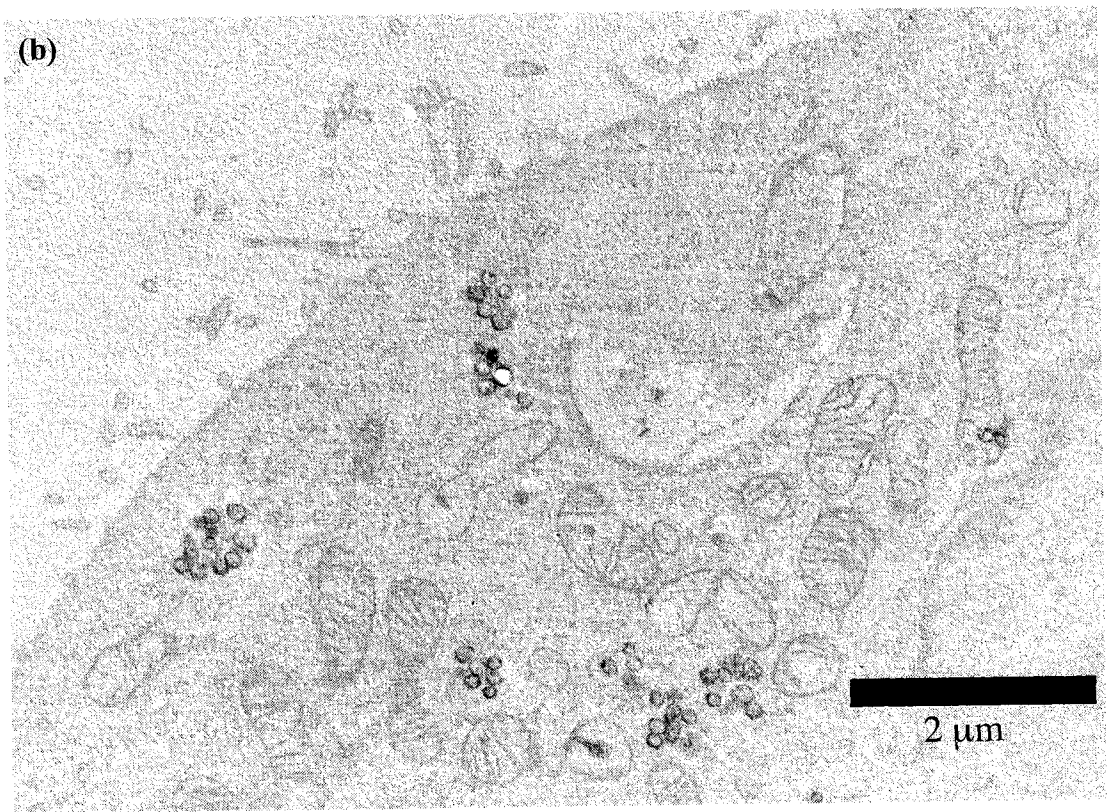


Figure 7-11. Fluorescence confocal micrographs of cells transfected by pEGFP-C1-coated G2-MSN system (a) GFP transfected HeLa cells showing cross-sections through a cell layer. Orthogonal images indicated the monolayer packing of cells. (b) Texas Red-loaded G2-MSNs inside a GFP-transfected rat neural glia cell (astrocyte).

Transmission electron micrographs of the posttransfection cells also provided direct evidence that a large number of G2-MSN-DNA complexes were endocytosed by all three types of cells (Figure 7-12). It is noteworthy that many subcellular organelles, such as mitochondria and Golgi, were observed with MSNs nearby as shown in Figure 7-12b, c and d. Given the fact that these organelles disappear rapidly upon cell death, the result strongly suggested that the MSNs were not cytotoxic *in vitro*.





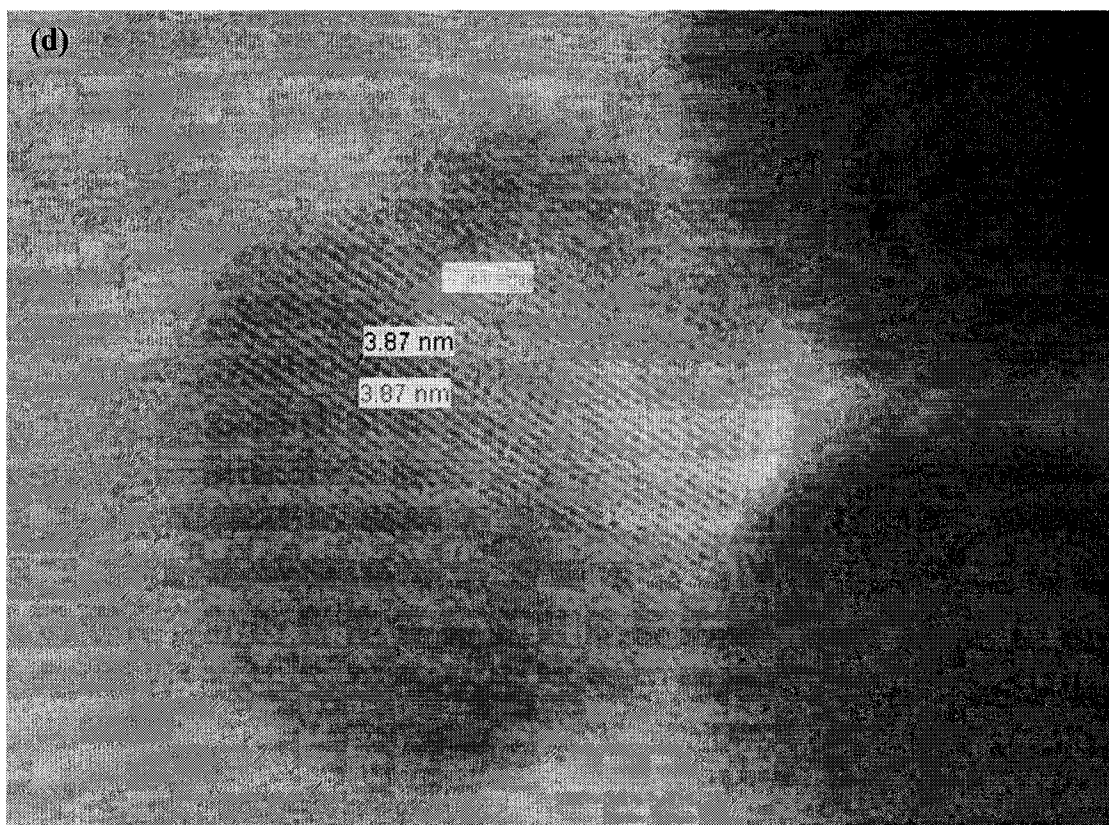


Figure 7-12. TEM micrographs of G2-MSN-DNA complexes (black dots) endocytosed by Chinese hamster ovarian (CHO) (a), human cervical cancer (HeLa) (b), and neural glia (astrocytes) (c) cells. Subcellular organelles, e.g., mitochondria and Golgi, were observed with MSNs nearby (b) and (c). The measured distance between channels (d) (including the pore walls) is consistent with the BJH average pore diameter of 3-4 nm from  $N_2$  sorption isotherms of the MSN material alone, zooming in image taken from neural glia cells..

To further investigate the biocompatibility of G2-MSN, we compared the cell growth profiles of HeLa cultures without and with G2-MSNs (0.1mg/mL). The numbers of cells from cultures with and without G2-MSNs were counted daily for 6 days.<sup>6</sup> The doubling times of the cell density of HeLa cells without and with MSNs were calculated from the semilog plots to be 20 h and 24 h, respectively. The doubling times of CHO cells without and with MSNs were calculated to be 21 h and 24 h, respectively. ( $R^2 \geq 97\%$  in the case of HeLa cells, whereas  $R^2 \geq 97.6\%$  for CHO cells)

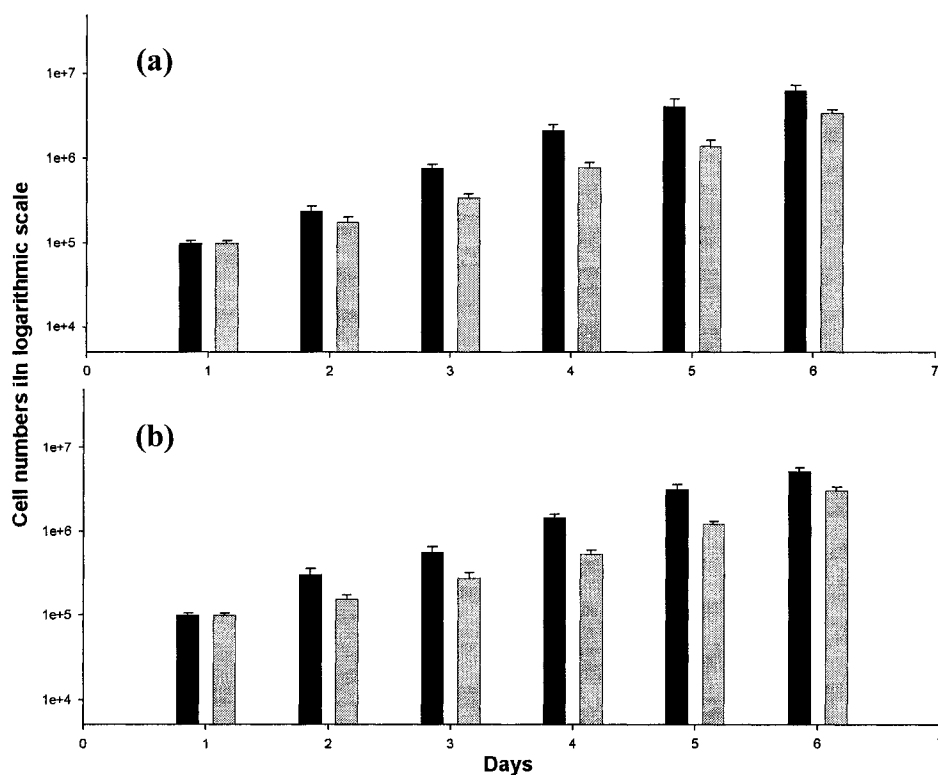


Figure 7-13. Cell growth of (a) HeLa and (b) CHO cells in the presence of G2-MSN (gray bars) and in the absence of G2-MSN (black bars).

Shown in Figure 7-13, the slopes of the cell growth curves from those cultures with and without G2-MSNs were very similar indicated that the increase of numbers of cells was not hindered by the presence of G2-MSNs. We envision that the G2-MSN material could serve as a new transmembrane delivery system for many biotechnological applications.

### Conclusions

The mesoporous structure of the MSN material shows exogeneous biomolecules such as DNA or membrane impermeable molecules, such as pharmaceutical drugs and fluorescent dyes, to be encapsulated inside the MSN channels. The system renders the possibility to serve as a universal transmembrane carrier for intracellular therapeutic gene therapy, drug delivery and imaging applications.

## Acknowledgements

This research was supported by the NSF (CHE-0239570). The authors thank Dr. Robert Doyle and the cell and hybridoma facilities of ISU for their assistance.

## References

1. Dennig, J.; Duncan, E. *Rev. Mol. Biotechnol.* **2002**, *90*, 339-347, and the references therein. (b) Esfand, R.; Tomalia, D. A. *Drug Discovery Today* **2001**, *6*, 427.
2. Lai, C.-Y.; Trewyn, B. G.; Jeftinija, D. M.; Jeftinija, K.; Xu, S.; Jeftinija, S.; Lin, V. S.-Y. *J. Am. Chem. Soc.* **2003**, *125*, 4451.
3. Subramanian, S.; Srienc, F. *J. Biotechnol.* **1996**, *49*, 137.
4. (a) Luo, D.; Saltzman, W. M. *Nat. Biotechnol.* **2000**, *18*, 893. (b) Kneuer, C.; Sameti, M.; Bakowsky, U.; Schiestel, T.; Schirra, H.; Schmidt, H.; Lehr, C.-M. *Bioconjugate Chem.* **2000**, *11*, 926. (c) He, X.-X.; Wang, K.; Tan, W.; Liu, B.; Lin, X.; He, C.; Li, D.; Huang, S.; Li, J. *J. Am. Chem. Soc.* **2003**, *125*, 7168. (d) Luo, D.; Han, E.; Belcheva, N.; Saltzman, W. M. *J. Controlled Release* **2004**, *95*, 333.
5. Mal, N. K.; Fujiwara, M.; Tanaka, Y. *Nature (London)* **2003**, *421*, 350.
6. See experimental section for details.

Chapter 8. An Intracellular Mesoporous Silica Nanosphere-based Controlled Release  
Delivery Carrier for Anticancer drugs and Multi-plasmids Transfection

A paper submitted to *Nature Biotechnology*

Lai, C.-Y.; Radu, D.R.; Lin, V.S.-Y.

Department of Chemistry, Iowa State University, Ames, Iowa 50011-3111

Abstract

Silica mesoporous nanomaterials have been utilized in various applications. For applying these materials in biology, they have to fulfill several prerequisites: a) narrow size distribution within a safe size-range defined from 100 nm to 1  $\mu$ m for biocompatibility reasons; b) versatility in exterior particle surface modifications for receptor targeting purposes or simply for improving particles biocompatibility; c) high chemical and thermal stabilities for increased feasibility. We are reporting on a intracellular delivery nano-vehicle that successfully responded to all these prerequisites and further proved pluripotency in biological applications. In the present work, the mesoporous silica nanospheres (MSNs) have been utilized for: drug delivery by encapsulating Doxorubicin inside the mesopores and controlled release of the drug in HeLa cancer cells and for transfection of different types of cells such as cancer cell lines: HeLa human cervical cancer and CHO Chinese hamster ovarian cells as well as primary cells such as neurons and glia.

Introduction

The developing of systems for investigation/intervention in cellular phenomena implies downsizing the components of the system to match the size of the cellular components. In the present work, we developed a nanocomposite Mesoporous Silica Nanosphere (MSN)-based system that is functioning as a cellular vehicle endowed with the ability of carrying exogenous molecules in the cytosol. The research performed in developing built-in delivery properties for pharmaceutical drugs is still relying on specialized synthesis for each particular group of molecules. Consequently, the development of delivery systems is as important as the development of the drugs. Several types of polymers were employed to



perform the intracellular delivery task. Often, polymeric system is too specialized on particular applications<sup>1</sup> whereas supramolecular assemblies such as dendritic boxes are still suffering from lack of controlled release as well as limited loading capacity. In terms of silica mesoporous materials utilization, other than MSN, the application of such materials in the biological field, e.g. in drug delivery, was disappointing due to their low biocompatibility (irregular shape and size, out-ranging the biocompatible size). To respond to all prerequisites related to biotechnological applications, several modifications of mesoporous silica materials have been achieved by different research groups.<sup>2</sup> Several organic-group modified mesoporous silica materials have been synthesized by *in situ* co-condensation of organosilane precursors and a silica source, e.g. tetraethyl orthosilicate (TEOS), in the presence of a templating surfactant. However, there were no morphological improvements reported, that would allow the successful use of these materials in drug delivery. In our recently published work,<sup>3</sup> we have been reporting morphological as well as surface modifications of mesoporous silica that lead to Mesoporous Silica Nanospheres (MSN). Herein we present a mesoporous silica nanospherical device that has the ability to encapsulate and control release to HeLa cervical cancer cells an antineoplastic antibiotic--Doxorubicin--proving an incommensurable potential in applications in drug delivery to living systems. As therapeutic methods extend their field from simple drug molecules to polymeric proteins and genes, virtually, our system, with mesopores in the range of 2-4 nm,<sup>4</sup> would not have the internal capacity necessary for encapsulating the drugs. However, the engineering of the surface with functionalities that enable it to electrostatically bind these aforementioned molecules allows the system to deliver their cargo. We demonstrated that HeLa human cancer cells, CHO murine cancer cells, and primary cells such as astroglia can be transfected and cotransfected by using MSNs as gene carriers.

## Materials and Methods

### Experimental Section

**Materials.** 3-Aminopropyltrimethoxysilane (APTES), *n*-cetyltrimethylammonium bromide (CTAB), 3-mercaptopropyltrimethoxysilane (MPTES), sodium sulfide, and tetraethoxysilane (TEOS) were all obtained from Aldrich and used without further purification. Nanopure

water (18.1 MHz) prepared from a Barnstead E-pure water purification system was employed throughout. Fluorescein 5-isothiocyanate (FITC) and Texas Red sulfonyl chloride were purchased from Molecular Probe (Eugene, OR.).

#### Synthesis of G2 -MSN<sup>5</sup>

*N*-(3-triethoxysilylpropyl)-4,5-dihydroimidazole was purchased from Gelest, and all other chemicals were purchased from Aldrich. All chemicals were used as received without further purification. The role of imidazole group is associated with the ability of weak bases to confer the buffer capacity necessary for manipulating the endosomal pH.

Hexagonally ordered IMI-MSN was prepared by the following procedure: *N*-Cetyltrimethylammonium bromide (CTAB, 1.00 g,  $2.74 \times 10^{-3}$  mol) was dissolved in 480 mL of Nanopure water. NaOH (aq) (2.00 M, 3.50 mL) was added to CTAB solution and the solution temperature was adjusted to 353 K. At this temperature, TEOS (5.00 mL,  $2.57 \times 10^{-2}$  mol) was introduced dropwise to the surfactant solution, followed by the dropwise addition of *N*-(3-triethoxysilylpropyl)-4,5-dihydroimidazole (0.928 mL,  $5.13 \times 10^{-3}$  mol), both additions being performed under vigorous stirring. The mixture was allowed to stir for 2 h to give rise to a white precipitate: template-containing IMI-MSN. The solid product was filtered, washed with deionized water and methanol, and dried in air. To remove the surfactant template (CTAB), 1.50 g of as-synthesized IMI-MSN was refluxed for 24 h in a solution of 9.0 mL of HCl (37.4%) and 160.00 mL of methanol followed by extensive wash with deionized water and methanol. The resulting surfactant-removed IMI-MSN material was placed under high vacuum to remove the remaining solvent from the mesopores. The surfactant-free IMI-MSN material was placed under high vacuum to remove the remaining solvent from the mesopores. IMI-MSN (1.00 g) was refluxed for 20 h in 80.00 mL of anhydrous toluene with 0.25 mL (1.00 mmol) of 3-isocyanatopropyltriethoxysilane to yield the 3-isocyanatopropyl-functionalized MSN (ICP-MSN) material.

The purified ICP-MSN (0.15 g) was added to anhydrous ethanol (3.00 mL). A second-generation (G2) polyamidoamine dendrimer (PAMAM, 2.00 mL, 0.11 mmol) was then added to the ICP-MSN ethanol solution. The amino groups of the G2-PAMAM were allowed to react with the ICP functional groups present on the surface of MSN for 20 h at room temperature to yield the G2-PAMAM-capped MSN material (G2-MSN). The resulting

G2-MSN material was filtered and washed thoroughly with ethanol, methanol and acetone and dried under high vacuum.

#### Synthesis of dye-Incorporated MSN (F-MSN and T-MSN)<sup>5</sup>

For synthesizing dye incorporated MSNs, fluorescein isocyanate (3mL of 8 mM DMF solution to allow the fluorescent dye to be embedded inside the silica matrix,  $2.4 \times 10^{-5}$  mol, Molecular Probe) was first covalently attached to the coupling agent 3-aminopropyltriethoxysilane (0.9 mL,  $5.1 \times 10^{-3}$  mol, APTES) by addition of the amine group to the FTIC group in anhydrous DMF solution. For Texas-Red doped MSNs, Sulforhodamine 101 sulfonyl chloride solution (3mL of 8 mM DMF solution,  $2.4 \times 10^{-5}$  mol, Texas Red<sup>TM</sup>, Molecular Probe) was added to 3-mercaptopropyltrimethoxysilane (0.97 mL,  $5.13 \times 10^{-3}$  mol, MPTES) to allow the reaction between the mercapto group and the sulfonyl chloride and both mixtures were stirred for 4 hours under nitrogen atmosphere. After 4 hour later, this mixture was added dropwise immediately after TEOS addition, the rest of conditions being identical with the aforementioned preparation. The resulting FTIC-MSN/Texas Red-MSN materials were filtered and washed thoroughly with ethanol, methanol and acetone and dried under high vacuum. To remove the surfactant template (CTAB), 1.50 g of as-synthesized FTIC-MSN or Texas Red-MSN was refluxed for 24 h in a solution of 9.0 mL of HCl (37.4%) and 160.00 mL of methanol followed by extensive wash with deionized water and methanol. The resulting surfactant-removed FTIC-MSN or Texas Red-MSN material was placed under high vacuum to remove the remaining solvent from the mesopores. To ensure the complete removal of FTIC or Texas Red molecules physisorbed on the surface of MSN, a Soxhlet extraction in ethanol was performed for 20 h. The resulting solid was filtered and dried in air.

#### Characterization of ICP-MSN and G2-MSN<sup>5</sup>

##### Powder X-Ray Diffraction

Powder XRD experiments were performed on a Scintag XDS 2000 diffractometer using a Cu K $\alpha$  radiation source. Low angle diffraction with a  $2\theta$  range of 1 to  $10^\circ$  was used to investigate the long-range order of the materials.

### Nitrogen adsorption/desorption isotherms

The surface area and median pore diameter were measured using N<sub>2</sub> adsorption/desorption measurements in a Micromeritics ASAP 2000 BET surface analyzer system. The data were evaluated using the Brunauer-Emmett-Teller (BET) and Barrett-Joyner-Halenda (BJH) methods to calculate the surface area and pore volumes/pore size distributions, respectively. Samples were prepared by degassing at 90 °C for 1 h and then at 150 °C for 4 h.

### Solid-state <sup>13</sup>C CP-MAS NMR

Solid-state <sup>13</sup>C CP-MAS NMR spectra were obtained at 75.47 MHz on a Bruker MSL300 spectrometer equipped with Bruker 4mm rotor MAS probe. Magic-angle sample spinning rate was maintained at 10 KHz for <sup>13</sup>C in order to minimize the spin band due to the high anisotropic chemical shifts of aromatic carbons. The NMR spectra consisted of 5,000 to 20,000 acquisitions with cross polarization times of 3 ms (<sup>13</sup>C) and pulse repetition times of 15 s (<sup>13</sup>C). All chemical shifts reported are referenced to liquid Me<sub>4</sub>Si (TMS).

### Scanning and Transmission Electron Micrographs (SEM and TEM) of G2-MSN

Particle morphology of these materials was determined by scanning electron microscopy (SEM) with 10 kV accelerating voltage and 0.005 nA of beam current for imaging. For transmission electron microscopy (TEM) studies, a small aliquot was taken from a suspension of methanol and placed in a lacey carbon-coated TEM grid, which was pulled through the suspension and allowed to dry in air. Thin sections of samples embedded in epoxy resin were obtained with ultramicrotomy (60-80 nm). The resulting sample was examined with a Philips model CM-30 TEM operated at 300 kV. The specimen was given no further treatment, as it appeared stable under beam bombardment.

### Cell Growth Studies

To further demonstrate the in vitro biocompatibility of the G2-MSN, growth studies were performed for HeLa and CHO cells. Two series of experiments were designed for both types of cells: one series studied the natural cells growth (without MSNs) and the other was monitored after MSNs application. All experiments were performed in triplicate. To ensure

enough space and media for cell growing, the cells were seeded in T-25 flasks. In the experiments without MSNs, 18 flasks were loaded with the same amount of cells for each cell type. After allowing 24 h for cell adhesion, the cells were analyzed everyday (3 flasks per day) for 6 days. The cells were trypsinized and counted by using a Guava ViaCount® assay (Guava Technologies, Inc, USA). In the experiments with G2-MSNs, the cells were seeded for 24 h prior to the incubation with MSNs at 0.1mg/mL concentration in DMEM + 10% CS (calf serum) and antibiotics for 4 h. After the 4 h incubation, the cells were washed twice with PBS buffer and incubated for another 6 days. The aforementioned cell counting procedures were followed. All experiments were performed in triplicate (3 flasks /day). During the 6-day growth period, the cells were periodically examined under a phase contrast microscope. The cells were added with fresh media every other day or upon pH fluctuations (Phenol Red dye was used as pH indicator). The doubling times of the cell density of HeLa cells without and with MSNs were calculated from the semilog plots to be 20 h and 24 h, respectively. The doubling times of CHO cells without and with MSNs were calculated to be 21 h and 24 h, respectively. ( $R^2 \geq 97\%$  in the case of HeLa cells, whereas  $R^2 \geq 97.6\%$  for CHO cells).

#### Endocytosis Mapping of Cells

For cell mapping studies, the cells were seeded with dye doped MSNs (such as FTIC-MSN) at 0.1mg/mL concentration in DMEM + 10% CS (calf serum) and antibiotics for 4 h. After the 4 h incubation, the cells were washed twice with PBS buffer and incubated for another 24 hours. Before imaging, the samples were washed three times with PBS buffer and fixed with formaldehyde in PBS (3.7 %). After washing again with PBS, images were captured by confocal microscope.

#### Gene Transfection Experiments of DNA-coated G2-MSNs<sup>5</sup>

##### Experimental Section

Human cervical cancer (HeLa) and Chinese Hamster Ovarian (CHO) cell lines were obtained from American Tissue Culture Collection (ATCC). Astrocyte Cells are donated from Dr. Srdija Jeftinija at Iowa State University. HeLa and CHO cells were maintained in T75 flasks using DMEM (Dulbecco's modified Eagle's medium) supplemented with 10%

calf serum, 2 mM L-glutamine, 100 U/mL penicillin, 100  $\mu\text{g}/\mu\text{L}$  streptomycin, and 1  $\mu\text{g}/\mu\text{L}$  gentamycin. Astrocytes cells were in Eagle's minimum essential medium (EMEM) containing 10% serum. All cells were passaged when its confluence is reaching 90% of the plates. pDsRed1-N1 and pEGFP-C1 plasmids (Clontech, Palo Alto, CA) were used as reporter proteins. All plasmids were amplified in the *E. coli* strain DH5 $\alpha$  and purified according to the manufacturer's protocol (Qiagen, USA). The isolated DNA was resuspended in Tris-EDTA (pH 8.0) at a concentration of 1  $\mu\text{g}/\mu\text{L}$ .

HeLa and CHO cells were first seeded onto 24-well plates ( $6 \times 10^4$  cells per well, in 0.6 mL growth medium) 24 h prior to the experiment. Astrocytes were deposited on 24 wells ( $7 \times 10^4$  cells per well, in 1.0 mL growth medium).

In a typical transfection experiment, 1  $\mu\text{g}$  pEGFP-C1 and 1  $\mu\text{g}$  pDsRed1-N1 (1 to 1 ratio) were added to 10  $\mu\text{g}$  of G2-MSN suspension obtained by dispersing the nanosphere material in 30  $\mu\text{L}$  of HEPES buffer solution (10 mM HEPES, pH 7.4). The complex mixture was incubated for 2 h at 4  $^{\circ}\text{C}$ . To further compact the DNA bound to the G2-MSN for more gene transfection efficiency and protection of the DNA from enzymatic degradation, the G2-MSN were incubated with 30  $\mu\text{L}$  of 100 mM  $\text{CaCl}_2$  aqueous solution for another 2 hours. The G2-MSN/DNA suspension was further added to the cells cultured on 24-well plates and incubated for 4 hours at 37  $^{\circ}\text{C}$  and each well contained 0.6 mL DMEM (free of  $\text{Ca}^{2+}$  and  $\text{Mg}^{2+}$ ) and consequently the addition of the complex resulted in a final  $\text{CaCl}_2$  concentration of 4.5 mM. After 4 hours, the transfection mixture was removed by washing the transfected cells with PBS buffer and cultured with DMEM supplemented with 10% calf serum (CS) and antibiotics. The cultures were maintained for 2 days to monitor gene expression.

To compare the transfection efficiency of our G2-MSN system with other commercially available transfection reagents, three different reagents, PolyFect<sup>®</sup> and SuperFect<sup>®</sup> (Qiagen, Valencia, California) were used to transfect the aforementioned cell types under the same experimental condition. First, 16 and 10  $\mu\text{L}$  of the stock solutions of PolyFect<sup>®</sup> (2 mg/mL) and SuperFect<sup>®</sup> (3 mg/mL), respectively, were added to a 60  $\mu\text{L}$  of serum-free medium (DMEM) containing 1  $\mu\text{g}$  pEGFP-C1 and 1  $\mu\text{g}$  pDsRed1-N1 (1 to 1 ratio). The solutions were incubated at room temperature for 15 min to allow the formation

of stable complexes between DNA molecules and transfection reagents. The complexes were then added to a culture of cells in a 24 well plate with a cell density of  $6 \times 10^4$  cells/well that contained 700  $\mu$ l of pre-warmed DMEM + 10% CS medium and antibiotics. After 4 h of incubation, the transfection medium was discarded and replaced with fresh growth medium (DMEM + 10% CS medium and antibiotics). The cells were evaluated for expression of the GFP and RFP by flow cytometry after 48 h post-transfection.

#### Flow Cytometric Analysis of transfected cells<sup>5</sup>

Flow cytometric measurements were performed immediately after collection of cultured cells. All cells were trypsinized and resuspended in 0.5 mL of PBS before the FACS analysis. Positive and negative control experiments utilizing cultures of untransfected cells (cells only) and “mock”-transfected cells (cells incubated with MSNs without DNA plasmid) were measured with an EPICS-ALTRA flow cytometer (Beckman Coulter, Miami, FL), using a 488 nm laser for GFP and RFP excitation. GFP fluorescence was detected using PMT2 in conjunction with a 525 nm band-pass filter and RFP fluorescence used PMT3 in conjunction with a 583 nm band-pass filter. An electronic gate was set around cells based on the forward and side scatter properties of the population and a minimum of 10,000 gated events per sample were collected and stored in list mode files. Data analysis was performed with FlowJo software (Tree Star, Ashland, OR). All experiments were performed in quadruplicate. Untransfected cells were used for background calibration. The average transfection efficiencies of different transfection reagent systems on HeLa cells were summarized on Figure 8-13 and 8-15.

#### Confocal Microscopy Imaging of Transfected Cells<sup>5</sup>

HeLa and CHO cells were grown on coverslips in a 24-well culture plate. All of the samples were washed three times with PBS buffer and fixed with formaldehyde in PBS (3.7 %). After washing again with PBS, images were captured on an inverted Nikon Eclipse microscope connected to a Prairie Technologies (Middleton, WI) Scanning Laser Confocal Microscope controlled by Prairie Technologies software. Images were analyzed using

Metamorph software (Universal Imaging, West Chester, PA). The samples were imaged by FTIC channel for GFP and TRIC channel for Ds-Red.

### Transmission Electron Micrographs of G2-MSN transfected Cells <sup>5</sup>

To study the endocytosis of G2-MSN, cells were fixed 4 and 24 hours after a typical transfection experiment with 2% glutaraldehyde/2% paraformaldehyde in PBS buffer and incubated overnight at 4°C to visualize the location of MSNs. After washing with PBS, cells were dehydrated with graded ethanol and coated with 2% osmium tetroxide (Aldrich). TEM samples were sectioned in epoxy resin by microtome and developed using 2% uranyl acetate and 0.04% lead citrate.

## Results and Discussion

### MSNs biocompatibility study

The application of our system directly to living cells involves two preliminary steps: successful derivatization of MSNs for the desired application and biocompatibility screening. To monitor the interaction of the MSN beads with the cellular environment we have prepared dye-doped particles, by incorporating fluorescent dyes inside the silica matrix. This embedding was performed in situ, during the synthesis of the material.<sup>6</sup> As flow cytometry instruments are often using lasers Kr and Ar lasers, the fluorescent dyes of choice were derivatives of fluorescein and of Texas Red. The synthesis of the particles: fluorescein modified (F-MSN) and Texas Red modified (T-MSN), involve a slight modification

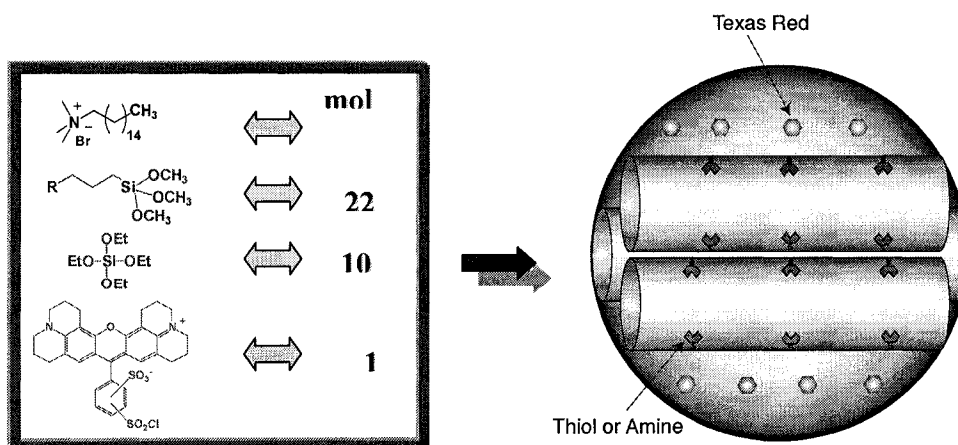


Figure 8-1. Schematic representation of Texas Red incorporated mesoporous silica nanospheres , T-MSN.



The synthetic pathway proposed in our previously published work resulted in morphological changes from polydisperse particles with irregular shape to nanospheres with high monodispersity (average diameter of 200 nm). The particles synthesized with fluorescent dyes were maintaining this morphology as suggested in Figure 8-1 and showed in the SEM images in Figure 8-2.

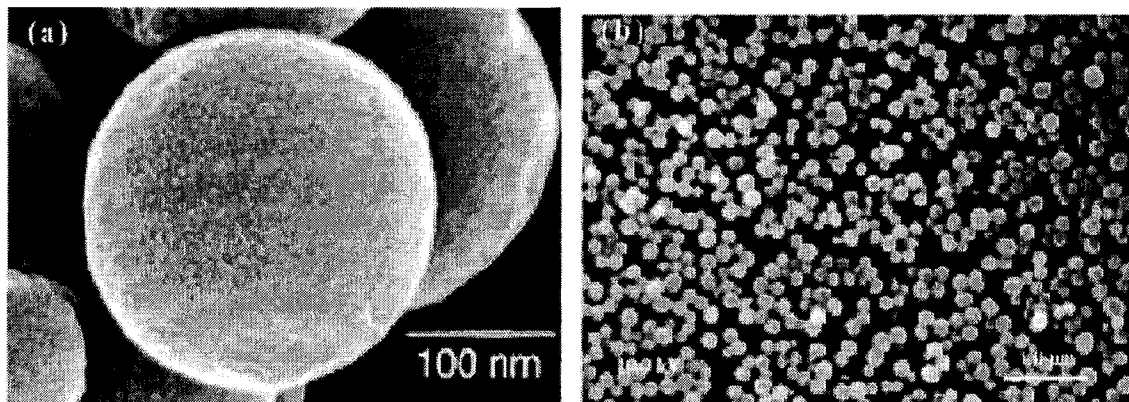


Figure 8-2 Scanning electron micrographs (SEM) of the mesoporous silica nanospheres (MSN). Scale bars = 100 nm (a) and 1.0  $\mu\text{m}$  (b).

The TEM micrographs in Figure 8-3 also show that the synthetic modifications of F-MSN and T-MSN did not affect the well organized mesoporosity characteristic to non-functionalized materials. The fluorescence of the materials was concluded by suspending aliquots of material in water and monitoring their fluorescent signal. A very high stability of the signal with time was observed, while the emission profile was similar with that belonging to the Texas Red monitored in water solution. Based on this observation we concluded that the covalent linkage between the fluorophores and the silica matrix prevented the undesired fluorophore-leaching problem. The biocompatibility screening was performed by applying the two fluorescent materials, F-MSN and T-MSN, to HeLa and CHO cancer cell lines. To evaluate the influence of fluorescent MSNs treatment on cells behavior, growth studies were performed for HeLa and CHO cells. The study concluded that after application of the MSNs, the cells followed their homeostatic behavior.

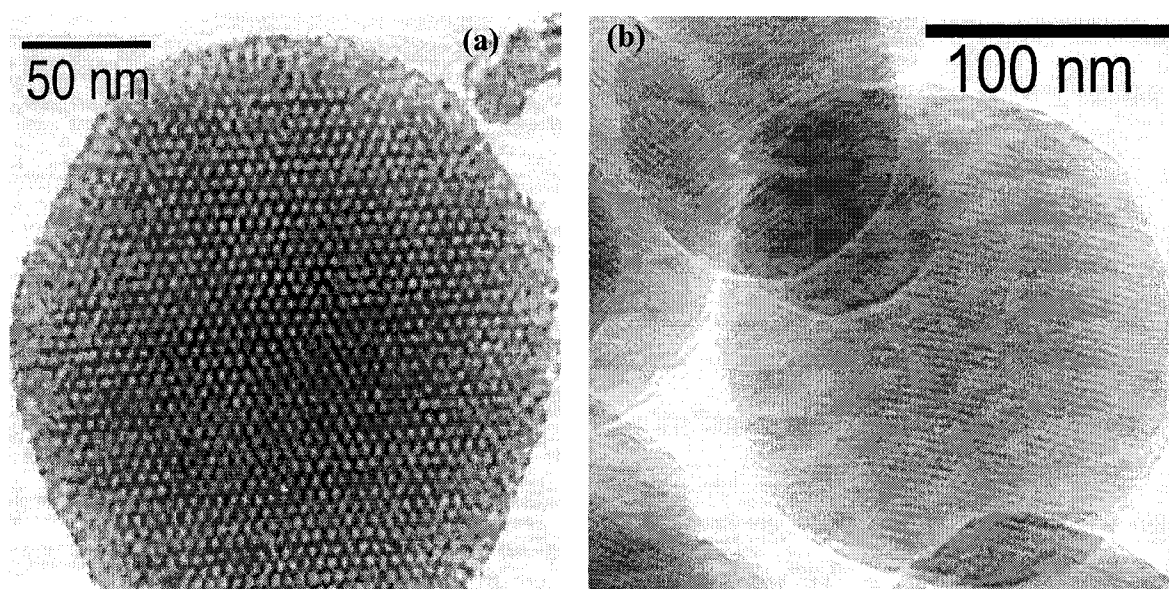


Figure 8-3. High-resolution transmission electron micrographs (TEM) of FTIC incorporated MCM-41 mesoporous silica nanospheres with amine functionality (F-MSN).

Furthermore, embedding a fluorescent dye within the matrix, although was designed for biocompatibility study, do not harm the mesostructure and consequently, the future applications for drug and gene can use this third dimension of the MSNs for tracking purposes.<sup>7</sup>

The biocompatibility study is including the observation of cellular fate as a function of time and amount of material that was applied. Eventually, these observations are essential to decide the type and extent of the applications. There are two hypotheses in MSNs application to the cell: an extracellular attachment on the cell membrane or an endocytic uptake. Whereas the first hypothesis would not be of real interest, the practical applicability of the second: MSN uptake inside the cells--whether is related to analytical determinations or delivery applications--would be always dependent of the amount of the material that is engulfed by a specific cell, as well as to the period of time that is necessary for the MSN to be internalized by the cell.

To investigate the aforementioned parameters, we performed a cellular uptake study of the material on HeLa and CHO cells. The dosage study experiments were designed to determine the maximum amount of material that can be incorporated by a cell. Fluorescein-doped, F-MSNs, were used for the study, enabling flow-cytometry assessment of the

fluorescence. The cells at visual confluency were treated with incremental amounts of material. Flow cytometry measurements were performed for a predetermined population of cells. Each set of cell cultures contained increasing amounts of material. To establish which of the aforementioned hypotheses is true, after measuring the fluorescence coming from samples, we added a fluorescence quencher, Trypan Blue, to each sample test tube. In this way, by measuring the fluorescence before and after quencher addition we can assess the location of the material in respect with the cell membrane. The first hypothesis, that the MSNs are located on the outer side of the membrane of the cells, was easily eliminated because the cells kept the same fluorescence level after Trypan Blue addition (Figure 8-4). This observation allows us to conclude that the material is completely engulfed by the cells.<sup>8</sup>

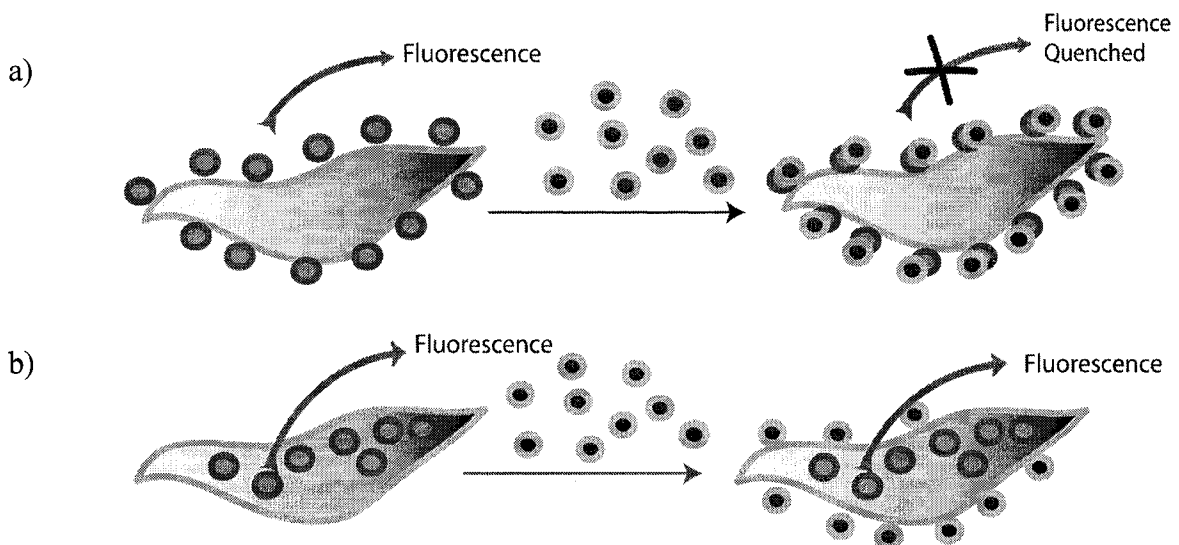


Figure. 8-4. Cartoon Schematic representation of possible interaction of MSNs with HeLa cells: Hypothesis 1: MSNs are located primarily outside of the cell and the addition of Trypan Blue causes the fluorescence quenching a); Hypothesis 2: MSNs are located primarily inside of the cells resulting; no quenching

The results, plotted in Figure 8-5, concluded that the maximum amount of MSNs engulfed by cells attained plateau at a dosage of 0.1 mg for  $10^5$  cells. As this uptake amount was observed after 12 hours of incubation, we further determined the minimum amount of time for incorporating the aforementioned dose (0.1 mg) for  $10^5$  cells. The kinetic study was performed for 12 hours and revealed that after the first 4 hours, the mean fluorescence became stationary. Together with the TEM micrographic evidence, this observations lead to

the final conclusion that the whole material was internalized in 4 hours, in the established conditions.

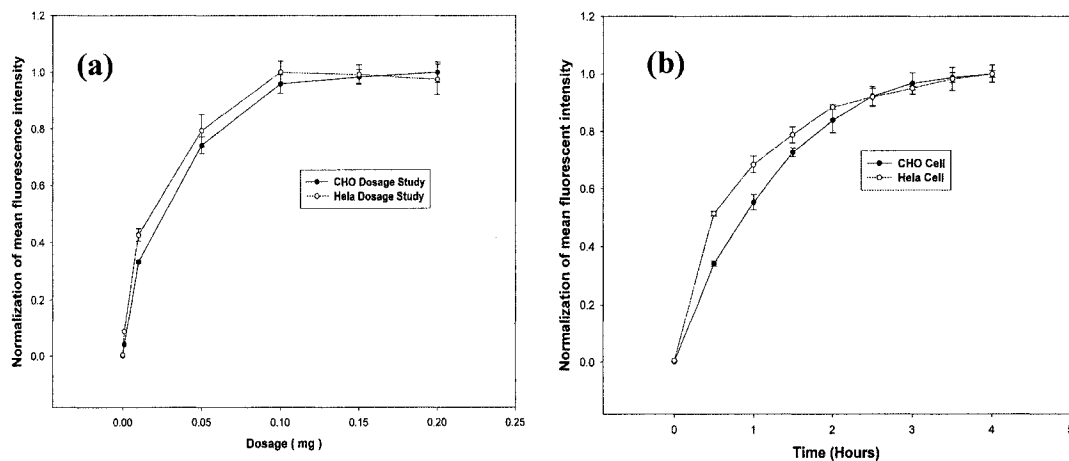


Figure 8-5. F-MSN internalization. Dosage study (a); Time dependence study (b)

In the case of cancer cells, whose cell cycle is very short, the carrier particles have to be shared during mitosis, to ensure a continuum in delivery. In order to study if the MSNs own these characteristic, we treated HeLa and CHO cells with Fluorescein doped MSNs and monitor their evolution by confocal microscopy. We observed that the cells are able to distribute the material evenly and share between daughter cells following mitosis.

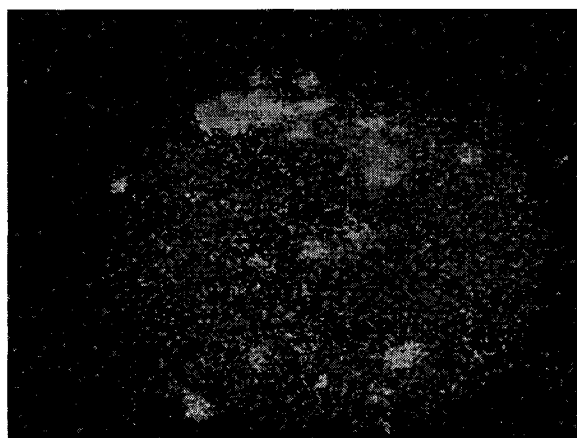


Figure 8-6. Fluorescent MSNs after endocytosis and cell mitosis – a dividing HeLa cell

Drug Delivery As the biocompatibility of the MSNs was demonstrated, we directed our attention to intracellular delivery applications. Intracellular delivery presents three major challenges: 1. *transmembrane trafficking*, involving the ability of MSN to penetrate the membrane while carrying a loading; 2. *release* of the “cargo” and 3. *drug action*, encompassing the amount and effectiveness of release inside the cell. The first intracellular delivery application that we are proposing here is related to cancer therapy and involves the delivery of an antineoplastic antibiotic, Doxorubicin, to HeLa cancer cells. In current cancer therapy, Doxorubicin (Adriamycin®) is normally administered intravenously with dramatic side effects in the body. When pure Doxorubicin is released in the cells, the drug is accumulating inside their nuclei, triggering an apoptotic death mechanism.

In our approach, Doxorubicin is encapsulated inside the mesopores of MSNs having the opening of the channels capped with bio-friendly PAMAM dendrimers of generation G4.5. The caps are covalently attached through a chemically cleavable disulfide linker. To demonstrate that this carrier has the ability to effectively deliver the drug to the cells we had to answer the three aforementioned challenges. The *transmembrane trafficking* of Doxorubicin loaded MSNs, Dox-MSNs, was monitored by TEM as showed in Figure 8-7.

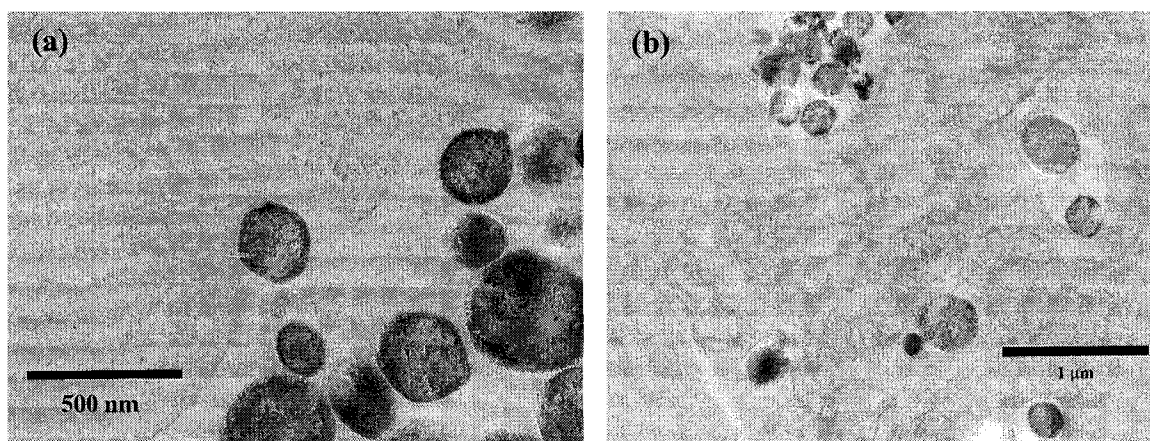


Figure 8-7. Cellular application of F-MSN (a) F-MSN engaged in endocytosis. (b) F-MSNs inside of a HeLa cell.

In this way, besides the proof brought by earlier presented flow cytometry investigations, we evidenced that the MSN are not only engulfed by the cells but also that they are not disturbing cellular homeostasis. The ability of MSN to penetrate the membrane while carrying a loading does not make them yet a drug delivery carrier. The second problem

to be addressed is the release of the drug inside the cytosol. To achieve this goal, the dendrimer caps used for drug encapsulation were attached through a disulfide bond that can be cleaved in the intensely reducing environment inside the cells. The confocal image in Figure. 8-8 illustrated the red fluorescent nuclei of HeLa cells that are demonstrating that the doxorubicin has been released from the MSNs mesopores after 12 hours of incubation of the Dox-MSNs with the cells. As a benchmark, we performed the same experiment with a water solution of Doxorubicin that was deposited on the cells. Doxorubicin mechanism of action consists of DNA intercalation with blocking of replication. For this reason, any cell that is undergoes Doxorubicin uptake will show red fluorescent nuclei. After fixation, the cells were counterstained with DAPI – a fluorescent dye that is also a DNA intercalator. As showed in the confocal image, no nuclei were available for DAPI staining, the Doxorubicin having occupied the chromosome. The localization of the drug in the nuclei in both cases proves that our release followed the same killing mechanism as the direct administration.

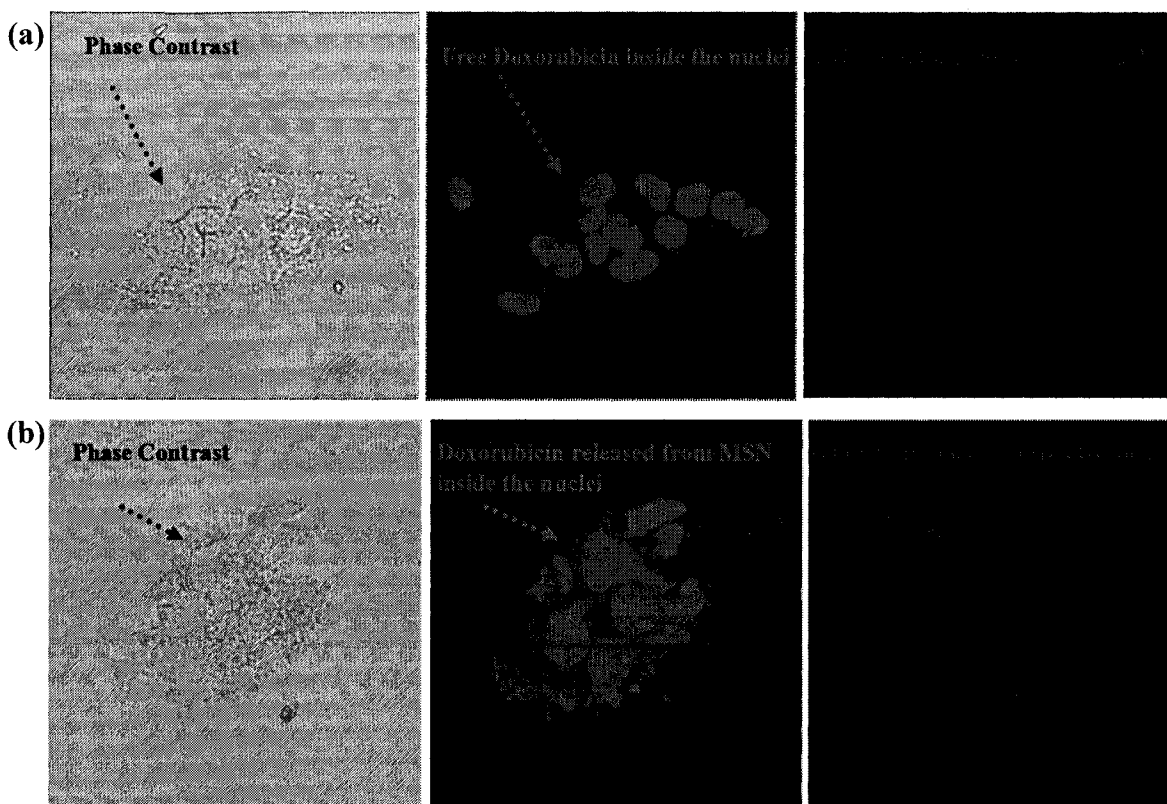


Figure 8-8. Doxorubicin delivery: Free doxorubicin delivered to HeLa Cells (a); MSN Encapsulated doxorubicin delivery in HeLa Cells (b)

The release mechanism is not clear, however, the reducing media of the cytosol might be responsible of disulfide bond cleavage. To attest that the Doxorubicin release is originated from uncapped mesopores and not from any physiabsorbed drug, we performed a control experiment where the disulfide linker in Dox-MSN was replaced by a non-cleavable urea bond to give Dox-ISP-MSN. The urea bond was generated by reacting the carboxyl termini of generation G4.5 PAMAM dendrimers with MSN-surface-bounded amine groups. The Doxorubicin entrapped in the mesopores could be visualized by examining the confocal images of the cells after treatment with Dox-ISP-MSN where the red spots can be easily observed. The striking evidence is brought by nuclei staining (Figure. 8-9).

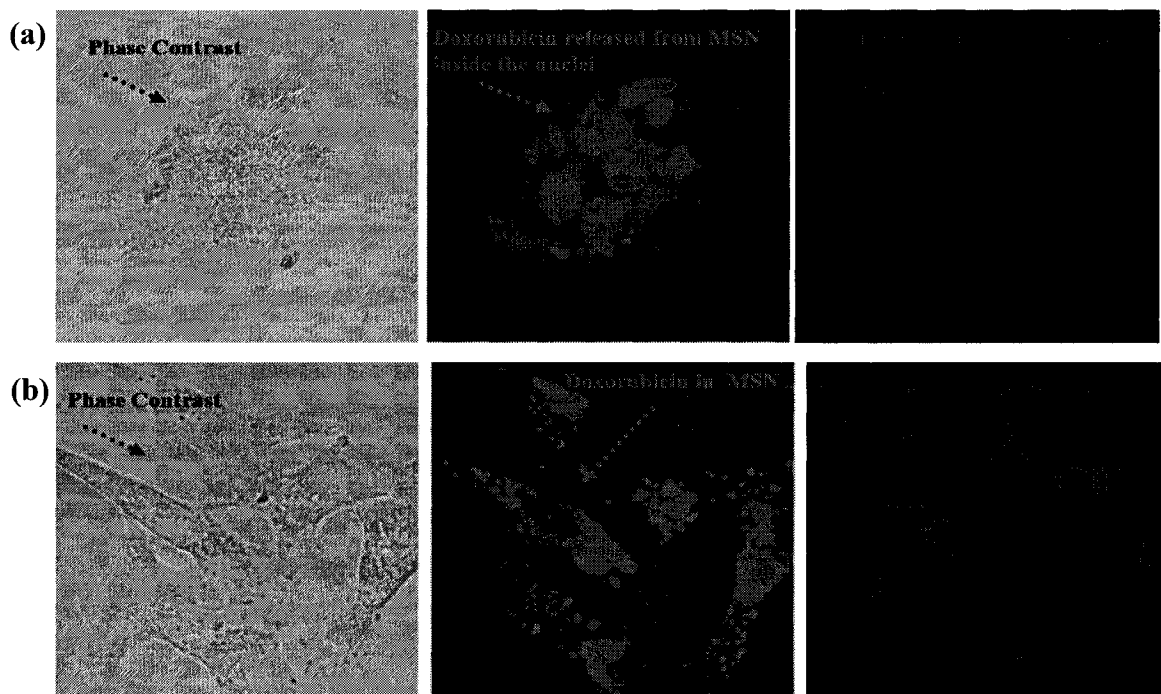


Figure. 8-9 Cleavable versus non-cleavable caps: Cells incubated with Dox-MSNs: release of Doxorubicin visualized by confocal microscopy (a); Cells incubated with Dox-Amine-MSNs: No release is observed, DAPI stain resides in the nuclei.

By contrast with the Dox-MSNs, the noncleavable caps do not allow Doxorubicin release and consequently, the cells are surviving for many days, as showed in the biocompatibility section. Furthermore, the nuclei are stained with DAPI that demonstrates that the nuclear DNA was not interfered by any Doxorubicin. Any possibility of Doxorubicin

physiabsorbtion was eliminated by extensive washes of the loaded MSNs followed by a filtration and fluorescent examination of the supernatant for any residual Doxorubicin in both Dox-MSN and Dox-ISP-MSN.

The third factor in evaluating a drug carrier is the *drug action* after release. This includes the amount and consequently the effectiveness of the release. To observe the fate of cells after dox-MSN application, a kinetic study was performed and confocal microscopy images were collected at intervals of four hours (Figure. 8-11). The cells started to change their shapes after 8 hours but at this stage only few of them had incorporated the Doxorubicin in the nuclei. After 12 hours, all cells had the drug in the nuclei. After another 12 hours, the culture was completely destroyed and only some debris could be observed on light microscope. Although we have a visual proof of effectiveness of the release, the quantitative data are important for trying to evaluate the mechnism. The amount of potential drug release of MSNs was evaluated by high performance liquid chromatography (HPLC).<sup>10,11</sup> The loaded Dox-MSNs, after extensive wash, were suspended in phosphate buffer at physiological pH (7.4) and the release was triggerd using dithiothreitol, a well known disulfide reducing reagent. The release profile is represented in Figure. 8-10. The amount of released drug is evaluated as 300 nmoles/mg MSNs.<sup>10,11</sup>

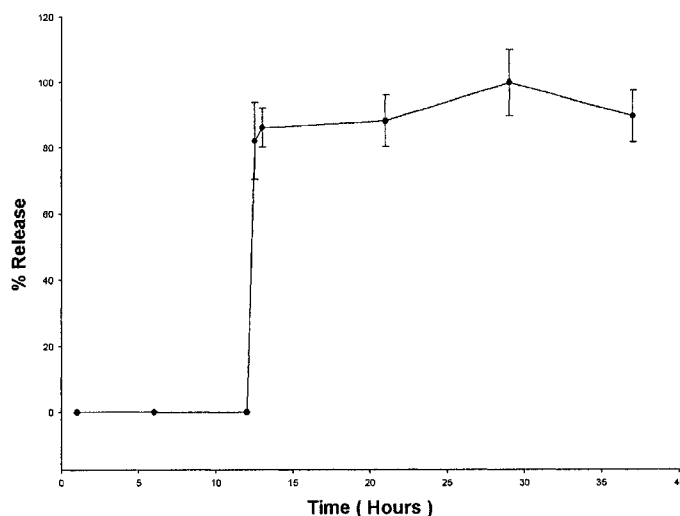


Figure 8-10. HPLC study of Doxorubicin releases from Dox-MSNs.



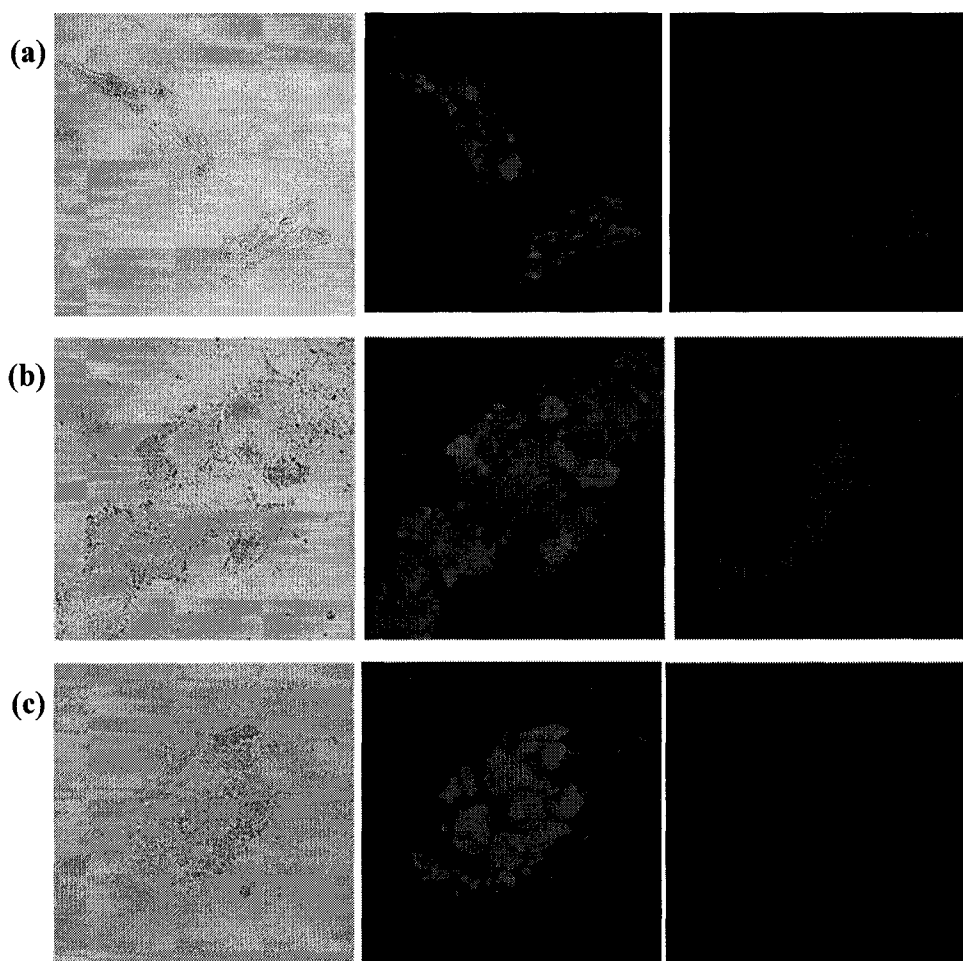


Figure 8-11. Kinetic study of Doxorubicin release: the Dox-MSNs were applied to cell cultures and monitored every four hours: after 4h (a); after 8h (b); after 12h (c)

### Transfection

As described in the introductory part, the material can prove universal carrier properties by transporting molecules not only inside the mesoporous channels but also, for large molecules, on the outer surface. It was demonstrated in our previously published work that MSNs, after derivatization with a cationically charged molecule on the external surface, can complex and delivery plasmid DNA to cancer cells such as HeLa and CHO at a superior efficiency than commercially available vectors. As the modularity of our system permits multiple functionalities, Texas Red doped MSNs were used for transfection of HeLa cells following the same derivatization/complexation/delivery pathway used in our previous work.

Confocal imaging was used for analyzing the cells after gene expression. The visual inspection of the sections, recorded at a thickness of 0.5  $\mu\text{m}$ , supplies a rapid method for investigating the internalization of the material.

The application of MSNs in cancer gene therapy is important but there are many other diseases that can take advantage of gene therapy utilizing this nanocomposite. In the present work, we disclose a breakthrough in gene delivery, as the system is able to transfect primary cells such as neural glia (astrocytes) at an unprecedented efficiency. Our MSN-based gene delivery nanodevice was applied to living cells in vitro. The nanocomposite comprises the core module--MSN, an exterior surface module for DNA complexation and an internal pore surface module as buffer capacity enhancer. In our approach, the external surface of MSN materials was modified with G2-PAMAM dendrimers, covalently attached through a surface anchored linker. The interior surface of the mesopores is functionalized with imidazole group. The positive surface has ability to complex plasmid DNA as it was demonstrated in our previously work.<sup>3</sup> As a proof of principle we condensed and transfected pEGFP-C1--plasmid that is encoding for green fluorescent protein--to different types of cell lines as well as primary cells. The transfection of HeLa and CHO cells with pEGFP using MSNs was published elsewhere. However, the efficiency of the method was not satisfactory when applied to astrocytes and therefore required further optimization. One of the impediments in cells transfection is represented by endosomal escape of the DNA. The pH inside the endosome reaches values around 5, suggesting that by fine-tuning the pH one can manipulate the carrier fate. The concept of "proton sponge" was introduced by<sup>9</sup> and is related to the buffer capacity of the carrier. This feature is enhancing the efficiency of gene transfection by causing endosomal burst and consequent escape of DNA. Because of the large surface area of the MSNs, they can be modified with functional groups to provide a strong buffer capacity to these gene carriers and thus enhancing endosomal escape thus increasing the efficacy of transfection. Anchoring dihydroimidazole functionality in the mesopores--via our previously published co-condensation reaction--proved to be the key of this optimization process. The transfection efficiency for astrocytes was considerably increased in this way from 1-2% to 12.4% which is unprecedented for primary cells when using other non-viral vectors.

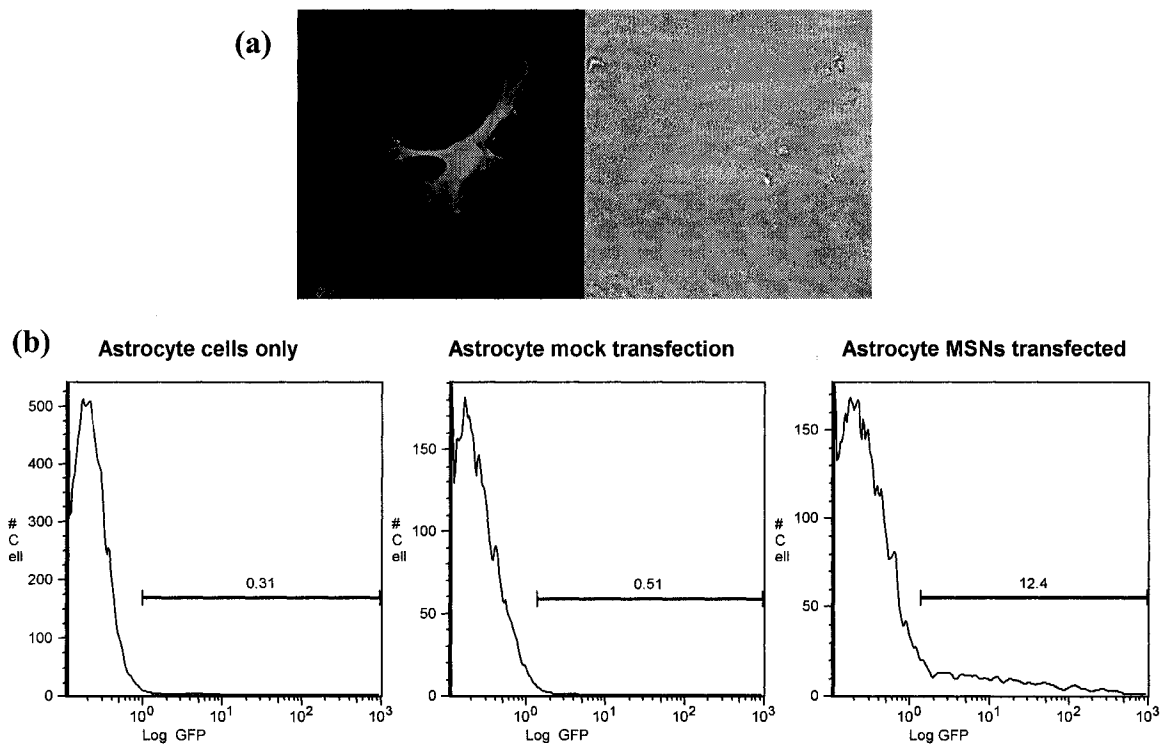


Figure 8-12. Transfection of neural glia (astrocytes) with pEGFP utilizing G2-MSN as a transfection vector

### Co-transfection of two different types of plasmids

The transfection of different types of cells with plasmid pEGFP offers a proof of principle for applicability in MSN-based transfection for one particular gene. However, one of the major challenges for therapeutic gene transfection is to develop a method for fast response detection of the encoded protein expression. This is possible for a gene encoding a signal such as fluorescence (pEGFP) but most of therapeutic genes have as a single result, the protein that is expressed. One of the solutions of the problem is the engineering of a marker gene--such as the one encoding for GFP--inside the plasmid of choice. The expression of the marker is representing a benchmark for the expression of the desired gene. However, the genetic engineering is tedious; besides, as the size of the plasmid increases, eventually the whole transfection process can be compromised. The alternative is represented by

cotransfection of two plasmids: one encoding for the therapeutic gene and one encoding for the marker gene. For the later choice, the ideal gene carrier would be able to deliver both plasmids, in a known ratio, so that the expression of the marker can be correlated with the extent of the therapeutic gene expression. In order to test if our system can achieve the aforementioned task, we used two plasmids that encode for different gene fluorescent proteins: pEGFP-C1 and DsRed-N1. The ratio between the two plasmids in the transfection experiments was 1:1 for all experiments. Since we have chosen plasmids that encode for fluorescent proteins, the level of expression could be monitored by flow cytometry. The most interesting finding was that within a cell culture there is no mixed population of transfected cells, i.e. there were no cells transfected only with one type of the two plasmids. The same observation is illustrated by the confocal images in Figure 8-14. The efficiency of cotransfection is similar with the transfection efficiencies that we reported for transfection of pEGFP in HeLa and CHO cells in Figure 8-15. The TEM micrographs bring further evidence of particle internalization shown in Figure 8-13.

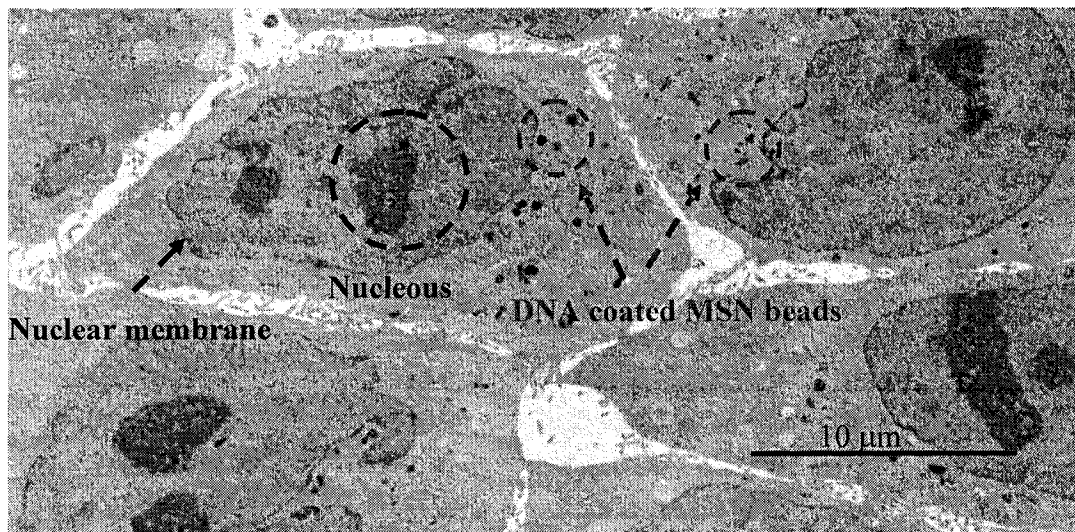
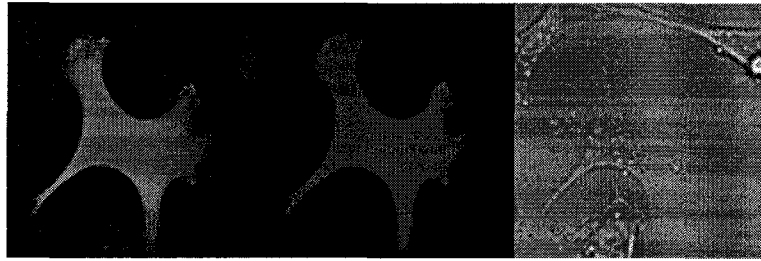


Figure 8-13 TEM micrograph of cotransfected HeLa cells

(a) HeLa Cells



(b) CHO Cells



Figure. 8-14. Confocal fluorescence images and phase contrast images of HeLa cells (a) and CHO cells (b).

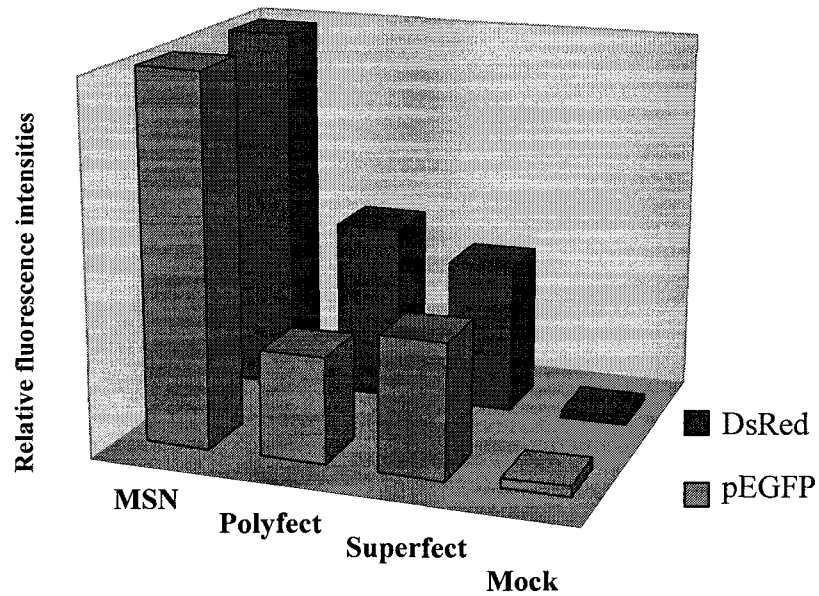


Figure. 8-15. Relative transfection efficiencies between several transfection reagents: G2-MSN, Polyfect and Superfect. Mock transfection (beads without plasmids) was also performed to demonstrate that there is no fluorescent signal detected in the absence of DNA complexed MSNs.

### Conclusions

The potential of MSN in drug and gene delivery was demonstrated. Possible combinations of the two approaches can be easily envisioned. In future applications the MSNs can serve as gene carriers using the outer surface while carrying gene up- or down-regulator molecules inside the mesopores. On the other hand, one of the methods proposed in the biocompatibility study was utilizing fluorescent doped MSNs in flow cytometry, demonstrating a possible utility in flow cytometry measurements. We can envision that by further outer surface derivatization of fluorescence MSN particles with cell targeting moieties, one can perform cellular sorting, the damaged cells being labeled and selected. In an extreme approach, all three elements of MSN: silica matrix, the nanochannels and the outer surface could be exploited at the same time, the device being endowed with both carrier and tracking abilities.

### Acknowledgements

Lai, Cheng-Yu thanks Dr. Paul Kapke, Dr. Janice Buss, Dr. Luisa Tobatabai, Dr. Marit Nilsen-Hamilton and the cell and hybridoma facilities of ISU for their assistance. I would highly express my sincere appreciation to Dr. Jeftinija, S. for the gift of Astrocyte cells.

### References

1. (a) Uhrich, K. E.; Cannizzaro, S. M.; Langer, R. S.; Shakesheff, K. M. *Chem. Rev.* **1999**, *99*, 3181. (b) Langer, R. *Acc. Chem. Res.* **1993**, *26*, 537 and references therein.
2. (a) Luo, D.; Saltzman, W. M. *Nat. Biotechnol.* **2000**, *18*, 893. (b) Kneuer, C.; Sameti, M.; Bakowsky, U.; Schiestel, T.; Schirra, H.; Schmidt, H.; Lehr, C.-M. *Bioconjugate Chem.* **2000**, *11*, 926. (c) He, X.-X.; Wang, K.; Tan, W.; Liu, B.; Lin, X.; He, C.; Li, D.; Huang, S.; Li, J. *J. Am. Chem. Soc.* **2003**, *125*, 7168. (d) Luo, D.; Han, E.; Belcheva, N.; Saltzman, W. M. *J. Controlled Release* **2004**, *95*, 333. (e) Vallet-Regi, M.; Ramila, A.; del Real, R. P.; Perez-Pariente, J. *Chem. Mater.* **2001**, *13*, 308. (f) Munoz, B.; Ramila, A.; Perez-Pariente, J.; Diaz, I.; Vallet-Regi, M. *Chem. Mater.* **2003**, *15*, 500. (g) Ramila, A.; Munoz, B.; Perez-Pariente, J.; Vallet-Regi, M. *J. Sol.-Gel Sci. Technol.* **2003**, *26*, 1199.

3. (a) Lin, V. S. Y.; Lai, C.-Y.; Huang, J.; Song, S.-A.; Xu, S. *J. Am. Chem. Soc.* **2001**, *123*, 11510. (b) Radu, D. R.; Lai, C.-Y.; Wiench, J. W.; Pruski, M.; Lin, V. S. Y. *J. Am. Chem. Soc.* **2004**, *126*, 1640. (c) Radu, D. R.; Lai, C.-Y.; Jeftinija, K.; Rowe, E. W.; Jeftinija, S.; Lin, V. S.-Y. *J. Am. Chem. Soc.* **2004**; *126*, 13216.
4. Lai, C.-Y.; Trewyn, B. G.; Jeftinija, D. M.; Jeftinija, K.; Xu, S.; Jeftinija, S.; Lin, V. S.-Y. *J. Am. Chem. Soc.* **2003**, *125*, 4451.
5. (a) Radu, D. R.; Lai, C.-Y.; Jeftinija, K.; Rowe, E. W.; Jeftinija, S.; Lin, V. S.-Y. *J. Am. Chem. Soc.* **2004**; *126*, 13216. (b) See chapter 7 for details and references therein.
6. Marjan, B; Olavi, S; Egon, M. *Journal of Colloid and Interface Science*, **2002**, *254*, 274 and references therein.
7. (a) Yao, Y; Zhang, M; Shi, J; Gong, M; Zhang, H; Yang, Y. *Materials Letters*, **2001**, *48*, 44. (b) Onida, B.; Bonelli, B.; Borello, L.; Fiorilli, S.; Bodoardo, S.; Penazzi, N.; Areat, C. Otero; Palomino, G. Turnes; Garrone, E. *Studies in Surface Science and Catalysis* **2003**, *146*, 379.
8. (a) Rohloff L., Andreas Wiesner and Peter Götz, *Journal of Insect Physiology*, **1994**, *40*, 1045. (b) Chok P. Wan, Choon S. Park and Benjamin H. S. Lau, *Journal of Immunological Methods*, **1993**, *162*, 1.
9. (a) Plank, C., Zatloukal, K., Cotton, M., Mechtler, K., Wagner, E. *Bioconjugate Chem.* **1992**, *3*, 533. (b) Plank, C., Oberhauser, B., Mechtler, K., Koch, C., & Wagner, E. *J. Biol. Chem.* **1994**, *269*, 12918. (c) Wagner, E., Plank, C., Zatloukal, K., Cotton, M., & Birnstiel, M. L. *Proc. Natl. Acad. Sci.* **1992**, *89*, 7934. (d) Behr, J.-P. *Chimica*, **1997**, *51*, 34. (e) Boussif, O., Lezoualc'h, F., Zanta, M. A., Mergny, M. D., Scherman, D., Demeneix, B., & Behr, J.-P. *Proc. Natl. Acad. Sci.* **1995**, *92*, 7297. (f) Pack, D., Putnam, D., & Langer, R. *Biotechnol. Bioeng*, **2000**, *67*, 217. (g) Midoux, P. & Monsigny, M. *Bioconjugate Chem.* **1999**, *10*, 406.
10. (a) Zhao, P.; Dash, A.K. *Journal of Pharmaceutical and Biomedical Analysis*, **1999**, *20*, 543. (b) E. Configliacchi, G. Razzano, V. Rizzo, A. Vigevani, *Journal of Pharmaceutical and Biomedical Analysis*, **1996**, 123.
11. G4.5-capped MSN nanoparticles with Doxorubicin (10.00 mg) material were dispersed in 1.50 mL of PBS buffer (pH 7.4), followed by repeating

wash/sonication/centrifugation cycles for five times to remove physisorbed, uncapped Doxorubicin molecules on the exterior surface of the material. The purified MSN/drug composite was redispersed in 3.50 mL of PBS buffer (pH 7.4). Aliquots were taken every 4 h over a time period of 12 h from the MSN/PBS buffer suspension and injected to an analytical HPLC system (Hitachi LC/3DQMS with a reverse phase C18 column (Vydac), 0.4 cm × 25 cm) to monitor the leaching of the mesoporous channel encapsulated Doxorubicin molecules.<sup>10</sup> After 12 h, dithiothreitol (DTT, 18.50 mM) was added to the suspension to cleave the disulfide linkage between the G4.5 dendrimers and the MSN. The kinetic profiles of the DTT-induced release of Doxorubicin were monitored by following two literature-reported HPLC separation conditions.<sup>10</sup> The peaks/areas at 254 nm were monitored/integrated for the quantitative analysis of amounts of released Doxorubicin. In of mixing, the suspension was centrifuged and the individual concentrations of dopamine and glutamic acid in the supernatant were analyzed by HPLC. Flow rate of mobile phase was 1 mL/min. separation was obtained with the following linear gradient of water (A)-acetonitrile (B), both containing 0.1% (v/v) CF<sub>3</sub>COOH: from 25% B to 30% B in 10 min, and then up to 80% B in 5 min, finally elution was maintained isocratic for the next 15 min to return to the initial condition and re-equilibrate. The column temperature was set at room temperature and the injection volume of samples was 25 μL for all analyses.



## Chapter 9. General Conclusions

In this dissertation, I presented my research accomplished in the past 5 years in chronological order. Each chapter discussed and demonstrated an application of pluripotent mesoporous silica nanospheres in three major areas. Throughout this dissertation they are presented as noninvasive, high sensitive, fast response and high resolution biosensors, as high selective and well-controlled drug delivery nano-devices and as *de novo* designed non-viral transfection reagents -“The Trojan Horse reloaded “.

Chapter 1 presented a general introduction of the dissertation, bringing a brief insight over each chapter.

Chapter 2 have introduced a novel co-condensation method that can fine tune the amount of chemically accessible organic functional groups on the pores surface of MCM-41 type mesoporous silica nanosphere (MSN) materials by matching the electrostatic interactions between surfactant head group and the organoalkoxysilane precursors at the micelle-water interface.

Chapter 3 presented the design and synthesis of a well-defined, monodispersed mesoporous silica nanosphere (MSN) as a fluorescence sensory system which could serve as synthetic scaffold for selective molecular recognition of multifunctional molecules with similar sizes and functionalities. The sensing event can be achieved not by shape recognition but by creating a multifunctionalized mesopore as the "active site" with combinations of covalent (isoindole formation) and noncovalent interactions (hydrophobic and  $\pi - \pi$  interactions).

Chapter 4 demonstrated the modification of a MSN coated with a poly(lactic acid) layer as a gatekeeper to regulate the penetration of molecules in and out of the nanoscale pores of PLA-MSN material. We successfully selected the molecular recognition events between several structurally simple neurotransmitters, i.e., dopamine, tyrosine, and glutamic acid and a pore surface-anchored *o*-phthalic hemithioacetal (OPTA) group.

Chapter 5 presented the synthesis and characterization a of MCM-41 type mesoporous silica nanosphere-based (MSN) controlled-release delivery system using surface-derivatized cadmium sulfide (CdS) nanocrystals as chemically removable caps to

encapsulate several molecules inside the organically functionalized MSN mesoporous framework. The release profiles of several drugs as well as the delivery efficiencies for neuroglia cells demonstrated that the organically functionalized mesoporous silica nanosphere material can be used as a novel stimuli responsive controlled-release delivery carrier.

In chapter 6, we applied a luciferase-catalyzed chemiluminescence technique to study the ATP release from mesoporous silica nanospheres end-capped either with CdS nanocrystals or with PAMAM dendrimers. By changing the capping molecules as well as the uncapping triggers, we concluded that the release profile of a drug of interest can be fine-tuned depending on whether a high concentration, one-time drug release or a lower level, continuous drug release treatment is desired.

Chapter 7 introduced a de novo designed gene shuttle. The nanocomposite consists of a polyamidoamine dendrimer-capped mesoporous silica nanosphere and a model gene-pEGFP that is encoding for green fluorescent protein. The novel device is providing high transfection efficiencies in several types of cells. The cellular uptake behavior of capped MSNs envisioned the possibility of creating a universal transmembrane carrier for gene therapy, drug delivery and imaging applications.

Chapter 8 presented the possible combination of intracellular applications of capped-MSN, either drug delivery or multiple gene transfection, by proper engineering the inner surface or external surface. Fluorescent doped MSNs were used in flow cytometry, demonstrating a possible utility in flow cytometry measurements. In the future, we can apply this novel carrier on living cells in gene therapy and employ the channels to encapsulate up-regulation or down-regulation molecules.

Chapter 9 is concluding the dissertation with a final review of the entire work.